2011

Studies of inhomogeneous superconducting states in novel materials

Robert Pearson Beaird
Louisiana State University and Agricultural and Mechanical College, rbeair1@tigers.lsu.edu

STUDIES OF INHOMOGENEOUS SUPERCONDUCTING STATES IN NOVEL MATERIALS.

A Dissertation

Submitted to the Graduate Faculty of the
Louisiana State University and
Agricultural and Mechanical College
in partial fulfillment of the
requirements for the degree of
Doctor of Philosophy

in

The Department of Physics and Astronomy

by
Robert Beaird
B.S., Centenary College of Louisiana, 2003
M.S., Louisiana State University, 2008
May, 2011

Dedication

For George and Lynne, my parents, and Billy, my brother,
all of whom have put up with me for longer than I can remember...

Acknowledgments

I want to thank Matthew Patterson, Sai Vinjanampathy, and Sulakshana Thanvanthri, the three people two whom I am closest outside of my family. It is to them that I am most grateful since, without them, I would not have made it through the past several years of graduate study. I want to thank Josh Thibodaux, with whom I share my academic advisor, for being there for me, especially when our work took us far from home. I also want to thank my colleagues Wesley Even, Charles Bradley, Andrew Collazzi, Frank Womack, and Rob Collyer for their friendship and support throughout my graduate school tenure. My family has offered unequivocal encouragement and support for my entire graduate education, and I especially thank my parents for their financial support over my last year of graduate study.

I would like to thank my adviser Ilya Vekhter for his support, guidance, and semi-infinite patience throughout this research and my time at LSU. I would also like to thank Dana Browne for his willingness to answer my questions and offer insights that helped to see the physics in the computation. In the same vein, I would like to thank Dan Sheehy, John DiTusa, and Phil Adams, all of whom tolerantly entertained my questions from time to time. I would like to thank Anton Vorontsov, my collaborator whose help was invaluable in completing the first half of my project work, and Jian-Xin Zhu, my host at Los Alamos National Labs (LANL) who provided me with the numerical techniques required for much of the second half of my thesis research. Finally, I thank my committee members John DiTusa, Phil Adams, and Ravi Rau for being so helpful as I completed my dissertation.

This work has been supported, in part, by grants DE-FG02-08ER46492 (LSU) and DE-AC52-06NA25396 (LANL) from the U.S. Department of Energy. This research also has been made possible by support from the Louisiana Board of Regents (LSU), the Charles E. Coates Memorial Fund (LSU), and the U.S. DOE Office of Science (LANL).

Table of Contents

Abstract

I provide detailed studies of two types of novel superconducting systems. In the first, I examine the effect of thermal (Gaussian) magnetic fluctuations on the superconducting transition of paramagnetically-limited superconductors under a Zeeman magnetic field. I consider transitions into both the uniform and the modulated (Fulde-Ferrell-Larkin-Ovchinnikov) superconducting states. I derive the Landau free energy expansion in powers of the superconducting order parameter, allowing for competition between the magnetic fluctuations and the superconducting order. I determine the order of the transition at the upper critical field and find that the fluctuations drive the transition, usually second-order, to first order at intermediate temperatures for both the uniform and modulated states. I also compute the thermodynamic signatures of the transition along the upper critical field. I use these results to help explain experiments on the heavy-fermion superconductor $CeCoIn_5$, for which the superconducting transition is first-order at low temperatures and large magnetic fields. In the second study, I use a T-matrix approach to examine the resonant state generated by a single, non-magnetic impurity in multi-band superconducting systems. I consider extended s-wave symmetry of the superconducting gap and allow for anisotropy of the gap along the Fermi surface. I derive analytic expressions for the Green's functions in the continuum and identify the criteria for the formation of the impurity states, emphasizing the role the band structure plays for existence of the resonant state. I then use these results to guide and explain the results of numerical studies of the impurity states on a lattice. For my numerical approach, I use dispersion relations appropriate for the description of the ferropnictides, a recently-discovered family of iron-based superconductors. I map the impurity state in real-space and emphasize how the features of these states can help identify the nodal structure of the gap on each of the Fermi surface sheets.

1. Introduction

Condensed matter physics concerns itself with explaining the physics of collective phenomena in dense phases of matter. Of special interest are the ordered states that form when some symmetry of the system is broken by the quantum-mechanical or electromagnetic interactions between the material's constituent parts. Superconductivity, one such state, arises when the condensation of paired electrons breaks the U(1) gauge symmetry of the system. The superconducting state is characterized both by infinite electrical conductance and the screening of the bulk of the superconductor from applied magnetic fields. It has been the subject of intense study over the past century, and is the state upon which my work for this dissertation is based.

1.1 Conventional Superconductivity

1.1.1 Discovery and Description of Superconductivity

Discovered experimentally in 1911 by Heike Kamerlingh Onnes[1], superconductivity is a low-temperature phase wherein the electrical resistance of a metal abruptly disappears below a characteristic, or critical, temperature T_c. It was not until 1950 that Ginzburg and Landau[2] provided a phenomenological theory to describe the properties of type II superconductors in the vicinity of T_c. They did this by providing a small-parameter expansion of the superconductor's free energy in terms of a complex-valued order parameter ψ and its gradients. Seven years later, Bardeen, Cooper, and Schrieffer (BCS) provided the first microscopic description of superconductivity via a variational wave function that accounted for the condensation of the electron pairs. Finally, in 1959, Gor'kov connected the BCS and Ginzburg-Landau theories by showing that, near T_c, the Ginzburg-Landau order parameter ψ is directly proportional to Δ, the amplitude of the BCS pair wave function [3].

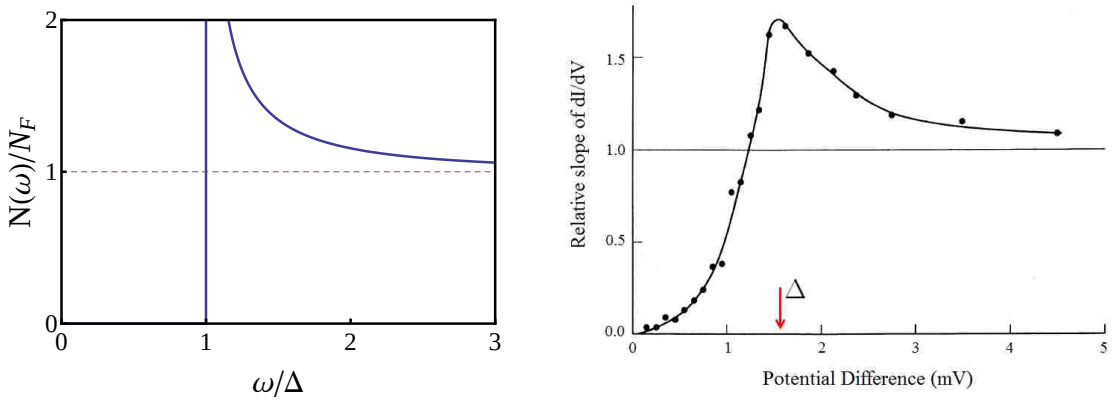

Figure 1.1: Density of states in conventional s-wave superconductor from both theory and experiment. The figure on the left is the theoretical density of states $N(\omega)/N_F = \omega/\sqrt{\omega^2 - \Delta^2}$ as predicted by Bardeen, Cooper, and Schrieffer[5]. The figure on the right is the density of states for lead at T=1.6K as measured in an electron tunneling experiment by Giaever in 1960[4]. In each case, the horizonal line represents the density of states in the normal phase. The softened gap feature in the experimental data is due to the convolution of the density of states with the energy derivative of the Fermi distribution function.

The conventional BCS theory shows how superconductivity arises when electrons of the same energy, near the Fermi surface, form pairs of opposite momentum and spin, pairs which then condense into a single quantum mechanical state. This condensate of "Cooper pairs" is phase-coherent throughout the superconductor. The formation of the condensate lowers the energy of the system by the energy $U_{cond} = N_F\Delta^2/2$, where N_F is the Fermi-level density of states in the normal-phase. The size of a Cooper pair is $\xi_0 = \hbar v_F/k_B T_c$, where $\hbar$ is the reduced Planck constant, v_F is the Fermi velocity, and k_B is the Boltzmann constant. Experimentally, the superconducting state is characterized by the existence a energy gap, of width 2Δ, from which all of the single-electron states have been removed. The states from within the gap are moved to higher energies when the superconductivity sets in and coherence peaks form in the density of states at the energies $\omega = \pm\Delta$. In Fig. 1.1, I show the density of states both as predicted by BCS theory and as first measured for lead in 1960[4].

All that BCS theory requires for pairing to take place is an attractive interaction between the electrons near the Fermi surface. Any attractive interaction, no matter how weak, leads

to pairing and, in the usual case, is due to the electron-phonon interaction. The situation can be more interesting when the pairing arises from another source, and, in particular, non-trivial shapes of the superconducting gap can result when pairs are formed by a repulsive interaction. This falls beyond the scope of the original BCS theory, and I explain this situation in more detail in Section 1.2.

1.1.2 Two Types of Superconductivity and Response to a Magnetic Field

In the superconducting state the Cooper-pair's center-of-mass momentum couples to the vector potential of an applied magnetic field. In 1933 Meissner and Ochsenfeld discovered the perfect, macroscopic diamagnetic response of superconductors to a weak magnetic field [6]. This perfect diamagnetism results when supercurrents flowing along the surface screen the applied field from penetrating the superconductor beyond the penetration depth λ. This expulsion of the magnetic field occurs regardless of whether the field is applied before or after cooling below T_c. This highlights the exotic nature of the superconducting state since a simple zero-resistance metallic state would *trap* any field applied above its zero-resistance transition. The diamagnetic response can drive the superconductor back into its normal phase when the kinetic energy of the surface currents is greater than the condensation energy, and the field at which this occurs is the thermodynamic critical field $H_{c,therm}(T)$.

There are two types of superconductor that behave very differently when the magnetic field increases. Type I superconductors expel the field from the material until the energy gap closes discontinuously in a first-order transition. In contrast, type II superconductors allow the field to penetrate through supercurrent vortices, in the so-called mixed state that forms above H_{c1}, before the order parameter vanishes in a second-order transition at the upper critical field H_{c2}. The superconducting transitions in both types of superconductor can be described using Ginzburg-Landay (GL) theory. The GL theory allows for the superconducting order parameter to change over the temperature dependent length $\xi_L(T)$, and $\xi_L = \xi_0$ at

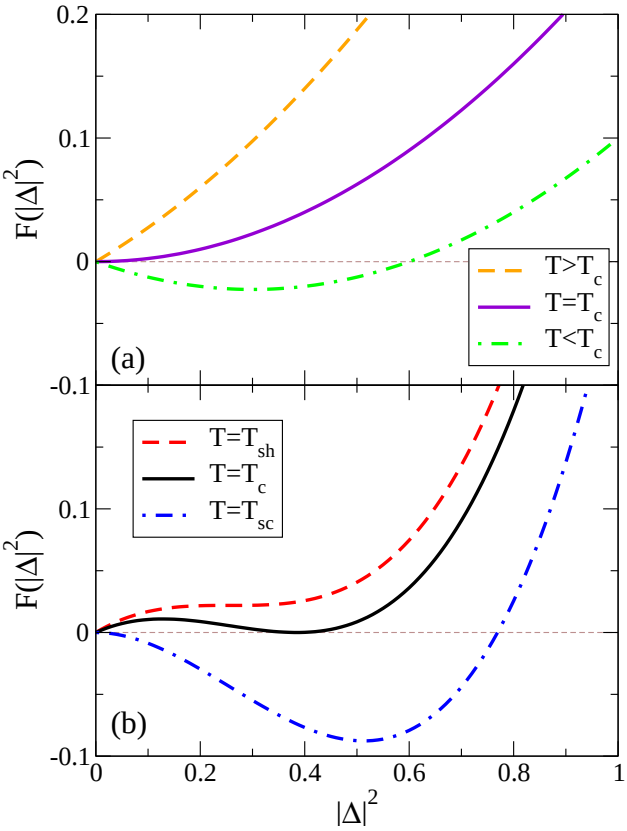

Figure 1.2: Landau free energy $F(|\Delta|^2)$ near (a) a second and (b) a first order transition at T_c. Coexistence of both states is possible near the first order transition, and the supercooling (T_{sc}) and superheating (T_{sc}) temperatures mark the limits of this coexistence.

$T = 0$. In 1957, Abrikosov used the Ginzburg-Landau theory to predict the vortex state in type II superconductors with $\lambda < \sqrt{2}\xi_L(T)$ [7]. In this case, the superconducting state is destroyed at the orbital-limited upper critical field which is $H_{c2,orb} = \Phi_0/2\pi\xi_0^2$ at $T = 0$. Here $\Phi_0 = hc/2e$ is the flux quantum.

The spins of the Cooper pairs also couple to the magnetic field through the Zeeman effect. The effect of the Zeeman field is to spin-polarize the electrons that make up the Cooper pair, a process called paramagnetic limiting. For most materials the paramagnetic effect is much less significant that the orbital effects, hence systems in the paramagnetic limit are novel and of interest. In Chapter 3, I describe the theory of superconductivity in the paramagnetic limit and the spatially inhomogeneous superconducting states that it can bring about.

Before moving on, I remind what is meant by first-order and second-order transitions, both of which can be described by the GL theory. Recall that Ginzburg-Landau theory describes the free energy of the superconducting state as an expansion in the order parameter ψ, or equivalently, in the amplitude of the gap Δ. As shown in Fig. 1.2(a), a second-order transition occurs when the minimum of the energy occurs for $\Delta = 0$ at the transition temperature T_c. This means that the gap is zero at the transition and opens smoothly upon cooling below T_c. For a first-order transition, which I shown in Fig. 1.2(b), the gap is finite at the normal-to-superconducting transition. Notice that the energy of the normal ($\Delta = 0$) and the superconducting state are equal at the first-order transition, hence coexistence of the two states can be expected near T_c. Near a first order transition, there are two free energy minima in a temperature range about T_c, one each for the normal and superconducting states, and this allows for hysteresis when cooling or heating the material through T_c. Specifically, the normal state can exist down to the supercooling temperature T_{sc}, and the superconducting state can exist at temperatures up to the superheating temperature T_{sh}. For a field-induced superconducting transition, the supercooling field and the superheating field are analogous to T_{sc} and T_{sh}, respectively.

1.2 Unconventional Superconductivity

The gap in an unconventional superconductor transforms according to a non-trivial representation of the underlying lattice symmetry of the material. This can happen when spin fluctuations provide the pairing mechanism in systems near incipient antiferromagnetic (AFM) order, and the strong on-site Coulomb energy reduces the amplitude of on-site pairing and enhances the pairing on nearest-neighbor sites. This results in an anisotropic gap function in momentum space and can lead to a sign change in the gap on different parts of the Fermi surface (FS) or between different FS sheets [8].

The work for this dissertation is based upon two families of layered materials where the electronic structure is nearly two-dimensional (2D). The first is the isostructural cerium-based compounds, called the 115's, of which I focus on $CeCoIn_5$[9] and its d-wave pairing state. The other is the family of multi-band iron-based compounds that were discovered relatively recently[10], for which the gap structure remains a topic of debate. Below I give a brief overview of the unconventional superconducting state in these two materials, and I present a more detailed description of each in Chapters 2 and 6, respectively.

1.2.1 Heavy-Fermion Superconductivity

Superconductivity in heavy-fermion materials arises out of a metallic state with strong electronic correlations that are due to the presence of a lattice of magnetic moments. As conduction electrons propagate through the system, they can scatter off of the local moment. In the single-ion Kondo effect, the electron forms a bound state with the local moment at $T = 0$, and the precursor to this bound state is evident in the enhanced scattering of electrons at low-T. When there is a lattice of magnetic ions, the conduction electrons collectively experience resonant scattering at low temperatures so that the quasiparticle effective mass dramatically exceeds the band mass. This reduces the Fermi velocity of the electrons and increases the orbital-limiting field $H_{c2,orb} \propto v_F^{-2}$. The result is that the orbital effect decreases in importance when compared to the paramagnetic effect.

Superconductivity in $CeCoIn_5$ forms from heavy electrons that reside on a corrugated Fermi surface that is open along the crystalline c-axis [11]. Since the system is close to AFM order[12, 13, 14, 15], the pairing of the heavy electrons is likely mediated by AFM spin fluctuations. This results in the so called d-wave order parameter that changes sign across the four gap nodes on the Fermi surface.

1.2.2 Multi-Band Superconductivity

The pnictides are layered materials with Fermi surfaces comprised of several quasi-2D

sheets. In the pnictides, the pairing occurs between states that reside on different Fermi surface sheets that are well-separated in momentum space. In addition, the strong on-site Coulomb repulsion induces anisotropy of the superconducting gap on some of the sheets. This gap anisotropy can lead to "accidental" nodes, *i.e.*, nodes that are not enforced by symmetry, or may simply result in a deep minimum in the gap on the FS sheet. The details of the gap shape have been under intense investigation in the three years since high-temperature superconductivity was first reported in these compounds [16]. It is this open question of the detailed shape of the gap that motivates my study of superconductivity in these systems.

2. The Heavy-Fermion Superconductor $CeCoIn_5$

As I described Section 1.2.1, superconductivity in heavy-fermion materials arises out of a metallic state with strong electronic correlations that are due to the lattice of magnetic ions. For $CeCoIn_5$, whose crystal structure I show in Fig. 2.1, the magnetic ion is cerium which has a valence shell comprised of a single f electron that provides a magnetic moment of $2.6\mu_B$. Measurements on $CeCoIn_5$ indicate that the conduction electrons responsible for superconductivity are quite heavy and reside primarily on the quasi-2D FS sheets [11].

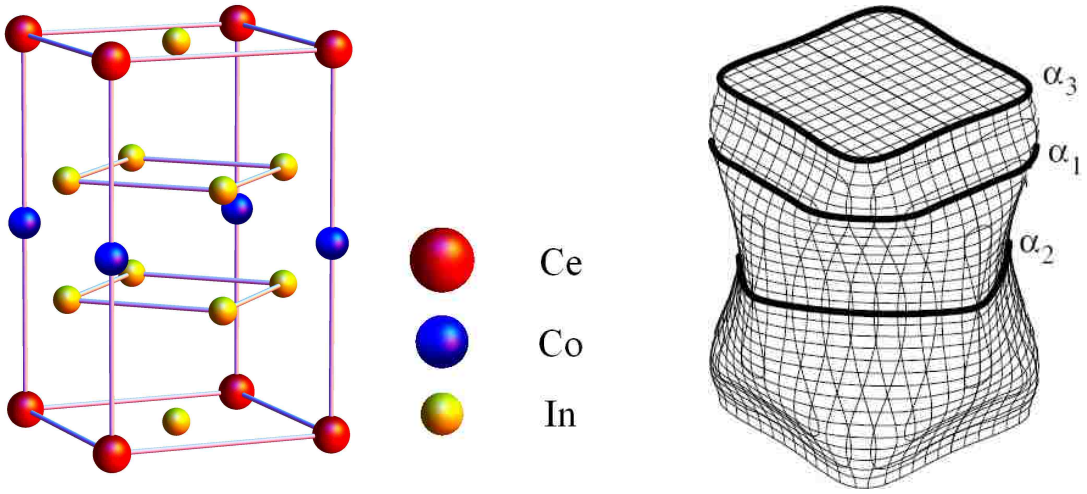

Figure 2.1: Crystal structure of $CeCoIn_5$ and the quasi-2D Fermi surface responsible for superconductivity. The atomic position for the crystal structure are taken from Ref. [17]. The Fermi surface, with the extremal orbits α_1, α_2, and α_3, is adapted from Ref. [11].

Mapping the Fermi surface by de Haas−van Alphen quantum oscillations provides one such measure of the electrons' mass [18]. In Fig. 2.1, I reproduce the Fermi surface with the largest f-electron contribution. The cyclotron masses are $m_c = 10 - 30m_e$ for the extremal orbits α_1, α_2, and α_3 [11]. An even stronger indication that the electrons are heavy comes

from measurements of the specific heat, C, where the value of the Sommerfeld coefficient, $\gamma = C/T$, is roughly proportional to the effective mass m^*.

As shown in Fig. 2.2, the normal state value is $C/T \gtrsim 300$ mJ/mol K^{-2} for $CeCoIn_5$, which is several orders of magnitude larger than the typical free-electron result. The specific heat at the superconducting transition also indicates the presence of strong interactions, since the specific heat jump $\Delta C/\gamma T_c = 4.5$ in $CeCoIn_5$ is over three times greater than the weak-coupling BCS result [9, 19].

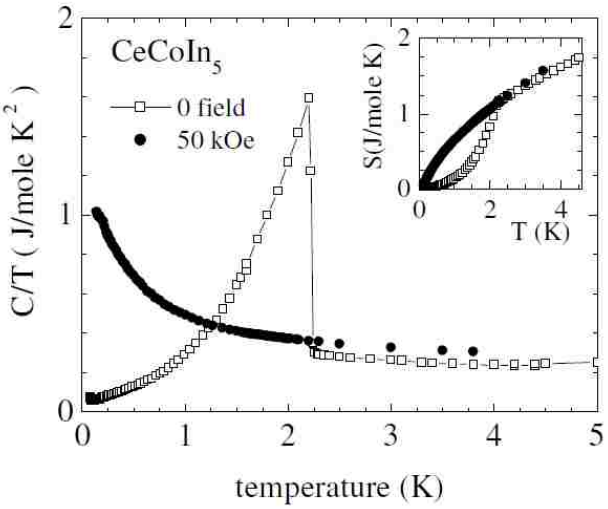

Figure 2.2: Specific heat divided by temperature vs. temperature in $CeCoIn_5$, adapted from Ref. [9]. Data is for both the superconducting state with no magnetic field (open squares) and the 50 kOe field-induced normal state (solid circles). A contribution from the indium nuclear quadrupole moment has been removed. The inset shows the entropy of the system as a function of temperature under the same magnetic field conditions.

2.1 Residual Magnetic Fluctuations

The specific heat $C = -T\partial S/\partial T$, hence the jump in C/T at T_c indicates the rate at which entropy is released at the superconducting transition. Usually, the jump in C/T at T_c is due to the formation of Cooper pairs, but any reduction in the material's entropy at T_c also contributes to the jump. Since the jump is so large for $CeCoIn_5$, one is motivated to seek out

other sources of entropy. In $CeCoIn_5$, the f-electrons that form the Kondo lattice are not completely screened by the onset of superconducting order, and the uncompensated portion of the local moments can fluctuate freely [9, 12]. Furthermore, the material's proximity to magnetic order implies the existence of low-energy magnetic fluctuations that also contribute to the entropy of the system [12, 13, 14, 15].

These experimental observations motivated Kos, Martin, and Varma to propose a simple Landau model of superconductivity that accounts for both superconductivity and thermal (Gaussian) magnetic fluctuations[20]. They included in their free energy expression a term proportional to $|\Delta|^2|\mathbf{M}|^2$, where $\mathbf{M}$ is the magnetization, to account for the competition between the two orders and integrated over the fluctuations to obtain a renormalized free energy. The competition between two orders allowed them to explain partially the large specific heat jump at $T_c(B = 0)$, but it also implied a concomitant decrease in the transition temperature T_c. This partial suppression of the zero-field transition implied an analogous suppression of the transition in an applied field, which in turn suggested that the presence of thermal magnetic fluctuations might explain other puzzling features of the phase diagram for $CeCoIn_5$ as I explain below.

2.2 Evidence of Unconventional Superconductivity

According to most experiments**refs**, superconductivity in $CeCoIn_5$ has d-wave symmetry. In addition, $CeCoIn_5$ is very near the paramagnetic limit [21]. This is because the heavy electron mass lowers the kinetic energy associated with the orbital limiting field $H_{c2,orb}$, so that superconductivity is destroyed mostly through the Zeeman-splitting of the spin-degenerate Fermi surfaces. The destruction of superconductivity through the Zeeman effect is called Pauli or paramagnetic limiting, see my discuss of this phenomenon the next chapter. The ratio between the estimated orbital critical field $H_{c2,orb}$ and the Pauli-limiting field H_P for $CeCoIn_5$ is $\sqrt{2}H_{c2,orb}/H_P \simeq 3.5$ [22]. It was also proposed that the unusual field

dependence of the vortex lattice form factor of $CeCoIn_5$ is due to the Zeeman-splitting the Fermi surfaces [23, 24]. In this limit, it is possible to realize the spatially-modulated [Fulde-Ferrell-Larkin-Ovchinnikov (FFLO)] superconducting phase. In point of fact, experiment proves the existence of a novel superconducting phase in $CeCoIn_5$ at low temperature and high fields (LTHF), see Fig. 2.3, which early experiments tentatively identified as FFLO [21, 25, 26, 27].

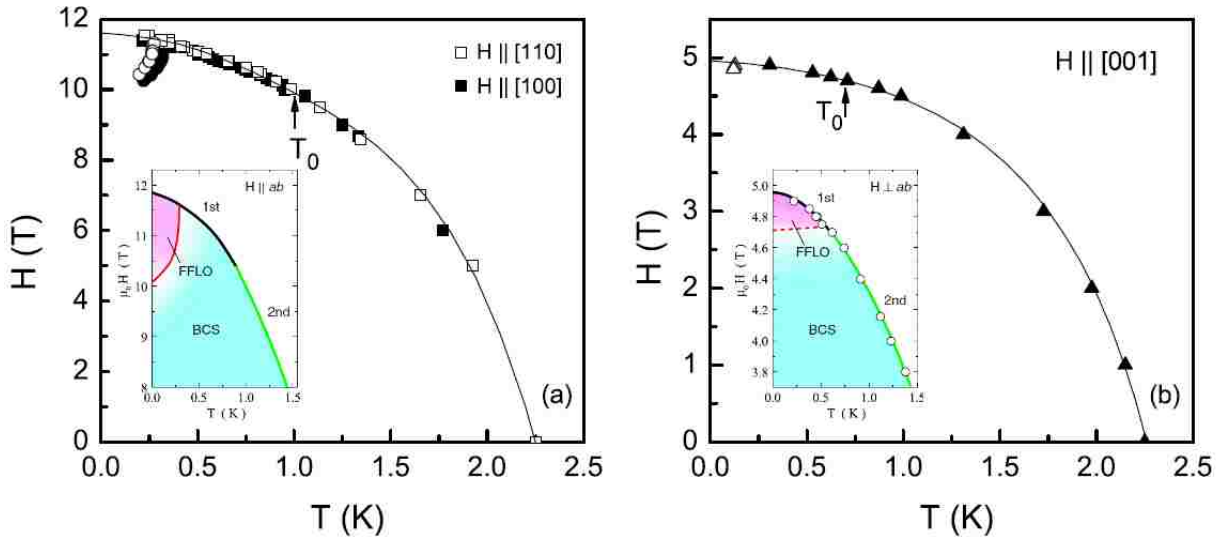

Figure 2.3: Temperature- magnetic field phase diagrams field for $CeCoIn_5$, adapted from Ref. [21]. The field directions for the left hand diagram are in the Ce-In planes while the field orientation for the right hand diagram is parallel to this plane. Insets are close ups of the LTHF phase as adapted from Ref. [28].

It is tempting to think of $CeCoIn_5$ as being in the strict paramagnetic limit, but several of the experimental features of the transition into the LTHF phase are not fit by the established theories of Pauli-limiting in two dimensions. The usual 2D theory of d-wave superconductivity in the Pauli limit predicts a second order normal-to-superconducting transition along the entire critical field line $B_c(T)$ [29]; however, experiments show that this is not the case for $CeCoIn_5$. Specifically, as I show in Fig. 2.3, the normal-to-superconducting transition in $CeCoIn_5$ becomes first order below the temperature T_0 and remains first order down to the

lowest temperatures accessible [21]. Thus the transition into the LTHF state, which occurs along $B_c(T)$ at low T.

There are theoretical predictions under which the normal-to-superconducting transition may become first order. These include strong Fermi-liquid enhancement of the magnetic susceptibility [30, 29] as well as impurity scattering in the resonant limit [31]. Also, $CeCoIn_5$ is not completely Pauli-limited [21] and superconducting fluctuations in the presence of orbital effects can drive the transition to first order over an intermediate temperature range [32, 33]. In this study, I propose a simple description of how first order transitions may naturally emerge over a part of the phase diagram. Working in the strict paramagnetic limit, I show that the competition between superconductivity and thermal magnetic fluctuations can drive the transition to first order both for the uniform and the FFLO state at intermediate temperatures. I track the suppression of the critical field $B_c(T)$ and discuss how the magnetic fluctuations affect the thermodynamics at the superconducting transition.

3. Superconductivity in the Paramagnetic Limit

3.1 The Zeeman Effect and Paramagnetic Limiting

Under a purely Zeeman field, **B**, the electron spin couples to the field, but the diamagnetic response of the superconductor to the field is irrelevant. Mathematically, the Zeeman effect is described by the Hamiltonian

$$\mathcal{H}_{\text{Zeeman}} = \sum_{\mathbf{k}} \mu B \left(c^{\dagger}_{\mathbf{k}\uparrow} c_{\mathbf{k}\uparrow} - c^{\dagger}_{\mathbf{k}\downarrow} c_{\mathbf{k}\downarrow} \right) , \tag{3.1}$$

where $\mathbf{k}$ is the electron momentum and the spin for the $c^{\dagger}_{\mathbf{k}\uparrow} c_{\mathbf{k}\uparrow}$ ($c^{\dagger}_{\mathbf{k}\downarrow} c_{\mathbf{k}\downarrow}$) is along (opposite) the magnetic field. The magnitude of electron's magnetic moment is $\mu = g\mu_B/2$, where μ_B is the Bohr magneton and g is the conduction electron g-factor. As is clear from Eq. 3.1, the electrons with spin along ('up') or opposite ('down') the Zeeman field are raised or lowered in energy, respectively, when compared to electrons in the absence of the magnetic field. Thus, with increasing **B** field, the Fermi surface for the spin-up (spin-down) electrons encloses a smaller (larger) volume in $\mathbf{k}$-space, as I show in Fig. 3.1.

This detuning of the two Fermi surfaces is in direct conflict with spin-singlet superconductivity, since paramagnetic pair-breaking occurs as the Zeeman field increases the energy of the spin-singlet with respect to spin-polarized $s = 1$. In an isotropic spin-singlet superconductor, two Fermi-level electrons with different spins pair up so that their net momentum is zero. I represent this schematically in the inset to Fig. 3.2, where the electrons reside on opposite sides of the spin-degenerate Fermi surface. If the Zeeman field polarizes the electrons and hence splits the two Fermi surfaces, then there are no Fermi-level electrons of opposite momentum with which to form the Cooper pairs; however, if the system remains in the superconducting state, then there is an energy cost equal to the paramagnetic energy

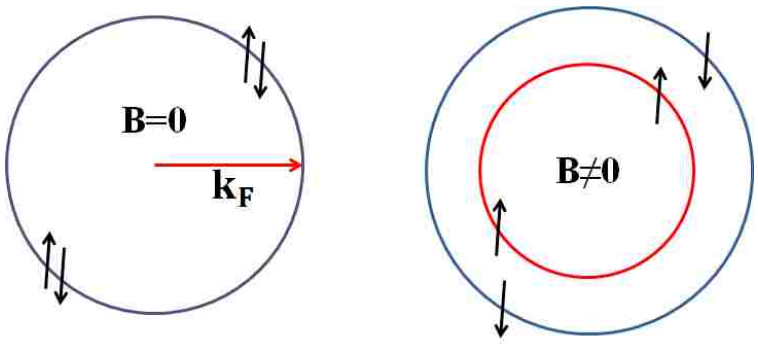

Figure 3.1: Fermi surfaces for normal-state free electrons in the absence (left) and presence (right) of a Zeeman field **B**. In the absence of the field, the Fermi surfaces are degenerate for the two spin species. A finite field increases the number of spin-down electrons and thus increases **k**-space volume enclosed by the corresponding Fermi surface. The volume enclosed by the spin-up Fermi surface decreases by an amount equal to the volume increase of the spin-down Fermi surface. Pauli-limiting occurs when the Zeeman **B** destroys superconductivity by lifting the spin degeneracy of the Fermi surfaces so that there are no electrons of opposite momentum with which to form Cooper pairs. The wave vector $\mathbf{k}_{\rm F}$ is the Fermi momentum.

of the polarized normal state. The superconductor then returns to the normal state one the paramagnetic energy cost is greater than the condensation energy of the superconducting state. This process is called paramagnetic, or Pauli, limiting.

In Fig. 3.2, I show the (T, B) phase diagram for a paramagnetically-limited system with isotropic s-wave superconductivity. The second order transition into the uniform superconducting state, $\Delta(\mathbf{r}) = \Delta_0$, becomes first order below a characteristic temperature $T_P \simeq 0.56 T_{c0}$ [34]. Here T_{c0} is the transition temperature in zero magnetic field and for which I show the derivation in Appendix A.1. At $T = 0$, superconductivity is destroyed when the energy of the polarized normal state equals the superconducting condensation energy (the Clogston[35]-Chandrasekhar[36] limit). This occurs at the Pauli field $H_P = \Delta/(\sqrt{2}\mu)$. Because the transition below T_P is first order, there is also a supercooling field below which the normal state cannot exist.

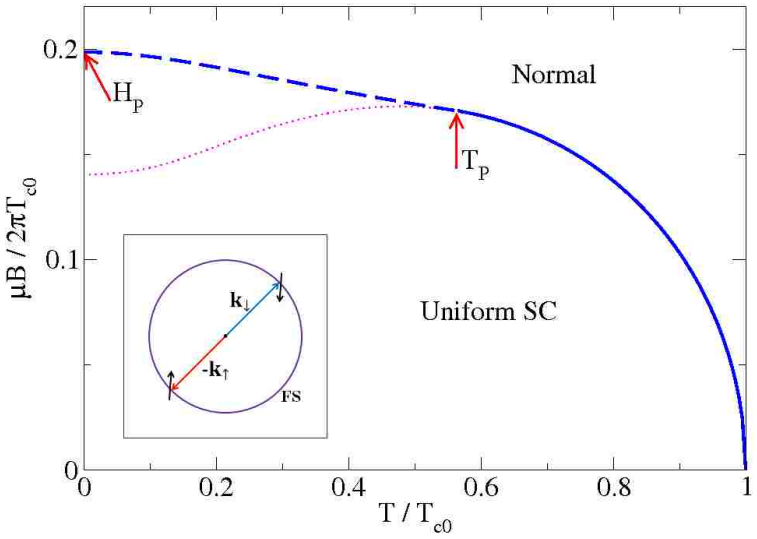

Figure 3.2: Phase diagram for spatially-uniform, paramagnetically-limited superconductivity. The transition is second order (solid blue) at high temperatures and is first order (dashed blue) at low temperatures. The supercooling field (dotted magenta) is also shown. The inset shows the zero-momentum Cooper pair on the degenerate Fermi surfaces.

3.2 Finite-Momentum Pairing and the FFLO State

An alternative to destroying the uniform superconductivity is instead to pair electrons of opposite spin on the Zeeman-split Fermi surfaces. In this situation, the Fermi-level electrons of course have the same energy but now have momenta differing by a wave vector $Q \sim \mu B/(\hbar v_F)$, where v_F is the Fermi velocity. The finite center of mass momentum of the Cooper pairs leads to a spatial modulation of the order parameter [37, 38] and allows superconductivity to survive at fields above the Clogston-Chandrasekhar limit.

One-dimensional spatial modulation of the order parameter can be of two general types: the phase-modulated Fulde-Ferrell (FF) state, $\Delta(\mathbf{r})=\Delta_0 e^{iQx}$, and the amplitude modulated Larkin-Ovchinnikov (LO) state, $\Delta(\mathbf{r})=\Delta_0 \sin(Qx)$. The phase modulation of the FF state describes a current-carrying state with an associated kinetic energy, thus the LO state is generally the energetically favorable phase.

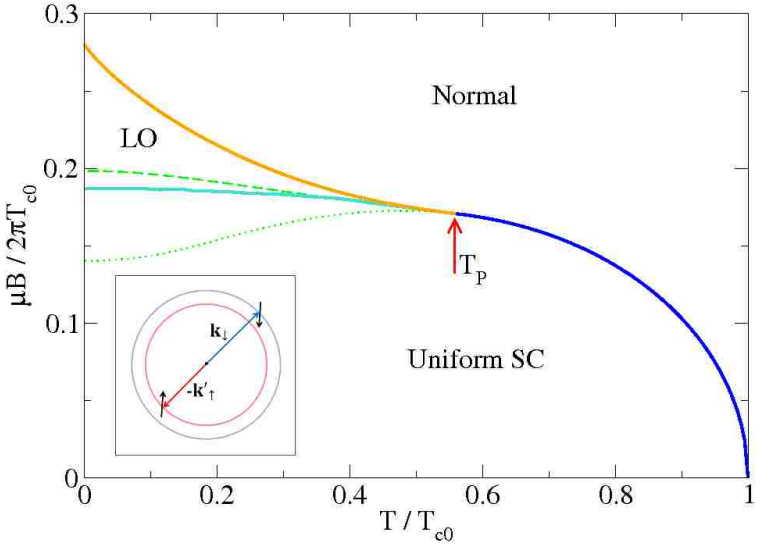

Figure 3.3: Phase diagram for 2D s-wave superconductor with LO modulation of the order parameter at low T and high B. The transition is second order into both the uniform (dark blue) and LO (orange) states. The second order transition (light blue) between the uniform and modulated states is taken from Ref. [30]. The upper critical (dashed green) and supercooling (dotted green) fields from Fig. 3.2 are shown for reference. Inset shows the nonzero-momentum Cooper pair on the Zeeman-split Fermi surfaces, and the magnitude of the modulation wave vector $\mathbf{Q}$ is $Q \sim |\mathbf{k}_\downarrow - \mathbf{k}'_\uparrow| = \mu B/\hbar v_F$.

In the analysis of one-dimensional modulation for isotropic, s-wave superconductors, the transition into the FFLO state is found to be second order in two dimensions and first order in three[30, 39, 40, 41]. In superconductors with nodes, such as d-wave $CeCoIn_5$[9, 42, 43, 44], the normal-to-FFLO transition is second order in both two[29] and three[45] dimensions. Although I do not consider the existence of a vortex lattice, it is worth noting that the transition to a combined vortex and LO state is also expected to be of the second order[46].

The predicted structure of the modulated state in s-wave systems is still not well established. In the absence of spin-orbit coupling, the direction of $\mathbf{Q}$ in real space can be chosen arbitrarily, and a superposition of plane waves with modulations along different directions may yield lower energy than for a single-mode modulation [47, 48]. In Fig. 3.3, I show the phase diagram for a two-dimensional s-wave superconductor in the paramagnetic limit, allowing for single-mode modulation of the superconducting order parameter. As shown, at

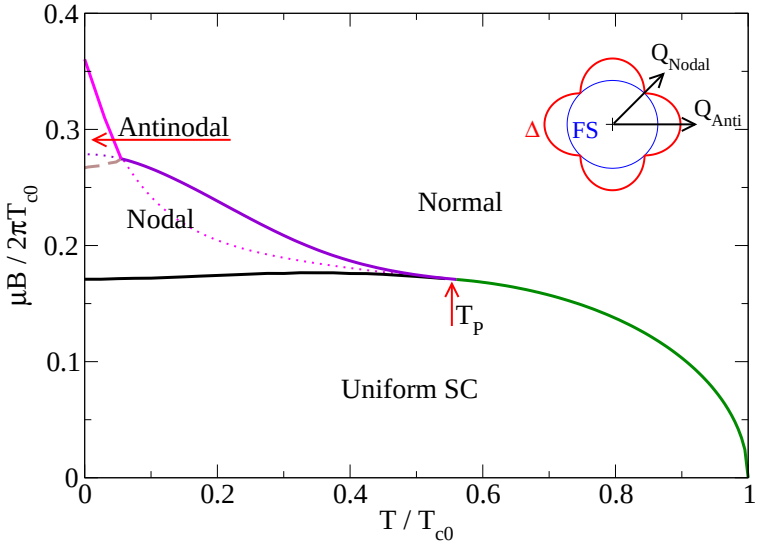

Figure 3.4: Phase diagram for 2D d-wave superconductor with LO modulation of the order parameter at low T and high B. Moving from high to low temperature, the normal-to-superconducting transition is second order into the uniform (dark green), nodally-oriented LO (purple), and anti-nodally (magenta) states. The second order transition (black) between the uniform and nodally-oriented states and the first-order transition (dashed tan) between the nodally and anti-nodally oriented states are taken from Ref. [29]. The two possible directions of the modulation wave vector $\mathbf{Q}$ are illustrated in the upper-right.

the point T_P the second order transition into the LO state preempts what would be the first order transition into uniform superconducting state and remains second order all the way down to $T = 0$. The transition between the uniform and LO states is second order, and the phase boundary between the two states meets the upper critical field at T_P.

The situation is different for systems with unconventional gap symmetry, such as d-wave systems, due to the presence of nodes in the superconducting gap [45, 49, 29, 50]. For a d-wave gap, the modulation wave vector is preferentially along either the nodal or anti-nodal direction, depending on both the temperature and the purity of the sample[29, 31]. In Fig. 3.4, I show the phase diagram for a two-dimensional d-wave superconductor with single-mode modulation, where the LO state is more advantageous than FF modulation. The transition into the modulated states below T_P is second order with the modulation along the nodal (antinodal) direction above (below) $T \simeq 0.06 T_{c0}$[29, 51, 47]. As for the s-wave system,

the transition between the uniform and modulated state is second order; however for the d-wave system there is within the superconducting phase an additional first order transition between the states with nodally- and antinodally- oriented modulation wave vector.

3.3 Microscopically-derived Landau Theory of the Paramagnetic Limit

In order to derive the Landau expansion of the free energy $\mathcal{F}$, I begin with the partition function

$$\mathcal{Z} = \mathrm{Tr}(e^{-\beta\mathcal{H}}) = e^{-\beta\mathcal{F}} \tag{3.2}$$

where $\beta = T^{-1}$, $\mathcal{H}$ is the mean-field Hamiltonian

$$\mathcal{H} = \sum_{\mathbf{k},\sigma} \epsilon_{\mathbf{k}\sigma} c^{\dagger}_{\mathbf{k}\sigma} c_{\mathbf{k}\sigma} + \frac{1}{|\lambda|} \sum_{\mathbf{q}} |\Delta_{\mathbf{q}}|^2 - \sum_{\mathbf{q},\mathbf{k}} \mathcal{Y}(\hat{\mathbf{k}}) \left(\Delta_{\mathbf{q}} c^{\dagger}_{\mathbf{k}+\mathbf{q}\uparrow} c^{\dagger}_{-\mathbf{k}\downarrow} + \Delta^{\star}_{\mathbf{q}} c_{-\mathbf{k}\downarrow} c_{\mathbf{k}+\mathbf{q},\uparrow} \right) , \tag{3.3}$$

and the trace is taken over all of the eigenstates of $\mathcal{H}$. Here $\sigma = \uparrow$ ($\sigma = \downarrow$) denotes the orientation of the electron with the spin along (opposite) to the field direction. Here $\epsilon_{\mathbf{k}}$ is the band energy measured with respect to the chemical potential so that $\epsilon_{\mathbf{k}\uparrow} = \epsilon_{\mathbf{k}} + \mu B$ and $\epsilon_{\mathbf{k}\downarrow} = \epsilon_{\mathbf{k}} - \mu B$. In Eq. (3.3), $|\lambda|$ is the strength of the pairing interaction, $\mathcal{Y}(\hat{\mathbf{k}})$ is a normalized basis function that transforms according to an irreducible representation of the crystal point group and describes the gap symmetry, and $\hat{\mathbf{k}}$ denotes position on the Fermi surface.

I assume, for simplicity, a separable pairing interaction, so that the spin-singlet order parameter is $\psi(\mathbf{k},\mathbf{q}) = \mathcal{Y}(\hat{\mathbf{k}})\Delta_{\mathbf{q}}$, with the amplitude $\Delta_{\mathbf{q}}$ self-consistently determined from

$$\Delta_{\mathbf{q}} = -|\lambda| \sum_{\mathbf{k}} \mathcal{Y}(\hat{\mathbf{k}}) \left\langle c_{\mathbf{k}+\mathbf{q}\uparrow} c_{-\mathbf{k}\downarrow} \right\rangle . \tag{3.4}$$

Here $\langle \cdots \rangle$ indicates the thermal average

$$\left\langle c_{\mathbf{k}+\mathbf{q}\uparrow} c_{-\mathbf{k}\downarrow} \right\rangle = \frac{\mathrm{Tr}(e^{-\beta\mathcal{H}} c_{\mathbf{k}+\mathbf{q}\uparrow} c_{-\mathbf{k}\downarrow})}{\mathrm{Tr}(e^{-\beta\mathcal{H}})} . \tag{3.5}$$

Uniform superconducting states have the single non-vanishing Fourier component with $\mathbf{q} = 0$, while modulated states correspond to one or more components with $\mathbf{q} \neq 0$. For simplicity, and without loss of generality, I use a model of a 2D circular Fermi surface. I use the azimuthal angle, θ, to parameterize the position on the Fermi surface, and I choose $\mathcal{Y}(\hat{\mathbf{k}}) \equiv \mathcal{Y}(\theta) = 1$ and $\mathcal{Y}(\theta) = \sqrt{2}\cos 2\theta$ for s- and d-wave gaps, respectively.

As I show in Appendix A, the gap amplitude in Eq. (3.4) has to minimize the free energy. Hence it determines, at the mean field level, the Landau expansion of the free energy density F_L in powers of $\Delta_{\mathbf{q}}$,

$$\begin{aligned} F_L = &\sum_{\{\mathbf{q}_i\}} \widetilde{\alpha}_{\mathbf{q}_i} |\Delta_{\mathbf{q}_i}|^2 + \sum_{\{\mathbf{q}_i\}} \widetilde{\gamma}_{\mathbf{q}_1,\ldots,\mathbf{q}_4} \Delta_{\mathbf{q}_1} \Delta^*_{\mathbf{q}_2} \Delta_{\mathbf{q}_3} \Delta^*_{\mathbf{q}_4} \delta_{\mathbf{q}_1+\mathbf{q}_3,\mathbf{q}_2+\mathbf{q}_4} \\ &+ \sum_{\{\mathbf{q}_i\}} \widetilde{\nu}_{\mathbf{q}_1,\ldots,\mathbf{q}_6} \Delta_{\mathbf{q}_1} \Delta^*_{\mathbf{q}_2} \Delta_{\mathbf{q}_3} \Delta^*_{\mathbf{q}_4} \Delta_{\mathbf{q}_5} \Delta^*_{\mathbf{q}_6} \delta_{\mathbf{q}_1+\mathbf{q}_3+\mathbf{q}_5,\mathbf{q}_2+\mathbf{q}_4+\mathbf{q}_6} \, . \end{aligned} \tag{3.6}$$

The coefficients of this expansion are combinations of the normal state Green's functions as described in Appendix A. The summation over $\{\mathbf{q}_i\}$ in Eq. (3.6) includes all possible combinations of the allowed Fourier components of $\Delta(\mathbf{r})$: $\mathbf{q}_i = 0$ for a uniform gap amplitude, single mode $\mathbf{q}_i = \mathbf{Q}$ for the FF modulation, and $\mathbf{q}_i \in \{\mathbf{Q}, -\mathbf{Q}\}$ for the LO phase. In the following I restrict myself to the comparison of the free energies of these three phases, finding the one most energetically favorable and the corresponding wave vector $\mathbf{Q}$.

I determine the phase transition line $B_c(T)$ by finding, at a given temperature, T, the highest B_c of the three phases I compare. In each phase I find $B_c(T) = \max(B_c(T, \mathbf{q}))$ by unrestricted maximization with respect to the modulation wave vector. To simplify my analysis, I introduce the dimensionless energy density, $f = F_L/N_F T_{c0}^2$, where N_F is the 2D normal state density of states at the Fermi level. I also introduce the dimensionless amplitude $\delta_0 = \Delta_0/T_{c0}$ where Δ_0 is the SC gap amplitude and T_{c0} is the mean-field transition temperature at $B = 0$ in the absence of magnetic fluctuations. The reduced temperature and magnetic field are given by $t = T/T_{c0}$ and $b = \mu B/(2\pi T_{c0})$ respectively, and I have set $k_B = \hbar = 1$ throughout this study.

3.3.1 Uniform Superconducting State

For the uniform state, $\Delta_{\mathbf{q}} = \Delta_0 \delta_{\mathbf{q},0}$, I find

$$f_u(T,B) = \alpha_u |\delta_0|^2 + \gamma_u |\delta_0|^4 + \nu_u |\delta_0|^6 \,, \tag{3.7}$$

with the coefficients determined from Eqs. (A.25)-(A.16),

$$\alpha_u = \ln(t) + \mathrm{Re}\left[\Psi\left(\frac{1}{2} + i\frac{b}{t}\right)\right] - \Psi\left(\frac{1}{2}\right), \tag{3.8a}$$

$$\gamma_u = -\frac{1}{8}\frac{\langle |\mathcal{Y}(\theta)|^4 \rangle_{FS}}{(2\pi t)^2} \mathrm{Re}\left[\Psi^{(2)}\left(\frac{1}{2} + i\frac{b}{t}\right)\right], \tag{3.8b}$$

$$\nu_u = \frac{1}{192}\frac{\langle |\mathcal{Y}(\theta)|^6 \rangle_{FS}}{(2\pi t)^4} \mathrm{Re}\left[\Psi^{(4)}\left(\frac{1}{2} + i\frac{b}{t}\right)\right]. \tag{3.8c}$$

Here Ψ ($\Psi^{(n)}$) is the digamma (nth order polygamma) function, and $\langle \cdots \rangle_{FS} = \int d\theta/(2\pi)$. For the s- and d-wave symmetries of the gap, Eq. (A.19), my coefficients agree with those in Refs. [39, 45].

3.3.2 Fulde-Ferrell Superconducting State

For the spatially-inhomogeneous superconducting state, the coefficients in Eq. (3.6), depend on the direction of modulation. Since the modulation wave vector $Q \sim \xi_0^{-1} \ll k_F$, for two particles at locations θ and $\pi + \theta$ on the Fermi surface, there is an energy mismatch $\mathbf{v}_F \cdot \mathbf{Q} = v_F Q \cos(\theta - \theta_Q)$, where θ_Q is the modulation direction with respect to the crystalline a axis. This energy mismatch enters in Eq. (A.25) with $\mathbf{q}_i = \mathbf{Q}$.

Recall that the polygamma functions in Eq. (3.8) originate from the summation over Matsubara frequencies, and that their argument is determined by the energy mismatch of the particles in the Green's functions in Eqs. (A.25)-(A.16). Consequently, the coefficients of the free energy expansion in the FF state are given by the same polygamma functions as for the uniform case, Eq. (3.8), but with the arguments reflecting the energy difference $\mu B + \mathbf{v}_F \cdot \mathbf{Q}$. Hence in the expansion $f_{FF}(T,B) = \alpha_{FF}|\delta_0|^2 + \gamma_{FF}|\delta_0|^4 + \nu_{FF}|\delta_0|^6$, I find

$$\alpha_{FF} = \ln(t) - \Psi\left(\frac{1}{2}\right) + \mathrm{Re}\left\langle |\mathcal{Y}(\theta)|^2 \Psi\left(\frac{1}{2} + i\frac{b+\bar{q}}{t}\right)\right\rangle_{FS}, \tag{3.9}$$

where $\bar{q} = q\cos(\theta - \theta_q)$ and $q = \xi_0 Q/2$. Similarly, γ_{FF} and ν_{FF} are given by expressions identical to Eqs. (3.8b) and (3.8c) under the replacement $b \to b + \bar{q}$ and averaging both the digamma functions and the basis functions $\mathcal{Y}(\theta)$ together over the Fermi surface.

It follows that for any anisotropic superconductor the direction of the modulation and the shape of the gap cannot be separated. For a two-dimensional d-wave superconductor that I consider, the modulation along the nodal/antinodal direction is preferred in a pure material above/below $T \simeq 0.06T_{c0}$[29, 51, 47], although as the impurity scattering is increased modulation along a node becomes favorable even for $T < 0.06T_{c0}$[31]. Therefore, below I focus on the modulation along the gap nodes.

3.3.3 Larkin-Ovchinnikov Superconducting State

For the Larkin-Ovchinnikov (LO) state, the quadratic component in Eq. (3.6) includes two terms identical to Eq. (3.9) but summed over $\mathbf{q} = \pm\mathbf{Q}$ with $\Delta_{\pm\mathbf{Q}} = \Delta_0/2$. Both terms for LO are identical when averaged over the Fermi surface, hence $\alpha_{LO} = \alpha_{FF}/2$. Thus the second order transition line, B_c, determined from $\alpha = 0$, is identical for both the FF and LO phases. The relative stability of the FF and LO phases is determined by comparing the quartic coefficients γ_{FF} and γ_{LO} at the transition, with the smaller of the two corresponding to the thermodynamically stable SC state because $f_{SC} - f_N = -\alpha^2/(2\gamma)$.

The quartic coefficient, γ_{LO}, is obtained by summing the six terms in Eq. (A.15) with $\mathbf{q}_i \in \{\mathbf{Q}, -\mathbf{Q}\}$, subject to the constraint $\delta_{\mathbf{q}_1+\mathbf{q}_3,\mathbf{q}_2+\mathbf{q}_4}$. This yields

$$\gamma_{LO} = t\mathrm{Re}\left\langle \sum_{n=0}^{\infty} |\mathcal{Y}(\theta)|^4 \frac{\bar{\omega}_{n,b}\left(3\bar{\omega}_{n,b}^2 - \bar{q}^2\right)}{128\pi^2\left(\bar{q}^2 + \bar{\omega}_{n,b}^2\right)^3} \right\rangle_{FS}, \tag{3.10}$$

where $\bar{\omega}_{n,b} = t(n + \frac{1}{2}) + ib$. Twenty distinct terms contribute to the sixth order Landau coefficient which becomes

$$\nu_{LO} = -t\mathrm{Re}\left\langle \sum_{n=0}^{\infty} |\mathcal{Y}(\theta)|^6 \frac{\bar{\omega}_{n,b}\left(\bar{q}^6 - 33\bar{\omega}_{n,b}^2\bar{q}^4 + 35\bar{\omega}_{n,b}^4\bar{q}^2 + 5\bar{\omega}_{n,b}^6\right)}{2048\pi^4\left(\bar{q}^2 + \bar{\omega}_{n,b}^2\right)^5\left(9\bar{q}^2 + \bar{\omega}_{n,b}^2\right)} \right\rangle_{FS}. \tag{3.11}$$

3.4 Determination of Transition Field and Optimal Modulation Wave Vector

For each phase, with the free energy density written as

$$f = \alpha(t, b, q)|\delta_0|^2 + \gamma(t, b, q)|\delta_0|^4 + \nu(t, b, q)|\delta_0|^6 \,, \tag{3.12}$$

I determine the critical field $b_c(T)$ and the optimal modulating wave vector q_0. I allow for possible second and first order transitions, and compare the results to determine the order of the physical transition.

The second order transition field at fixed t is the maximal value of b_c (with respect to q) for which $\alpha(t, b_c, q) = 0$, and $\gamma(t, b_c, q_0) > 0$. The corresponding optimal q_0 determines whether the transition is into a uniform ($q_0 = 0$) or modulated state. In the vicinity of the transition line

$$|\delta_0|^2 = -\frac{\alpha(t, b_c, q_0)}{2\gamma(t, b_c, q_0)} \approx \frac{\alpha'(t_c - t)}{2\gamma(t_c, b_c, q_0)} \,, \tag{3.13}$$

where $\alpha' = \partial\alpha(t, b_c, q_0)/\partial t|_{t=t_c}$. With this value I can compute the free energy difference between the normal and the superconducting states and therefore determine the thermodynamic properties such as the specific heat jump at the transition, see below.

In the region where $\gamma < 0$, the first order transition occurs once the minimum in the free energy shifts discontinuously to $\delta_0 \neq 0$ before the quadratic coefficient α changes sign [52]. This happens along the line defined by

$$\gamma^2(t, b_c, q) - 4\alpha(t, b_c, q)\nu(t, b_c, q) = 0 \,, \tag{3.14}$$

where the new minimum first appears at

$$|\delta_0|^2 = -\frac{\gamma}{2\nu} \,. \tag{3.15}$$

For example, I show in Fig. 3.5 the result of the Landau expansion for the unmodulated s-wave state in the paramagnetic limit. As shown, the Landau expansion only captures the

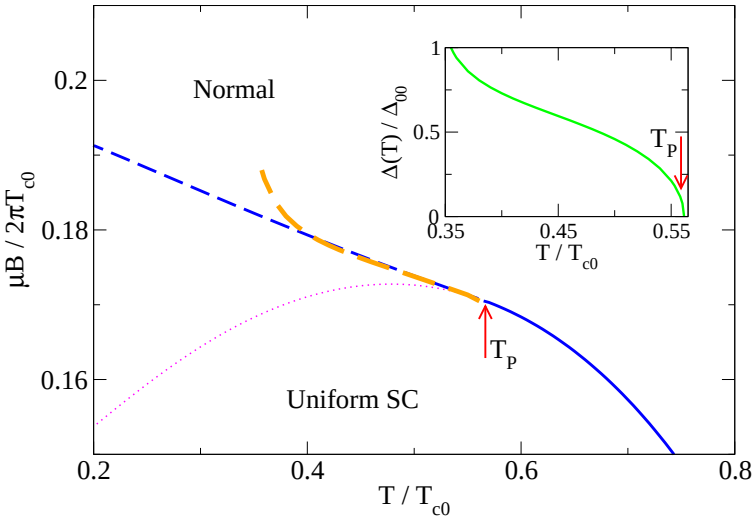

Figure 3.5: Landau theory prediction of upper critical field for s-wave system with uniform gap. The inset shows the superconducting gap amplitude along $B_c(T)$ measured with respect to Δ_{00}, the gap amplitude at zero temperature and field. The first order transition field predicted by Landau theory (dashed orange) closely follows the mean-field transition (dashed blue) provided $\Delta(T) \ll \Delta_{00}$. When $\Delta_(T)$ is large, *i.e.*, here for $T \lesssim 0.45 T_{c0}$, the Landau expansion begins to break down and incorrectly predicts $B_c(T)$. As in Fig. 3.2, the transition is second order (solid blue) for $T > T_P$ and supercooling field (dotted magenta) is also shown.

line of first order transition while $\Delta(T)$ is much smaller than the gap at zero temperature and field Δ_{00}, which I calculate in Appendix A.2 for both s- and d-wave gap symmetries.

I locate the first order transition at a given t by unrestricted maximization, with respect to q, of the field b_c that satisfies Eq. (3.14). At each temperature, I locate the maximal field $b_c(q) = b_c(q_0)$ for which the coefficient $\alpha(t, b_c, q_0) = 0$. If I find $\gamma(t, b_c, q_0) > 0$, the transition is second order. If $\gamma(t, b_c, q_0) < 0$, I maximize b_c for Eq. (3.14), checking that γ remains negative and that the free energy remains bounded from below. The latter condition requires $\nu(t, b_c, q_0) > 0$, which is satisfied throughout the region of the first order transition if the full q dependence of ν is kept, see Eq. (3.11). This is in contrast to the sixth order coefficient's changing sign within the gradient expansion. The first and second order transition lines meet at a critical point $t^\star$ where $\gamma(t^\star, b_c, q_0) = 0$. For the d-wave gap, I compare the critical fields for nodal and antinodal orientations of the modulation wave vector $\mathbf{Q}$ and verify that

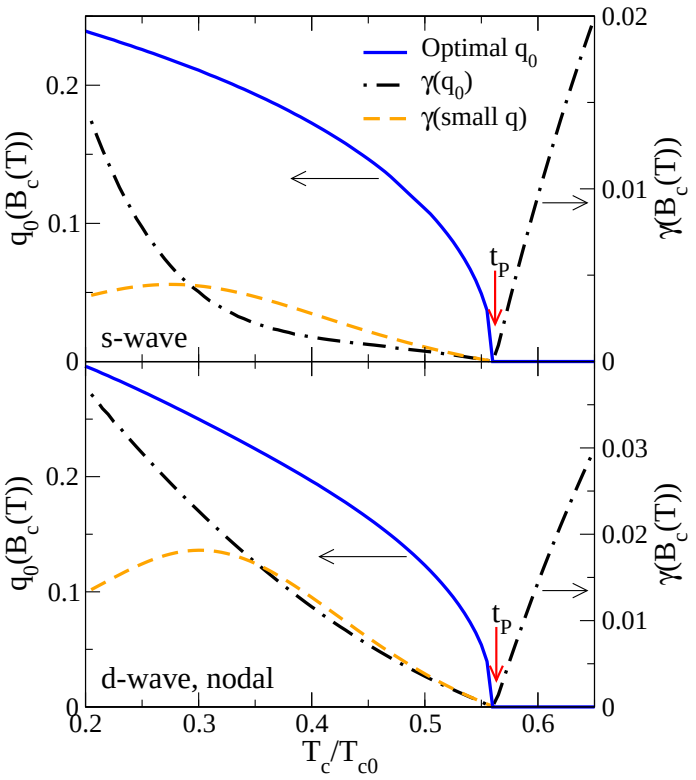

Figure 3.6: Optimal wave vector $q_0(b_c(T))$ (solid) and quartic coefficient $\gamma(B_c(T))$ (dot-dashed) obtained by unrestricted maximization of $b_c(t)$ for LO state. Quartic coefficient for small-q expansion (dashed) is also shown. Upper/lower panels are for s and d-wave (q along node) gaps.

modulation along gap nodes is preferred above $T \simeq 0.06T_{c0}$. As shown in Fig. 3.6 for LO modulation, the quartic coefficient remains positive and the transition is second order on both sides of t_P.

3.5 Gradient Expansion of the Free Energy

Analysis of the FFLO states is often carried out within the Ginzburg-Landau theory, which entails an expansion of the superconducting state free energy in both the amplitude and the gradient of the order parameter [39]. Such an expansion is justified in the immediate vicinity of T_P, but its region of validity is very narrow. I obtain the gradient expansion of the free energy by expanding Eq. (3.12) in powers of q. This requires me to expand

Eqs. (3.9)-(3.11) in powers of q while retaining the corresponding powers of $\mathcal{Y}(\theta)$. The resulting expansion

$$f = (\alpha_0 + \alpha_2 q^2 + \alpha_4 q^4)|\delta_0|^2 + (\gamma_0 + \gamma_2 q^2)|\delta_0|^4 + \nu_0|\delta_0|^6 \tag{3.16}$$

contains only even powers of q since the system is isotropic, and the coefficients in Eq. 3.16 are identical to those obtained for s-wave and d-wave superconductivity in Refs. [39] and [45], respectively. Since each subsequent term in the expansion contributes an extra qG_σ^0 in the Matsubara summation of Eqs.(A.25)-(A.15), I have $\alpha_n \propto \gamma_{n-2} \propto \mathrm{Re}(\Psi^{(n)}(\frac{1}{2} + i\frac{b}{t}))$ for $n \geq 2$. Consequently α_2 and γ_0 change sign at exactly the same temperature, $t_P = T_P/T_{c0}$, in the absence of magnetic fluctuations. The modulated state with $q_0^2 = -\alpha_2/(2\alpha_4)$ emerges at lower T via a second order transition described by

$$f = \left(\alpha_0 - \frac{\alpha_2^2}{4\alpha_4}\right)|\delta_0|^2 + \left(\gamma_0 - \frac{\gamma_2\alpha_2}{2\alpha_4}\right)|\delta_0|^4 + \nu_0|\delta_0|^6 \tag{3.17}$$

with the renormalized quartic term positive. The results obtained from an examination of Eq. (3.17) are identical to those discussed in Refs. [39, 45].

The modulation wave vector increases rapidly along $T_c(B) < T_P$ and becomes comparable to the inverse of the superconducting coherence length, $\xi_0^{-1} = [\hbar v_F/2\pi T_{c0}]^{-1}$, rendering the gradient expansion invalid. As I show in Fig. 3.6, below t_P the transition is into modulated state with the wave vector that reaches values of $q_0 \approx 0.2\xi_0^{-1}$ and higher. The gradient expansion loses accuracy as the expansion parameter increases and eventually fails when q_0 becomes too large. This failure of the expansion is manifested in the significant discrepancy between the values for the quartic coefficient at the optimal wave vector within the gradient expansion and in the full evaluation, shown in Fig. 3.6.

4. Thermal Magnetic Fluctuations

Soft magnetic modes exist in systems that are close to ordering magnetically. In the continuum limit, the fluctuations of the magnetization field $M(\mathbf{r})$ are described by the Gaussian free energy

$$\mathcal{F}_M[\mathbf{M}] = \frac{1}{2}\int d\mathbf{r}\chi^{-1}\mathbf{M}(\mathbf{r})^2\,. \tag{4.1}$$

Here I have ignored the the momentum dependence of $\chi(\mathbf{q})$, assuming the that the momenta relevant for superconductivity are $Q \sim \xi_0^{-1} \ll \pi/a$ (where a is the lattice spacing). I do not discuss here the role of the (possibly singular) antiferromagnetic (AFM) fluctuations in mediating the superconducting pairing: this role can only be addressed within the framework of specific microscopic theories[53, 54, 55]. My task is to consider the competition of superconductivity and the long-wavelength fluctuations of the magnetization, whether uniform or staggered, in systems with susceptibility χ that is much larger than the dimensionless Pauli susceptibility for typical metals $\chi_P \approx 10^{-6}$. Although the susceptibility $\chi \gg \chi_P$ is enhanced, the system is not close to ferromagnetic order ($\chi \ll 1$), hence I do not distinguish between B and the applied magnetic field H for the rest of the study. In the same spirit, I ignore $\mathbf{M}\cdot\mathbf{H}$ in the magnetic free energy since its contribution to the averaged free energy is a factor of χ smaller than the corrections I consider.

In Ref. [20] the susceptibility was taken to be temperature-dependent, in agreement with experiment [12], $\chi(T) = \chi_0 T_{sf}/(T + T_{sf})$ where T_{sf} is a characteristic energy scale for the low-energy spin fluctuations. While I make use of this expression to make contact with Ref. [20], my main results are qualitatively the same for a temperature independent χ of the same magnitude. I also ignore the field dependence of χ. Finally, I do not account for the quantum fluctuations of $\mathbf{M}$ and consider only thermal fluctuations of the magnetization.

Recall that my goal is to investigate the effects of long-wavelength magnetic fluctuations on the N-SC transition. I include the competition between magnetism and superconducting orders via the lowest order term allowed by symmetry in the free energy expansion,

$$\mathcal{F}_{sc,M}\left[\Delta,\mathbf{M}\right]=\frac{\eta}{2}\int d\mathbf{r}|\Delta(\mathbf{r})|^2\mathbf{M}(\mathbf{r})^2\,, \tag{4.2}$$

where the coupling constant $\eta>0$ makes coexistence of the two orders unfavorable. In a simple system it would be possible to determine η from microscopics, by expanding $\mathbf{B}=\mathbf{H}+4\pi\mathbf{M}$ in each Green's function in the powers of the fluctuating magnetization and introducing the correlator $\langle\mathbf{M}(\mathbf{r})\mathbf{M}(\mathbf{r}')\rangle$ that is proportional to the susceptibility, in analogy with Ref. [56]. Such an expansion produces an $M^2|\Delta|^2$ term. In a complex system with f-electrons I cannot determine the coefficient of this term microscopically, and I use Eq. (4.2) with a phenomenological parameter η to explore the salient features of the model. My consistency checks on the choice of η are the magnitudes of the jump in Δ_0 and of $\Delta M/M$ across the first order transition line. I find maximal $\Delta_0(T_c)\lesssim 0.3\Delta(0)$ and $\Delta M/M\approx 1-5\%$ everywhere along the first order transition line. These values are moderate, hence my choice of η is physically reasonable.

To verify the generality of my results, I examined the coupling of the SC order parameter to higher order terms in $M(\mathbf{r})^2$ and its gradients, *e.g.* $|\Delta(\mathbf{r})|^2|\nabla M(\mathbf{r})|^2$, and, within the small-$q$ approximation, to gradients of the order parameter itself, *e.g.* $|\nabla\Delta(\mathbf{r})\cdot\mathbf{M}(\mathbf{r})|^2$. I checked that, while these various couplings renormalize the transition temperature, they do not introduce new features into the phase diagram.

To derive the effective theory for the superconducting order, I integrate out the magnetic fluctuations from the partition function

$$\mathcal{Z}=\exp\left[-(\mathcal{F}_L+\mathcal{F}_{sc,M}+\mathcal{F}_M)/T\right]\equiv e^{-\mathcal{F}_L/T}\overline{\mathcal{Z}}_{sc,M}\,,$$

where $\mathcal{F}_L=\int d^D\mathbf{r}F_L$. I obtain the total free energy

$$\overline{\mathcal{F}}=\mathcal{F}_L-T\ln\overline{\mathcal{Z}}_{sc,M}\,, \tag{4.3}$$

where the magnetic contribution is

$$\overline{\mathcal{Z}}_{sc,M} = \int \mathcal{D}[\mathbf{M}(\mathbf{r})] \exp\left[-\frac{1}{T}\left(\mathcal{F}_{sc,M} + \mathcal{F}_M\right)\right], \tag{4.4}$$

and $\mathcal{D}[\mathbf{M}(\mathbf{r})]$ indicates integration over all possible configurations of magnetization. The integral is Gaussian in $\mathbf{M}$, hence I compute it analytically and expand in powers of $|\Delta|^2$ to obtain the corrections due to magnetic fluctuations to the expansion coefficients in F_L. Below I address these corrections in each of the three phases I consider: uniform, FF, and LO.

4.1 Uniform and Fulde-Ferrell Superconducting States

Integrating out the fluctuating magnetization for a uniform order parameter, Δ_0, is straightforward. I work with the Fourier components of the magnetization, $\mathbf{M}_\mathbf{k}$, and restrict the sum

$$\mathcal{F}_{sc,M} + \mathcal{F}_M = \sum_{|\mathbf{k}|<k_c} \frac{1}{2}\left(\chi^{-1} + \eta|\Delta_0|^2\right)|\mathbf{M}_\mathbf{k}|^2, \tag{4.5}$$

to one-half of k-space since $\mathbf{M}_\mathbf{k} = \mathbf{M}^\star_{-\mathbf{k}}$ for real $\mathbf{M}(\mathbf{r})$. Therefore from Eq. (4.4) I have, after Gaussian integration over both real and imaginary parts of $\mathbf{M}_\mathbf{k}$,

$$\overline{\mathcal{Z}}_{sc,M} = \prod_{|\mathbf{k}|<k_c} \left(\frac{2\pi\chi T}{1+\eta\chi|\Delta_0|^2}\right)^{\frac{d}{2}}, \tag{4.6}$$

where now the product is taken over all $\mathbf{k}$ up to the cutoff of the order of the lattice spacing $|\mathbf{k}_c| = \pi/l$, and d is the dimensionality of magnetization vector $\mathbf{M}$.

Neutron scattering [57] measurement of the dynamic spin susceptibility in $CeCoIn_5$ shows evidence of spin fluctuations, and light Cd-doping [15] induces AFM order at $Q_{AFM} = (.5, .5, .5)$ [58]. Sister compound $CeRhIn_5$ exhibits AFM order at $Q_{AFM} = (.5, .5, .297)$ [59], which is stable under pressure [60, 61], before SC preempts AFM order at $P \approx 2$GPa [62]. Furthermore, the pressure dependence of T_c and T_N for $CeRhIn_5$ and Cd-doped $CeCoIn_5$ is nearly identical [15] suggesting that the SC and magnetic orders in both are closely related.

Hence I conclude that $CeCoIn_5$ is in proximity to 3D magnetic ordering, and I take $d = 3$ for the purposes of this study.

The corresponding contribution to the free energy is $\mathcal{F}_M(\Delta_0) = -T \ln \overline{\mathcal{Z}}_{sc,M}$. Subtracting the average magnetic contribution to the normal state energy, $\overline{\mathcal{F}}_M(\Delta_0 = 0)$, I find an additive contribution to the superconducting free energy density

$$\begin{aligned} F_{uni,M} &= \frac{\overline{\mathcal{F}}_{uni,M}(\Delta_0) - \overline{\mathcal{F}}_{uni,M}(0)}{L^D} \\ &= \frac{3}{2}\frac{T}{L^D}\sum_{k<k_c} \ln\left(1 + \eta\chi|\Delta_0|^2\right) \\ &= \frac{3}{2}\frac{T}{l^D} \ln\left(1 + \eta\chi|\Delta_0|^2\right) , \end{aligned} \tag{4.7}$$

where L^D is the volume. The last line of Eq. (4.7) follows from $\sum_k a \approx a(L/l)^D$ where a does not depend on k. Expanding this contribution in powers of $|\Delta_0|$ for my 2D superconductor ($D = 2$), I find the renormalized coefficients of $f = F/(N_F T_{c0}^2)$, Eq. (3.12),

$$\overline{\alpha}_u = \alpha_u + \frac{3}{2} t \frac{T_{c0}}{N_F l^2} \eta\chi(T), \tag{4.8a}$$

$$\overline{\gamma}_u = \gamma_u - \frac{3}{4} t \frac{T_{c0}^3}{N_F l^2} \eta^2\chi^2(T), \tag{4.8b}$$

$$\overline{\nu}_u = \nu_u + \frac{1}{2} t \frac{T_{c0}^5}{N_F l^2} \eta^3\chi^3(T)\,, \tag{4.8c}$$

where α_u, γ_u, and ν_u are given in Eqs. (3.8a)-(3.8c).

Since in the FF state, $\Delta(x) = \Delta_0 e^{iQx}$, only the phase of the order parameter is modulated, the coupling between the magnetization and the superconducting order, Eq. (4.2), has exactly the same form as in the uniform state. Hence the renormalized expansion coefficients are obtained from Eqs. (4.8) by a direct substitution of α_{FF}, γ_{FF}, and ν_{FF} for α_u, γ_u, and ν_u, respectively.

4.2 Modulated Larkin-Ovchinnikov State

In the LO state, in addition to the order parameter $\Delta(x) = \Delta_0 \cos(Qx)$ competing with the average magnetization, the amplitude modulation couples the magnetic fluctuations at

wave vectors differing by $2Q$. Therefore, the magnetic contribution to the free energy is

$$\mathcal{F}_{sc,M} + \mathcal{F}_M = \sum_{|\mathbf{k}|<k_c} \left[\frac{1}{2} \left(\chi^{-1} + \frac{1}{2}\eta|\Delta_0|^2 \right) |\mathbf{M_k}|^2 - \frac{\eta}{8}|\Delta_0|^2 \mathbf{M_k} \cdot \left(\mathbf{M}^\star_{\mathbf{k}+2\mathbf{Q}} + \mathbf{M}^\star_{\mathbf{k}-2\mathbf{Q}} \right) \right] . \quad (4.9)$$

After integrating out the fluctuations, the contribution to the superconducting free energy density relative to the normal state becomes

$$\overline{F}_{LO,M} = \frac{3}{2}\frac{T}{L^D} \sum_{k<k_c} \left[\ln\left(1 + \frac{1}{2}\eta\chi|\Delta_0|^2 \right) + \ln\left(1 - \frac{1}{8}\eta^2\chi^2|\Delta_0|^4 + \frac{1}{8}\eta^3\chi^3|\Delta_0|^6 \right) \right] . \quad (4.10)$$

The first term differs from its counterpart in Eq. (4.7) by the factor of 1/2, arising from the spatial average of $\cos^2(Qx)$. The second term arises from the mode-mode coupling terms in Eq.(4.9) and is derived in Appendix B. Under expansion in Δ_0, it only contributes to the fourth and sixth order terms in the free energy, and I obtain

$$\overline{\alpha}_{LO} = \alpha_{LO} + \frac{3}{4} t \frac{T_{c0}}{N_F l^2} \eta\chi(T), \quad (4.11a)$$

$$\overline{\gamma}_{LO} = \gamma_{LO} - \frac{3}{8} t \frac{T_{c0}^3}{N_F l^2} \eta^2\chi^2(T), \quad (4.11b)$$

$$\overline{\nu}_{LO} = \nu_{LO} + \frac{1}{4} t \frac{T_{c0}^5}{N_F l^2} \eta^3\chi^3(T) , \quad (4.11c)$$

where α_{LO}, γ_{LO}, and ν_{LO} are given in Sec. 3.3.3.

Comparing Eqs. (4.8) and (4.11), I see that the free energy expansion depends on η and χ only through their product $\eta\chi$. Thus, for subsequent analysis I define a dimensionless coupling parameter

$$\tilde{\eta} = \frac{3}{2}\frac{T_{c0}}{N_F l^2}\eta = \frac{3}{2} T_{c0} T_F \eta , \quad (4.12)$$

where the characteristic temperature $T_F = (N_F l^2)^{-1}$ is of the order of the Fermi temperature in the system. I also define a dimensionless parameter based on the experimental fit of $\chi(T) = \chi_0 T_{sf}/(T + T_{sf})$

$$\tilde{\chi} = \chi_0 \frac{T_{sf}}{T_{c0}} . \quad (4.13)$$

With these parameters, the renormalized quadratic coefficients in Eqs. (4.8a) and (4.11a) become simpler, *e.g.*,

$$\bar{\alpha}_u = \alpha_u + \tilde{\eta}\tilde{\chi}\frac{t}{t+t_{sf}}\,. \tag{4.14}$$

The renormalization of all other Landau coefficients is determined by the product $\tilde{\eta}\tilde{\chi}$, and, in simplifying the fourth and sixth order terms in Eqs. (4.8) and (4.11), I introduce the parameter $t_F = T_F/T_{c0}$.

I note that the dimensionality of the magnetization vector $\mathbf{M}$ enters the Landau coefficients as a prefactor of the coupling parameter η. Throughout this paper, I take $d = 3$. Using a different value for d simply decreases the magnetic fluctuation contributions in Eqs. (4.8) and (4.11) by a factor of $d/3$. For example, taking $d = 2$ only requires that I use $3\eta/2$ to obtain the same results (*e.g.*, T_c) as for η and $d = 3$. Hence, I proceed with my choice $d = 3$ without any loss of generality.

4.3 Choice of Energy Scales and Coupling Parameters

The exchange of entropy between the magnetic fluctuations and superconductivity reduce the zero-field transition temperature from the unrenormalized T_{c0} to the experimentally observed $T_c(\eta > 0)$ as determined from the instability condition

$$0 = \overline{\alpha}_u = \ln\left(\frac{T_c}{T_{c0}}\right) + \frac{3}{2}T_c T_F \eta\chi\,. \tag{4.15}$$

The extra entropy is released in a specific heat jump that exceeds the BCS value,

$$\frac{\Delta C/T_c(\eta)}{N_F T_{c0}^2} = -\frac{\partial^2 f}{\partial T^2}\bigg|_{T_c(\eta)} = \frac{[\bar{\alpha}'(\eta)]^2}{2\bar{\gamma}(\eta)}\bigg|_{T_c(\eta)}\,, \tag{4.16}$$

where $f(\eta)$ is the dimensionless free energy for the given coupling, η, and $\bar{\alpha}' = \partial\bar{\alpha}(T)/\partial T$. Without magnetic fluctuations, BCS mean field theory predicts for s-wave gap $\Delta C/C_N = 12/7\zeta(3) \approx 1.43$ and for d-wave gap $\Delta C/C_N = 8/7\zeta(3) \approx 0.95$ at T_{c0}. Here C_N is the normal state specific heat, and $\zeta(3) \approx 1.202$ is the Riemann zeta function. Measuring the

jump relative to the s-wave value, I find for $B = 0$

$$\frac{\Delta C/T_c(\eta)}{1.43 C_N/T_{c0}} = \left.\frac{\left(1+\frac{3}{2}T_c T_F \eta\left(\chi + T_c\chi'\right)\right)^2}{\langle|\mathcal{Y}(\theta)|^4\rangle - \frac{3(2\pi)^2}{7\zeta(3)}T_c^3 T_F \eta^2\chi^2}\right|_{T_c} \tag{4.17}$$

where $T_c = T_c(\eta)$ and $\chi' = \partial\chi(T)/\partial T$. Using Eq. (4.15) to eliminate η I find

$$\frac{\Delta C/T_c}{1.43 C_N/T_{c0}} = \frac{\left(1+\frac{(\chi+T_c\chi')}{\chi}\ln\left(\frac{T_{c0}}{T_c}\right)\right)^2}{\langle|\mathcal{Y}(\theta)|^4\rangle - \frac{4(2\pi)^2}{21\zeta(3)}\frac{T_c}{T_F}\ln^2\left(\frac{T_{c0}}{T_c}\right)}, \tag{4.18}$$

in zero field. I discuss the field dependence of $\Delta C/T_c$ in Section 5.2.1.

From the experimentally measured behavior of the susceptibility, specific heat jump $\Delta C/T_c(B = 0)$, and T_c one can estimate T_{c0} provided a reasonable guess about the value of T_F can be made. For my purposes, I take $T_c = 2.3K$, $T_F = 40K$ (the Kondo coherence temperature for $CeCoIn_5$[63]), and the dimensionless $\chi_0 \approx 10^{-4}$ (presented in units of emu/g in Ref. [12]). I follow the example of Ref. [20] and set $T_{sf} = 1.5K$. With this choice $T_{sf} < T_c$, and I examine the effects of χ which varies substantially with temperature below T_c. Experiment, however, suggests a weaker temperature dependence of $\chi(T)$ with $T_{sf} \approx 3.5T_c$[12]. Therefore, I verify that my general results are independent of the details of χ by comparing this case with the analysis for constant susceptibility. For my chosen energy scales, I solve Eq. (4.18) with $\Delta C/T_c = 3\Delta C/T_{c0}$. This gives for s-wave $T_{c0} = 6.20K$ and $\tilde{\eta}\tilde{\chi} \simeq 1.6$ and for d-wave $T_{c0} = 9.27K$ and $\tilde{\eta}\tilde{\chi} \simeq 2.3$.

5. Effects of Magnetic Fluctuations on the Normal-to-Superconducting Transition

Using the formalism outlined above, I am now in a position to investigate the changes appearing in the transition lines of the superconductor coupled to the magnetic fluctuations. In the following I set T_F, T_{sf}, and T_{c0} as described at the end of the previous section. I adjust the coupling η to the magnetic fluctuations as well as the temperature dependence of the magnetic susceptibility. I first address the nature of the transition along the $B_c(T)$ line, and then consider the thermodynamic signatures of these transitions.

5.1 Normal-to-Superconducting Transition in an Applied Zeeman Field

Quite generally, coupling to magnetic fluctuations suppresses the transition temperature, since, as is clear from Eq. (4.2), the finite thermal average of $\mathbf{M}^2(\mathbf{r})$ makes the appearance of superconductivity energetically costly. This is also evident from Eqs.(4.11a) and (4.8a), which show positive additive contribution to the quadratic coefficients in the Landau expansion. In the absence of the field, when $\alpha(T) = -\ln T/T_{c0}$, it follows from Eq.(4.15) that the transition temperature T_c satisfies

$$\left.\frac{T_c}{T_{c0}}\right|_{B=0} = e^{-\frac{3}{2}T_c T_F \eta\chi(T_c)} = \exp\left(-\frac{\tilde{\eta}\tilde{\chi}\,T_c}{T_c + T_{sf}}\right), \tag{5.1}$$

where in the last step I explicitly invoked the temperature dependence of the susceptibility. For small $\tilde{\eta}\tilde{\chi}$ the linearized form of this equation coincides with that used in Ref. [20].

At the same time the results for the quartic coefficient, Eqs.(4.11b) and (4.8b) show that it is renormalized *downward* by the magnetic fluctuations. Since the sign of this term controls whether the transition is of the second or first order, it seems possible that the order of the transition may change as the strength of the magnetic fluctuations increases.

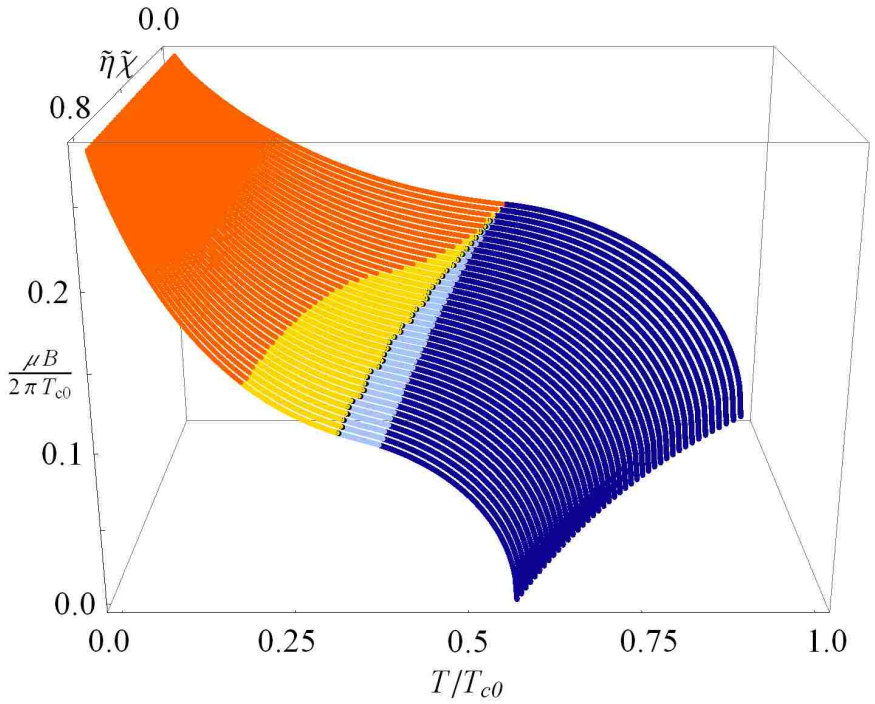

Figure 5.1: The normal-to-superconducting transition in s-wave superconductors under a Zeeman field. Magnetic fluctuations, $\tilde{\eta}$, modify the B_{c2} transition, showing four distinct regions (for increasing T): second order into modulated, first order into modulated, first order into uniform, and second order into uniform states.

Figures 5.1 through 5.3 show that this is indeed the case: coupling to magnetic fluctuations opens a region of first order transition from the normal to both uniform and the modulated superconducting state. This finding is a major conclusion of my work, and qualitatively fits with the behavior of $CeCoIn_5$ where the transition becomes first order below $T_0 \approx 1$K[22], while the putative FFLO-like phase does not occur until a lower temperature[21].

To understand this behavior recall that in the absence of fluctuations [34, 39, 45] the quartic term of the Ginzburg-Landau expansion for the uniform superconducting phase changes sign, $\gamma_u(T_P) = 0$ exactly at the point along the $B_c(T)$ line (at temperature T_P) where the modulated phase, reached via a second order transition, $\alpha_{LO}(T_P) = 0$, becomes allowed. Coupling to the fluctuations increases α_{LO} and lowers γ_u ensuring that the first order transi-

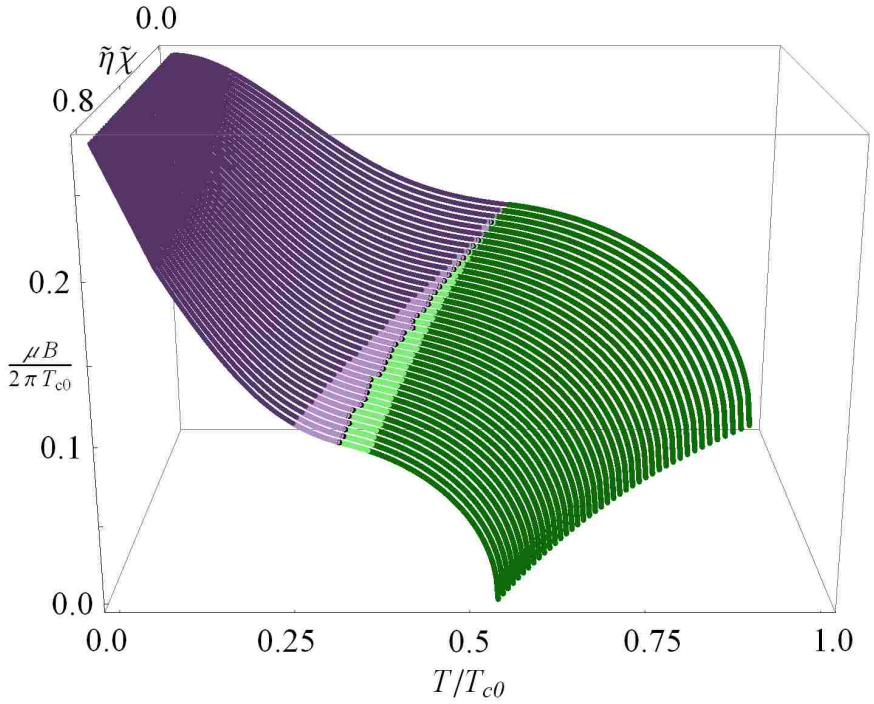

Figure 5.2: The normal-to-superconducting transition in d-wave superconductors under a Zeeman field. Order parameter modulation is along gap node. Magnetic fluctuations, $\tilde{\eta}$, modify the B_{c2} transition, showing four distinct regions (for increasing T): second order into modulated, first order into modulated, first order into uniform, and second order into uniform states.

tion in the uniform state occurs at higher temperature than that where the modulated phase can form.

Since I use the expansion in powers of δ_0, I can only estimate the location of the first order transition line away from the critical points at which the transition becomes second order. However, since the jump in δ_0 across the first order transition is modest this estimate is quite reliable. For example, the jump is $\delta_0(t_c) \lesssim 0.3\delta_0(0)$ for s-wave gap symmetry, with $\delta_0(0) = \pi e^{-\gamma_E} \approx 1.76$ as I derive in Appendix A.2. I denote by t_{LO} my estimate of the temperature along $b_c(t)$ where the first order transition lines into the uniform and the LO phases meet. For $t < t_{LO}$, the transition (first or second order) is into the amplitude-modulated phase, while the transition is into a uniform phase for $t > t_{LO}$. I also define the temperatures $t_P^\star$ and

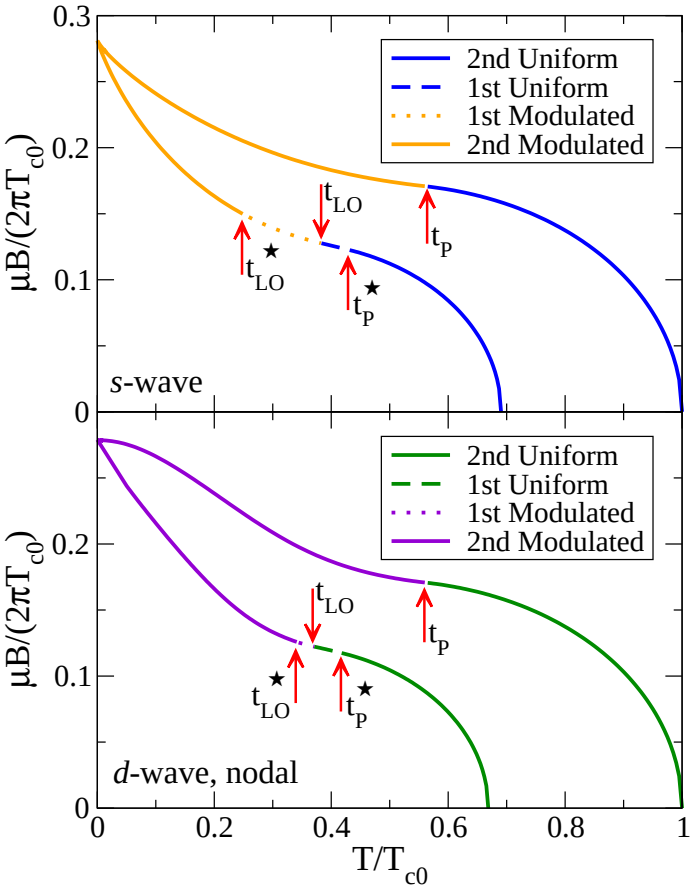

Figure 5.3: Normal state to superconducting state transition lines for s- and d-wave with nodally-oriented $\mathbf{Q}$. Upper curves are in the absence of fluctuations, and lower curves are for $\tilde{\eta}\tilde{\chi} = 0.5$.

$t^{\star}_{LO}$ where the second order transitions into the uniform and LO modulated superconducting states, respectively, become first order. In the absence of fluctuations, the temperatures coincide so that $t^{\star}_{P} = t^{\star}_{LO} = t_{LO} = t_{P}$.

As is seen from Figs. 5.1 through 5.3, the region of the first order transitions widens as the fluctuations become softer (χ increases) or compete more strongly (η increases) with superconductivity. I find that for s-wave order the region of the first order transition, for the same values of the coupling and magnetic susceptibility, is wider than for s-wave. This can be qualitatively explained by examining the quartic Landau coefficient for both symmetries in the absence of fluctuations, shown in Fig. 5.4. In the vicinity of T_P, the coefficient $\tilde{\gamma}$ is

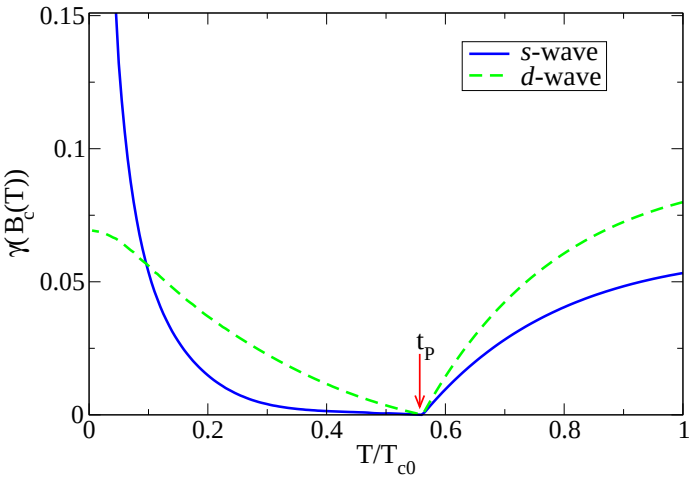

Figure 5.4: Quartic Landau coefficient evaluated along $B_c(T)$ for s-wave and d-wave symmetries with LO modulation for $t < t_P$ and uniform state for $t > t_P$.

numerically smaller for an s-wave order parameter than for d-wave, both on the uniform and the modulated (with the wave vector Q yielding maximal B_c for each symmetry) side of the transition. Hence it is easier to drive an s-wave system to first order transition.

Note that for d-wave SC I find that the modulation of the order parameter along the gap nodes is stabilized even below $T = 0.06T_{c0}$, where, in the absence of fluctuations, the anti-nodal direction would be more advantageous [49, 51, 29]. The anti-nodal modulation still gives a lower free energy at very low temperatures, below a threshold that depends on the parameter $\tilde{\eta}\tilde{\chi}$, but that occurs far from the first order transition range on which I am focusing here. Therefore for the rest of this study, I discuss only d-wave SC where $\mathbf{Q}$ is oriented along a gap node.

I find that the main result, *i.e.*, the region of the first order transition, does not depend on the detailed temperature dependence of $\chi(T)$. For comparison, I also considered the constant susceptibility $\chi_1 \equiv \chi(T_c)$ so that, for a given coupling strength $\tilde{\eta}$, I obtain the same T_c. In Fig. 5.5, I compare the critical field and order of transition for $\chi(T)$ and constant χ_1. Since $\tilde{\eta}\chi_1 < \tilde{\eta}\chi(T)$ for all $T < T_c$, superconductivity is suppressed *less* and $B_c(T)$ is higher for constant susceptibility. However, in both cases the product $\tilde{\eta}\chi < 1$, and the

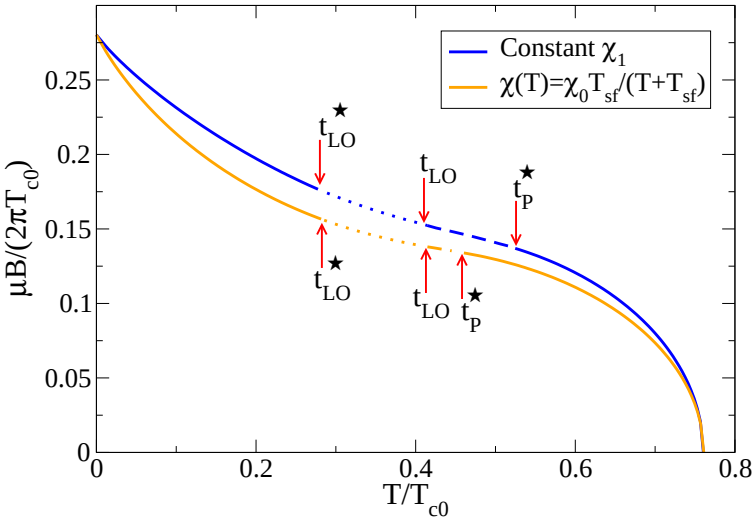

Figure 5.5: S-wave critical field $b_c(t)$ for both constant $\chi(t)$ and $\chi_1 \equiv \chi(t_c)$ for $t_c = 0.76$. Upper and lower curves are for χ_1 and $\chi(t)$, respectively. The critical field is suppressed less for χ_1 since $\tilde{\eta}\chi_1 < \tilde{\eta}\chi(t)$ at $t < t_c$. As $\tilde{\eta}\chi < 1$ for both cases, the region of first order transitions is larger for χ_1.

magnetic fluctuations have a *larger* effect for constant susceptibility than for $\chi(T)$ on the fourth Landau coefficient where $\tilde{\eta}\chi$ enters quadratically. Thus, the N-SC transition is first order over a wider temperature range for constant susceptibility. While both the exact temperature range of first order transition and the degree of $B_c(T)$ suppression depends on the temperature dependence of χ, the *presence* of these effects is independent of the details of the susceptibility. Furthermore, the thermodynamics of the transition are similar for both χ_1 and $\chi(T)$ where the only significant difference is the low-T behavior of the specific heat jump for d-wave as discussed below.

To some extent, all of the phase transitions can be predicted by a small-q expansion of the Landau free energy, which is valid in the immediate vicinity of the onset of the transition into modulated superconducting state [64]. As I show in Fig. 3.5, the gradient expansion can capture the second order transitions only over a moderate temperature range below t_P in the absence of magnetic fluctuations. Therefore, the gradient expansion can estimate the onset of the first order transitions only when the coupling $\tilde{\eta}\tilde{\chi}$ is small enough so that

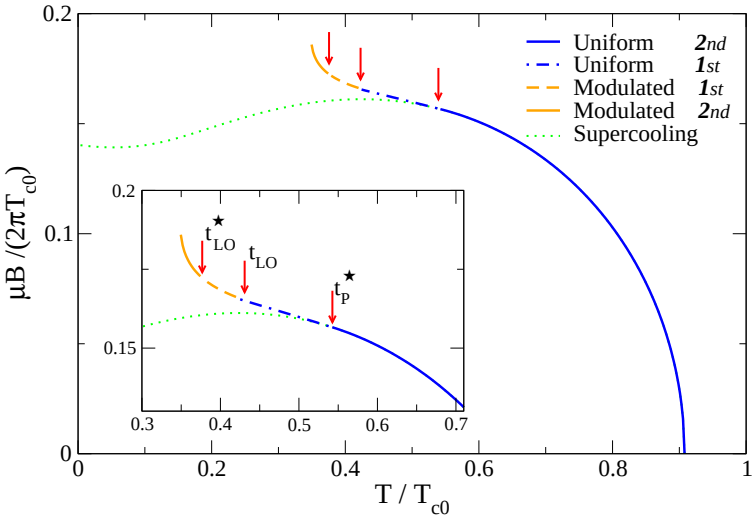

Figure 5.6: Normal-to-superconducting transition lines for s-wave superconductivity as predicted by the small-q expansion of Landau free energy with $\tilde{\eta}\tilde{\chi} = 0.15$. Magnetic fluctuations introduce first order normal-to-superconducting transitions into both the uniform and the modulated superconducting states. The inset is a closeup of the region around t_{LO}, and the temperatures $t^{\star}_{LO}$, t_{LO}, and $t^{\star}_{P}$ are explained in the text.

$t^{\star}_{LO}$ and $t^{\star}_{P}$ remain close to t_P. In Fig. 5.6, I show the results of the gradient expansion for s-wave superconductivity with $\tilde{\eta}\tilde{\chi} = 0.15$, and, as shown, the first order transitions into the uniform and modulated states are clearly present. However, as I show in Fig. 5.7, the optimal wave vector found via the small-q approximation diverges not far below $t^{\star}_{LO,grad}$, where $t^{\star}_{LO,grad}$ is the value of $t^{\star}_{LO}$ predicted by the gradient expansion. Due to this limitation, the gradient expansion breaks down and incorrectly predicts that the first-order transition exist over a smaller temperature range than is predicted by the full theory. Furthermore, the limitations of the gradient expansion also prevent me from locating the low-temperature first- and second-order transitions into modulated state. Hence, this is why I use the fully-q dependent Landau theory that I have presented above.

My main conclusion thus far is therefore that coupling to thermal magnetic fluctuations drives the normal-to-superconducting transition to first order along $b_c(t)$ in the vicinity of the onset of the modulated state. Importantly, the transition is first order on both sides of

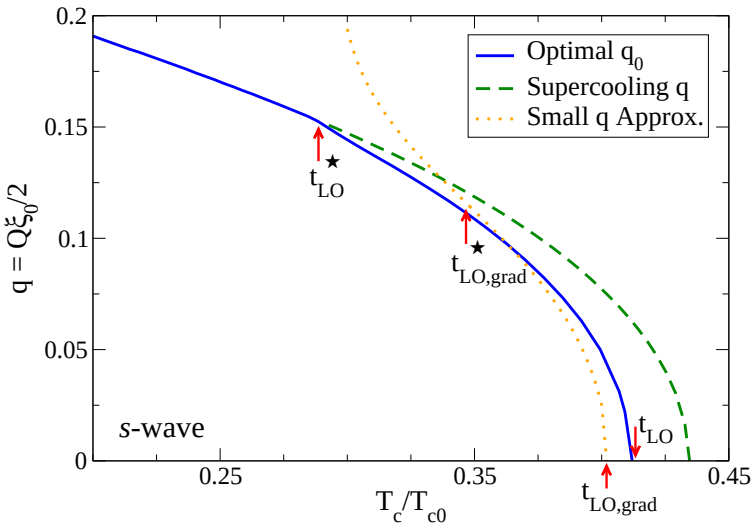

Figure 5.7: The optimal wave-vector q_0 at the normal-to-superconducting transition for s-wave system with $\tilde{\eta}\tilde{\chi} = 0.4$ as determined by both the full theory (solid blue line) and the small-q expansion (dotted orange line). The small-q approximation predicts $t_{LO,grad}$ and $t^{\star}_{LO,grad}$. The rapid increase in q_0 below $t^{\star}_{LO,grad}$ indicates the breakdown of the small-q expansion near the point where $\alpha_4 \propto \nu \to 0$, see Ref. [64].

this point, *i.e.*, I find first order transitions both in the uniform and into the LO state. At lower temperatures the transition to the inhomogeneous superconducting state is second order. This is natural within my picture since the thermal fluctuations "die out" as the temperature is lowered. Within the present framework I cannot determine whether, should the quantum dynamics of the magnetization be accounted for, the transition would remain first order to the lowest temperatures. However, since $t^{\star}_{LO} \approx 0.5t_c$ for d-wave order parameter (Figs. 5.1, 5.2, and 5.3), it appears likely that the LO transition becomes second order again at high enough temperatures so that the quantum fluctuations are unlikely to have a major effect. I now investigate the thermodynamic signatures of these transitions.

5.2 Thermodynamics at the Normal-to-Superconducting Transition

5.2.1 Specific Heat Jump at the Second Order Transition

The specific heat jump, measured relative to the BCS s-wave value, at the second order normal-to-superconducting transition along $B_c(T)$ is given by

$$\frac{\Delta C/T_c(\eta)}{1.43C/T_{c0}} = \frac{7\zeta(3)}{8\pi^2}\,\frac{(\bar{\alpha}')^2}{2\bar{\gamma}}\bigg|_{T_c,B_c,Q_0} . \tag{5.2}$$

Here again the prime denotes the temperature derivative, and the quadratic and quartic coefficients are determined from Eqs. (4.8) and (4.11) evaluated at the transition point and optimal modulation vector Q_0. The results are presented in Fig. 5.8 for the s and d-wave superconductors.

Not surprisingly, the specific heat jump diverges on approaching the first order transition region. Note that in the absence of fluctuations, even though the transition remains second order throughout, there is a singularity in $\Delta C/T_c$ due to the vanishing of the quartic coefficient at T_P. The shoulder in the specific heat in the modulated state is found both with and without coupling to the magnetic moment, and hence simply reflects the details of the variation of the coefficients and the modulation wave vector with temperature.

Of more interest is the low temperature behavior. While for s-wave superconductors the specific heat jump vanishes as $T \to 0$ for both $\eta = 0$ and $\eta \neq 0$, for the d-wave symmetry the same jump is a) finite for $\eta \neq 0$, and b) exhibits a minimum at the lowest T.

The key to understanding this behavior is in evaluating the $T = 0$ limit of the coefficients α_{LO} and γ_{LO}, which can be done analytically as detailed in Appendix C. Note that the classical fluctuations disappear at $T = 0$, as evidenced by the linear in t fluctuation corrections in Eqs. (4.8) and (4.11) and that the values of b_c and Q_0 at $t = 0$ do not depend on η or χ. For s-wave symmetry, the optimal wave vector and critical field are $Q_{0,s} = e^{-\gamma_E}\xi_0^{-1} \approx 0.56\xi_0^{-1}$

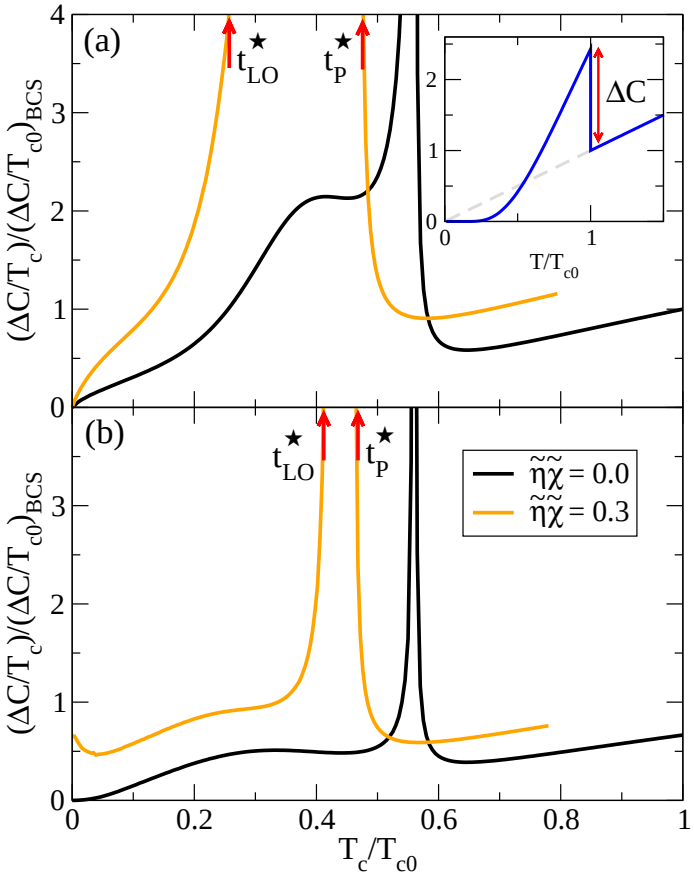

Figure 5.8: (Specific heat jump at second order normal-to-superconducting transition for (a) s-wave and (b) d-wave symmetries with $\tilde{\eta}\tilde{\chi}$ =0.0, 0.3. Inset: Specific heat jump ΔC at second order normal-to-superconducting transition.

and $b_{c,s} = e^{-\gamma_E}/2 \approx 0.28$ ($\gamma_E \approx 0.577$ is Euler's constant) at zero temperature, respectively. I find that for the s-wave case in the absence of fluctuations at $Q_{0,s}$, the quartic coefficient γ_{LO} diverges as $(b^2 - (Q_{0,s}/2)^2)^{-3/2}$ as the field approaches $b_{c,s}$ (see Eq. (C.10)). Hence $\Delta C/T_c = 0$ at zero temperature irrespective of the value of η.

In contrast, I find that at zero temperature the optimal wave vector for the d-wave gap is

$$Q_{0,d} = e^{-\gamma_E} \exp\left[\frac{\sqrt{3}-1}{4}\right] \xi_0^{-1} \approx 0.67\xi_0^{-1}\,, \tag{5.3}$$

with $b_{c,d}/(2Q_{0,d}\xi_0) = (1+\sqrt{3})/4)^{1/2} \approx 0.83$, and the coefficient $\gamma_{LO}(T=0) = 0.07$ remains finite for all values of η. The vanishing of the specific heat jump in the absence of magnetic

fluctuations is now due to the vanishing of α' at $T = 0$ (discussed in Appendix C.0.2). The temperature slope of the quadratic term, $\bar{\alpha}'(0) = \alpha'_{LO}(0) + \tilde{\eta}\chi(0)$, increases as η becomes finite, and this leads to a finite value of $\Delta C/T_c$ for d wave order in the limit $T \to 0$ in the presence of the fluctuations.

The negative slope at $t = 0$ of the specific heat jump for d-wave (Fig. 5.8(b)), is due to the temperature dependence of χ. To explain this, I expand Eq. (5.2) in t to find

$$\frac{\Delta C/T_c}{\Delta C/T_{c0}} \simeq \frac{7\zeta(3)}{8\pi^2}\left(\frac{(\bar{\alpha}')^2}{2\bar{\gamma}} + \frac{\bar{\alpha}'\left(2\bar{\gamma}\bar{\alpha}'' - \bar{\gamma}'\bar{\alpha}'\right)}{2\bar{\gamma}^2}t\right) \tag{5.4}$$

where all the derivatives and $\bar{\gamma}$ are evaluated at $t = 0$.

As discussed in Appendix C.0.2, for d-wave symmetry the quadratic derivative $\bar{\alpha}'(0) = \tilde{\eta}\chi(0)$ is positive while the quartic derivative $\bar{\gamma}'(0) = -(\tilde{\eta}\chi(0))^2/(6t_F)$ is negative at low t. The second order quadratic derivative is $\bar{\alpha}''(0) = \alpha''_{LO}(0) + 2\tilde{\eta}\chi'(0)$ with $\alpha''_{LO}(0) \approx 4.54$ and $\chi' = -\tilde{\chi}/t_{sf}^2$ is always negative for $\chi(T)$. Hence, with $\chi(T)$, the initial slope at $t = 0$ of the specific heat jump is determined by how strongly the fluctuations compete with superconductivity. As shown for $\tilde{\eta}\tilde{\chi} = 0.3$ in Fig. 5.8(b), moderate coupling is sufficient to make prominent the dip in the specific heat jump for d-wave at low temperatures. For constant susceptibility, however, $\chi' = 0$, and the specific heat jump always increases from its value at $t = 0$.

5.2.2 Entropy and Magnetization at the First Order Transition

Between $t_P^\star$ and $t_{LO}^\star$, where the transition is first order, I compute the entropy jump, $\Delta S = -\partial f/\partial t$, at the transition, and show it in Fig. 5.9(a). From Eq. (3.12), the entropy jump is

$$\begin{aligned} -\Delta S &= \left[\frac{\partial\alpha}{\partial t}|\delta_0|^2 + \frac{\partial\gamma}{\partial t}|\delta_0|^4 + \frac{\partial\nu}{\partial t}|\delta_0|^6\right]_{t=t_c} \\ &= -\frac{\partial\alpha}{\partial t}\frac{\gamma}{2\nu} + \frac{\partial\gamma}{\partial t}\left(\frac{\gamma}{2\nu}\right)^2 - \frac{\partial\nu}{\partial t}\left(\frac{\gamma}{2\nu}\right)^3 \end{aligned} \tag{5.5}$$

with $|\delta_0|^2 = -\gamma/(2\nu)$ at the first order transition. As the effective coupling parameter between magnetism and superconductivity, $\tilde{\eta}\tilde{\chi}$, grows, more and more entropy is transferred at T_c from the magnetic fluctuations to superconductivity, and the entropy jump increases. I find, as expected, that ΔS is largest in the vicinity of t_{LO}, where δ_0 takes its maximum value, and is on the order of a few percent of the entropy difference between the SC state at $T = 0$ and the normal state at $T_c(B = 0)$. I also find that δ_0 is moderate at the first order transition, with its largest value $\delta_0(t_{LO}) \approx 0.3\delta_0(t = 0, b = 0)$, and the results of my small δ_0 expansion make physical sense.

The mismatch in the entropy jump in Fig. 5.9(a) at t_{LO} results from averaging the LO gap amplitude over the system size in the limit $q = 0$. Near t_{LO}, the wavelength $\lambda_{FFLO} = \pi\xi_0/q$ of $\Delta(x)$ becomes comparable to the system size, and the profile of the order parameter near t_{LO} resembles a single kink [30, 29] profile that describes the uniform-modulated transition within the SC phase. Below t_{LO} the modulation vector q_0 rises rapidly along $b_c(t)$, and the spatial averaging of the order parameter is justified away from the immediate vicinity of t_{LO}. Therefore I expect that a calculation free of the single-mode ansatz, will give a greater entropy jump for the modulated state in the immediate vicinity of T_{LO}.

Since at the first order transition γ changes sign, I expand this coefficient near $t_P^\star$ and $t_{LO}^\star$ along the transition line, $\gamma = g_i(t_c - t_i^\star)$ where g_i is positive (negative) near $t_i = t_P^\star$ ($t_{LO}^\star$). I find that, near the tricritical points,

$$-\Delta S = S_N(t_c) - S_{SC}(t_c) \simeq \frac{-g_i}{2\nu}\frac{\partial\alpha}{\partial t}\bigg|_{t_c}(t_c - t_i^\star)\,, \tag{5.6}$$

where S_N and S_{SC} are the entropy in the normal and SC states, respectively. Hence $-\Delta S$ increases linearly in $t_c - t_i$ as seen in Fig. 5.9(a). This behavior may be tested experimentally in magnetocaloric measurements.

Exactly at the points $t_P^\star$ and $t_{LO}^\star$, the entropy difference between the normal and the superconducting states is zero. Instead, there is a rapid release of entropy upon lowering

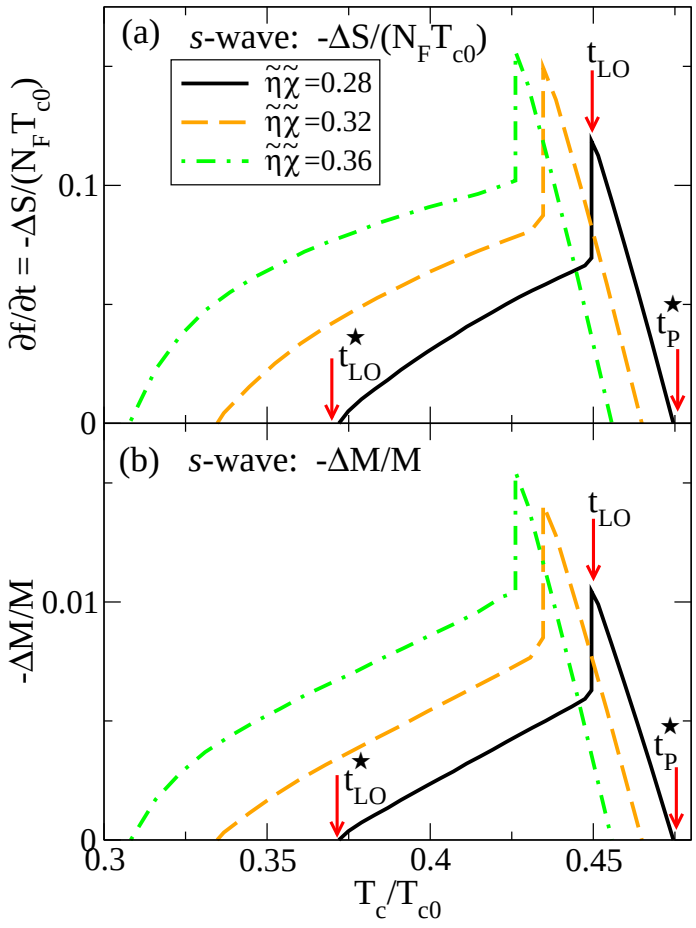

Figure 5.9: Thermodynamics at the first order normal-to-superconducting transition for s-wave with $\tilde{\eta}\tilde{\chi}$ =0.28, 0.32, and 0.36. Shown are (a) decrease in entropy and (b) decrease in susceptibility. Temperatures $t_P^\star$, t_{LO}, and $t_{LO}^\star$ are labeled for $\tilde{\eta}\tilde{\chi} = 0.28$.

the temperature at a fixed field, and entering the SC state. Near $t_P^\star$ and $t_{LO}^\star$, both the quadratic and quartic Landau coefficients are small and can be expanded about $t_i^\star$, namely $\alpha = a_i(t - t_i^\star)$ and $\gamma = g_i(t - t_i^\star)$. I then find

$$|\delta_0|^2 = \frac{-g_i(t - t_i^\star) \pm \sqrt{g_i^2(t - t_i^\star)^2 - 3a_i\nu(t - t_i^\star)}}{3\nu} \tag{5.7}$$

and, sufficiently close to $t_i^\star$, $|\delta_0|^2$ is dominated by the temperature dependence of the second term under the square root. Thus, the entropy relative to the normal state varies with temperature as

$$S_{SC}(t) - S_N(t) \simeq -\frac{3}{2}\sqrt{\frac{a_i^3}{3\nu}}\sqrt{t_i^\star - t}\,, \tag{5.8}$$

where $S_{SC}(t)$ and $S_N(t)$ are the entropy in the SC and N states, respectively.

To further test the validity of my parameter choices, I calculate

$$M/H = \left(\chi^{-1} + \eta|\Delta_0|^2_{ave}\right)^{-1} \tag{5.9}$$

along the first order N-SC transition. Here $|\Delta_0|^2_{ave}$ is the spatial average of the SC order parameter. I find that magnetization is suppressed by the onset of superconducting order (see Eq. (4.2)) as entropy is transferred between their respective degrees of freedom. The fractional change in magnetization is

$$\frac{\Delta M}{M} = -\frac{\eta\chi(T)|\Delta_0|^2_{ave}}{1+\eta\chi(T)|\Delta_0|^2_{ave}} \tag{5.10}$$

across the transition. This jump, as shown in Fig. 5.9(b), resembles the entropy jump in Fig. 5.9(a), which makes sense as both quantities depend on the value $|\Delta_0|$ takes upon entering the SC state. Thus, the jump in δ_0 across the transition may be revealed by measuring both $\Delta M/M$ and ΔS along the line of first order transition.

Since I include fluctuations phenomenologically, it is possible that the first order transitions are due to an unreasonable choice of the coupling parameter η such that the magnetization is strongly renormalized. As a check on the validity of my model, I verify that the magnetization does not change drastically at the N-SC transition. As shown in Fig. 5.9(b), the relative change in M/H at a first order transition is generally less than a few percent and validates my method of including the magnetic fluctuations.

6. Superconductivity in the Iron-Based Materials

Given the typically antagonistic relationship between superconductivity and magnetism, it came as a surprise in 2008 when Kamihara, *et al.*, reported the discovery of high-temperature superconductivity, T_c=26 K, in fluorine-doped LaFeAsO [16]. It is so well known that elemental iron is strongly magnetic that the spontaneous parallel magnetic ordering of local moments is called ferromagnetism after *ferrum*, the Latin word for iron. Thus, the presence of superconductivity, much less high-temperature superconductivity, in an iron-based material was wholly unexpected. This discovery gave birth to the study of iron-based superconductivity, which has remained at the forefront of research for the past three years.

Superconductivity in the iron-based material is possible because the Fe-moments order antiferromagnetically rather than ferromagnetically; therefore, the iron moments do not provide a macroscopic magnetic field to interfere with superconductivity. The Fermi-level charge carriers in LaFeAsO originate primarily from *d*-electrons donated by the irons in the Fe-As plane [65], and the antiferromagnetic fluctuations of the irons sublattice are likely the mechanism by which pairing occurs [8]. Thus, it seems that the presence of iron and its proximity to antiferromagnetic order are key to superconductivity in LaFeAsO.

Within a year of Kamihara's announcement, many other iron-based materials were reported [16, 66, 67, 68, 69]. In Figure 6.1, I show the four most common structural classes in which superconductivity has been found. Each of these materials has a layered structure based upon planar, tetrahedrally-coordinated Fe-M layers where M is either a pnictide or chalcogenide. Pnictides are elements in the nitrogen column of the periodic table (Group 15), *e.g.*, phosphorous and arsenic, while the chalcogenides are from the oxygen column (Group 16), *e.g.* selenium and tellurium. The so-called 11 materials (FeSe, FeTe) are comprised of a

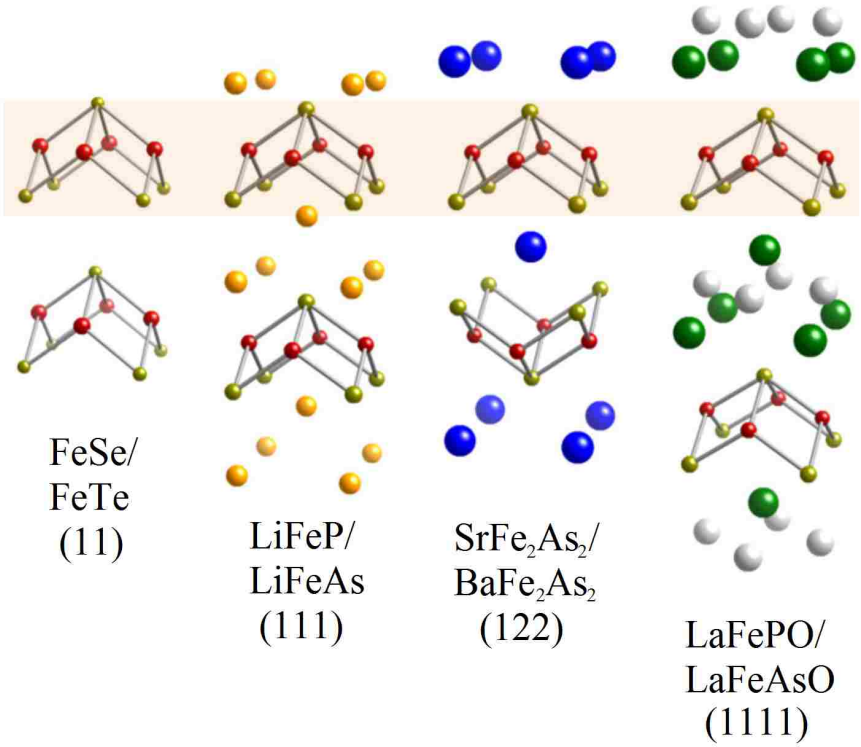

Figure 6.1: Common crystal structures for the Fe-based superconductors, adapted from Ref. [70]. The shaded box highlights the Fe-M layer common to all of the materials. The numerical labeling scheme corresponds to the stoichiometric ratios of the constituent elements.

simple layering of the Fe-M planes. In the 111, 122, and 1111 materials the Fe-M layers are separated by so called 'blocking layers' composed alkali, alkaline earth, or rare earth metals and oxygen or fluorine. See Figure 6.1 for an explanation of the numerical labeling scheme.

6.1 Electronic Structure

The charge carriers in the iron-based superconductors reside primarily in the Fe-M planes, hence their electrical properties are quasi-two dimensional. Furthermore, since the M atoms are staggered below and above the plane, the crystalline unit cell is doubled with respect to the underlying iron lattice. This results in a crystallographic Brillouin zone that is half the size of the zone for the iron atoms alone. In the pnictides, all five d-orbitals of iron contribute

to the density of states at or very near the Fermi surface [65, 71, 72], which can be modeled with two [73] or four [74, 75] bands, of hole-like (over half-filled) and electron-like (under half-filled) nature. Band structure calculations predict a Fermi surface that consists of at least four separate sheets, two each of the hole and electron types, that are located at the center and corners of the crystallographic zone respectively [76, 77, 74, 75, 65, 71, 72]. The general features of these calculations are borne out in experiment.

Angle-resolved photoemission (ARPES) measurements studies on LaFePO [72], in fluorine-doped NdFeAsO [78], and potassium-doped $BaFe_2As_2$ [79] show the basic structure of two hole sheets at the zone center and two electron sheets at the corners. This confirms the basic topology of the Fermi surface sheets, but ARPES is a surface probe and is not capable of determining the detailed dependence of the sheets on $\mathbf{k}_z$, the momentum perpendicular to the material surface. On the other hand, quantum oscillation experiments can probe the cross-sections of the Fermi surface along the crystalline c-axis, and such experiments performed on the 122-type materials $SrFe_2As_2$ [80] and $BaFe_2As_2$ [81, 82] also confirm the general features of the band structure calculations. In Figure 6.2, I show the Fermi surface of $BaFe_2As_2$ as calculated by density functional theory [71] and as measured by de Haas−van Alphen oscillations [81].

6.2 Unconventional Multi-band Superconductivity

There are two main scenarios for the A_{1g} pairing state in the iron-based superconductors. In the first, pairing is magnetically-mediated which requires a sign change between the order parameter on different parts of the Fermi surface. Unlike $CeCoIn_5$, however, this does not immediately imply the existence of gap nodes on any one Fermi surface sheet. In the first situation, proposed three months after superconductivity in LaFeAsO was reported, Mazin, *et al.* [8], and Kuroki, *et al.* [76], suggest that the near nesting of the electron and hole FS sheets leads to predominantly interband pairing with a change in the sign of the order

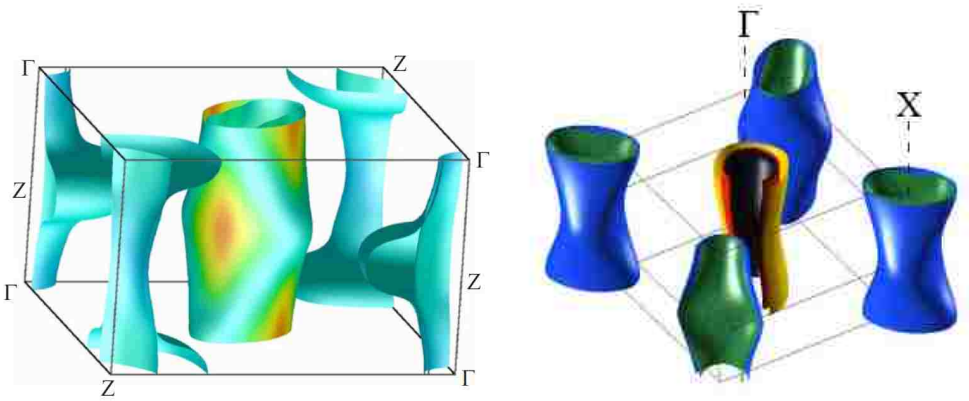

Figure 6.2: Quasi-two dimensional Fermi surfaces in the iron-based superconductors. The figures are for $BaFe_2As_2$ as calculated by density functional theory [71] and as calculated to fit quantum oscillation measurements [81]. The experimentally determined Fermi surface is on the right. Note that the high-symmetry Γ point is at the corner of the figure on the left and at the center of the figure on the right.

parameter between FS sheets of different type. For the pnictide structure, this proposed order parameter is of the "extended" s-wave type. This so-called s_{+-} state, quickly caught on as a leading contender for the gap symmetry, and several groups have attempted to obtain the momentum dependence of the anisotropic energy gap from various calculations. The results range across several different types of order parameter: possible nodes on both Fermi surface sheets [83]; a combination of strongly anisotropic or nodal gap on the electron sheet with nearly isotropic gap on the hole sheet [84, 77, 85, 86, 87, 88]; and nearly isotropic, full superconducting gaps on all of the FS sheets [89, 90]. In the second, more recently suggested scenario, orbital fluctuations due to spatial oscillation of the Fe atoms promote pairing with the same sign of the order parameter on the FS sheets [91]. There are many indications that the order parameter has the full symmetry of the lattice [76, 87, 85, 89, 90, 77, 84, 92, 93]. one detailed study showed, however, that the extended s-wave and the d-wave pairing states can be nearly degenerate in energy [77], which indicates that the detailed physics of any one system might tip the balance in favor of one symmetry state or the other.

The experimental situation is also far from clear, and there is an emergent consensus that the gap structure is non-universal for different compounds and across doping ranges [94, 95, 70]. ARPES experiments measure isotropic or nearly isotropic gaps on all FS sheets in the 122-type materials [79, 96, 97, 98] and in fluorine-doped NdFeAsO [78]. Penetration depth measurements indicate both full and nodal superconducting gaps, depending on the material [99, 100, 101, 102, 103, 104, 105, 106, 107]. Transport measurements [108, 109, 110, 107] and nuclear magnetic resonance (NMR) studies [111, 112, 113] suggest the presence of line-nodes in 1111-type materials and phosphorous-doped $BaFe_2As_2$ while indicating fully-gapped superconductivity in other 122-type materials. Note that even if the interactions favor a nodal state in a pure compound, lifting of the nodes due to disorder may occur [114, 115]. Hence determination of the structure of the gap remains an important goal, with many studies suggesting experimental signatures of the various gap symmetries [87, 116, 117, 118, 119, 120, 121, 75, 122, 123, 124].

6.3 Resonant States Near a Single Impurity

Historically, some of the most detailed theoretical and experimental studies of the consequences of the nodal gap have been carried out for the cuprate superconductors. Scanning tunneling spectroscopy measurements near impurity sites played a significant role in testing our understanding of the superconducting state, see Ref. [125] for review. Prediction [126, 127] and subsequent observation [128, 129] of the bound states via scanning tunneling spectroscopy (STS) at and around impurities was an important milestone in understanding superconductivity in the copper based systems. The analysis of the spatial dependence the states (DOS) around the impurity provided insights into nodal structure of the gap [125], and I show the both a calculated and an experimentally measured impurity-induced state in Fig. 6.3.

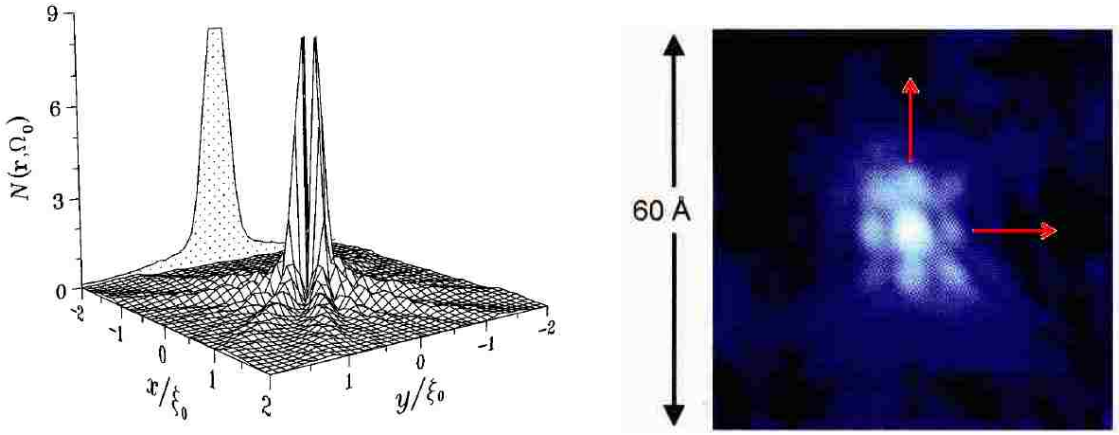

Figure 6.3: The resonance state in the d-wave cuprates near a non-magnetic impurity. The figure on the left is the spatial profile as first presented in Ref. [130]. The figure on the right, adapted from Ref. [128], is scanning tunneling microscopy data for a zinc impurity on the surface of $Bi_2Sr_2CaCuO_{8+\delta}$. The arrows for the experimental data show the direction of the gap nodes in real space.

It is with this in mind that I pursue my study of the single-impurity effect in the iron-based superconductors. I consider the formation of bound states around non-magnetic impurities in multiband extended s-wave superconductors, and focus on the gap symmetries and parameter values relevant to iron-based materials. Several recent studies have also considered this problem but have failed to reach a consensus on the nature of the resonant state [131, 75, 132, 123, 121, 133, 133, 134]. Here I provide a comprehensive analysis of the single-impurity problem combining analytical and numerical techniques. I consider the conditions for the existence of well-defined resonance states and analyze the spatially-resolved density of states around the impurity site for different shapes of the gap in the A_{1g} representation. I take the gap on the hole FS to be isotropic and investigate the consequences of the gap anisotropy on the electron sheet. I allow for an isotropic gap, deep gap minima, and gap nodes, and I compare the results for different gap shapes while emphasizing the salient features expected in STS measurements. I demonstrate that the energy of the impurity states for similar gap structures is sensitive to the details of the band structure of the material. I explain

the physics behind these effects and provide experimentally testable predictions for future tunneling studies.

7. Basic Models of Multiband Systems

As discussed in Chapter 6, all five d-orbitals of iron contribute to the density of states (DOS) at or very near the Fermi surface [65, 71, 72], and the number of bands crossing the chemical potential depends on the specific compound, doping, and other details. Consequently one faces the choice of either using the results of the *ab-initio* calculations for a given material or considering a simplified band structure that contains features common to the entire family. Both approaches have their respective merits, and I take the latter route since it allows me to combine analytical and numerical techniques in a controlled way.

Motivated by the quasi-2D nature of the pnictides, I restrict my analysis to a two-dimensional Brillouin Zone (BZ). The salient feature I include is the existence of the hole Fermi surface (FS) sheet around the Γ point, and the electron FS sheet at the M and equivalent points. As described in Section 6.1, the crystallographic unit cell contains two irons and the resulting BZ shown in 6.2 for a representative compound. It is often useful, however, to 'unfold' the Brillouin zone into one twice the size of the physical BZ, and this is the representation that I show schematically in Fig. 7.1. Note that in the unfolded BZ picture, the M point corresponds to the middle of the BZ boundary.

In the simplest model there is one [73], and in a more realistic description two [74, 75, 76, 77] FS sheets of each type. The two-band model is well-suited to an analytical description in the continuum, while the four-band model is more representative of the electronic structure of the pnictides. I therefore consider three classes of models: a two-band continuum model with one electron and hole band each; a two-band tight-binding model with one electron and hole band each; and a more realistic four-band model with two electron bands and two hole bands each. In the continuum model I analyze the conditions for the formation of the impurity resonance state and determine how the impurity state depends on the structure of

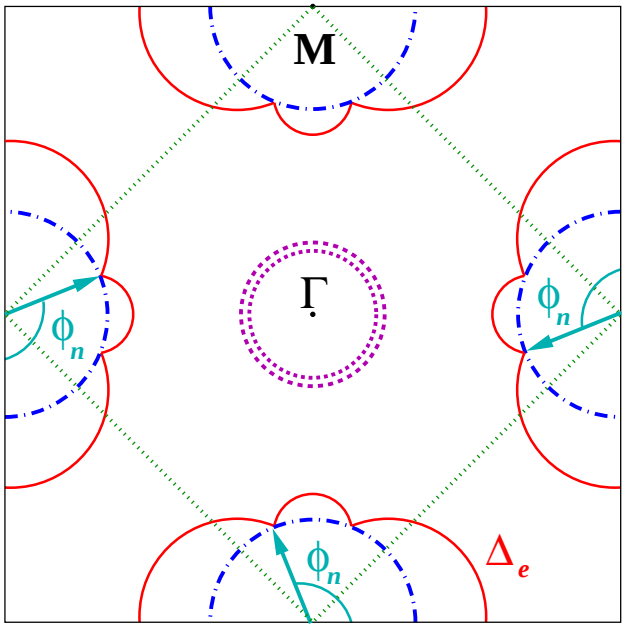

Figure 7.1: Two-dimensional model of the iron-based superconductors. The unfolded and the folded Brillouin Zones contain one and two iron atoms respectively and are indicated by the solid and dotted black lines respectively. The two hole-like (dotted magenta) and electron-like (dash-dotted blue) Fermi surfaces are of approximately the same size. The gap is taken to be isotropic on the hole Fermi surfaces, and anisotropic on the electron Fermi surfaces, shown in red solid line for the case with nodes at ϕ_n and equivalent points.

the bands. I then use a simple two-band nearest-neighbor tight-binding model to verify that my analytical results are clearly manifested in the numerical approaches and to understand the properties of the impurity state in real space. This then sets the stage for carrying out calculations in the more physical four-band model suggested in Ref. [74] where I discuss conditions for the existence of the resonance states and determine the properties of the impurity state in a realistic system.

7.1 Basic Hamiltonian and the Choice of Gap Functions

My basic Hamiltonian is $H = H_0 + H_{imp}$ where H_0 is the mean field Hamiltonian for a pure multiband superconductor and H_{imp} describes scattering by the impurities. I assume

H_0 to be diagonal in the band index, j, so that $H_0 = \sum_j H_j$, where

$$H_j = \sum_{\mathbf{k}\sigma} \xi_{j\mathbf{k}} c^\dagger_{j\mathbf{k}\sigma} c_{j\mathbf{k}\sigma} - \sum_{\mathbf{k}} \left(\Delta_{j\mathbf{k}} c^\dagger_{j\mathbf{k}\uparrow} c^\dagger_{j-\mathbf{k}\downarrow} + \Delta^*_{j\mathbf{k}} c_{j-\mathbf{k}\downarrow} c_{j\mathbf{k}\uparrow} \right) . \tag{7.1}$$

Here $\xi_{j\mathbf{k}}$ is the quasiparticle energy in band j, measured with respect to the chemical potential, which varies between different models and is specified in the appropriate sections below, $c^\dagger_{j\mathbf{k}\sigma}$ and $c_{j\mathbf{k}\sigma}$ are the creation and annihilation operators for quasiparticles with momentum $\mathbf{k}$ and the spin σ, and $\Delta_{j\mathbf{k}}$ is the superconducting gap function on the j-th Fermi surface sheet.

Hereafter I take the order parameter to be of the extended s-wave form [8, 93, 77, 84], $A + B\left[\cos(k_x a) + \cos(k_y a)\right]$, where a is the lattice constant for the square Fe lattice so that $\mathbf{k}$ is the wave vector in the "unfolded" zone scheme. When projected on the hole, S_h, and electron, S_e, Fermi surface sheets in Fig. 7.1, this results in a nearly isotropic gap on the hole sheet(s), $\Delta_{h\mathbf{k}} \approx \Delta_h$ for $\mathbf{k} \in S_h$, and a generally anisotropic gap on the electron sheet(s). To find the gap on the electron FS, I expand the gap near $(\pi, 0)$ to find $\Delta_{e\mathbf{k}} \approx A + \frac{Bk_F^2}{2} \cos 2\phi$, where ϕ is the angle as measured from the [010] direction. A similar expansion near the other M points gives the same gap shape on all of the other electron sheets. Thus, the gap is of the general form $\Delta_{e\mathbf{k}} = \pm\Delta_e(1 + r\cos 2\phi)$ for $\mathbf{k} \in S_e$, where the angle ϕ is measured from the [100] and [010] directions at $(\pm\pi, 0)$ and $(0, \pm\pi)$, respectively, as I show in Fig. 7.1. Different gap structures are then determined by the relative sign of the gaps on the electron and the hole sheets (s_{++} vs s_{+-} pairing) and the value of the parameter r. Without loss of generality, I take $r \geq 0$, and the choice of the minus sign with $r = 0$ gives the so-called s_{+-} state [8]. Gap anisotropy on the electron sheet increases with increasing r, with the quasiparticle spectrum fully gapped for $0 < r < 1$, and the minimal/maximal gap values $\Delta_{e,\pm} = \pm\Delta_e(1 \pm r)$. Nodes develop in $\Delta_{e\mathbf{k}}$ for $r > 1$ at $\phi_n = \pm\left(\pi \pm \arccos r^{-1}\right)/2$, see Fig. 7.1, and move towards the 45° degree directions as r increases. In the limit $r \to \infty$, the gap on the electron sheets approaches the d-wave form $\Delta_{e\mathbf{k}} = -r\Delta_e \cos 2\phi$. Throughout this paper I will be considering

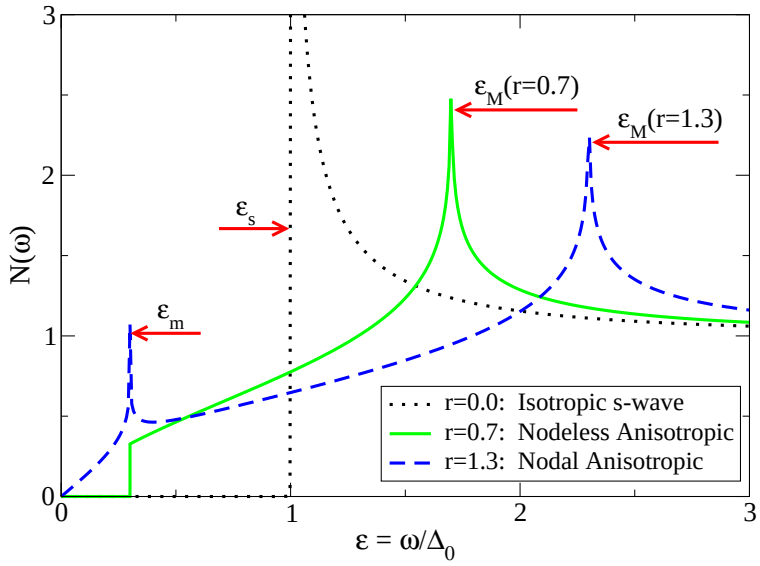

Figure 7.2: Density of states for single-band superconductor with with order parameter $\Delta_{\mathbf{k}}=-\Delta_0(1+r\cos 2\phi)$ and $\varepsilon=\omega/\Delta_0$. I show the isotropic s-wave gap (r=0), gap with deep minima (r=0.7), and gap with nodes (r=1.3). Arrows indicate the s-wave gap edge ε_s=1, the lower gap feature at $\varepsilon_m=|1-r|$=0.3, and the upper gap edges at $\varepsilon_M=|1+r|$.

the values $r = 0$ (isotropic gap on electron Fermi surface), $r = 0.7$ (nodeless anisotropic gap), and $r = 1.3$ (nodal gap). For both of the latter two choices, a feature exists in the density of states of the pure material at the energy $\omega = 0.3\Delta_e$, see Fig. 7.2, which makes the comparison of the two more straightforward.

The relative magnitudes of the gap amplitudes on the electron and the hole Fermi surface sheets depends on the details of the pairing interaction and the band structure. For two-band superconductivity arising from purely interband pairing, since the dimensionless coupling constant is the product of the bare coupling and the density of states, a simple calculation of the gap amplitude ratio $\delta_0 = \Delta_e/\Delta_h$ at zero temperature yields (see Appendix D)

$$1 = n\langle\delta^2\rangle_{FS} = n\delta_0^2\left(1+\frac{r^2}{2}\right), \tag{7.2}$$

where $n = N_e/N_h$ is the ratio of the DOS at the Fermi surface in the electron and hole bands respectively, and $\langle\ldots\rangle_{FS}$ denotes the Fermi-surface average. To simplify my analysis, I keep the total Fermi-level DOS fixed at $N_F = (N_e + N_h)/2$. For r=0 Eq. (7.2) agrees with the

result for isotropic s_{+-}-wave superconductivity [89, 135]. As seen in ARPES measurement of the the band dispersion [72, 136] and quantum oscillation measurement of the various band masses [81, 137, 138, 82], the electron- and hole-band contributions to the normal state DOS vary with material and generally fall into the range $0.5 < N_e(0)/N_h(0) < 1$. Here $N_j(0)$ is the total contribution to the Fermi-level DOS from all FS sheets of the jth type. Tight-binding fits to the Fermi surface also yield different Fermi-level DOS on the two types of the FS sheets [73, 74, 75], with some estimates as large as $n \approx 5$ [73]. For all of the models examined in this paper, I consider the parameter range $0.5 < n < 1$ and hence estimate $1 < \delta_0 < \sqrt{2}$ for the isotropic s_{+-} gap. The range of δ_0 for the anisotropic cases depends of course on the choice of r.

7.2 Impurities and the T-matrix Formalism

I make a simplifying assumption that the scattering due to a single non-magnetic impurity located at the origin is independent of momentum within each band, and therefore is given by

$$H_{imp} = \sum_{\mathbf{k}\mathbf{k}'\sigma} U_{jj'} c^\dagger_{j\mathbf{k}\sigma} c_{j'\mathbf{k}'\sigma} \,, \tag{7.3}$$

where $U_{jj'}$ are the elements of the scattering matrix $\check{U}$ in the particle-hole (Gor'kov-Nambu) and band space. The approximate independence of the elements of $\check{U}$ is justified in part by the small size of the Fermi surfaces in pnictides. For simplicity hereafter, I parameterize the impurity by the "intraband" and "interband" matrix elements, U_0 and U_1 respectively. In the two-band model this notation is obvious,

$$U_{jj'} = \begin{cases} U_0, & \text{if } j = j' \\ U_1, & \text{if } j \neq j' \,, \end{cases} \tag{7.4}$$

as shown Fig. 7.3(a). In the four-band model this nomenclature means that the scattering both within each electron or hole band, and between the nearly degenerate electron or hole bands, is described by U_0, while the matrix element for scattering between any electron-

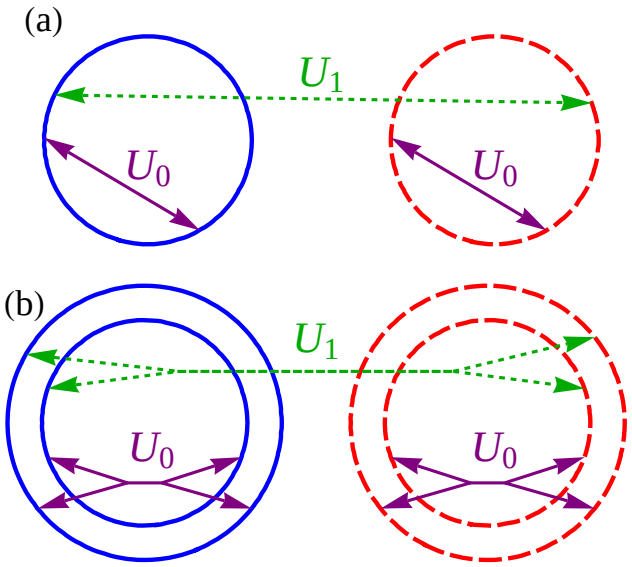

Figure 7.3: Quasiparticles near the electron (solid circles) and hole (dashed circles) FS sheets scatter within and between the conduction bands by means of the intraband (U_0: solid arrows) and interband (U_1: dashed arrows) components of the scattering potential. Panels (a) and (b) show, respectively, the scattering potentials for the two- and four-band models for the iron-based superconductors.

like band and any hole-like band is given by U_1. I show the four-band scattering potential schematically in Fig. 7.3(b).

The electron and hole Fermi surfaces in the iron-based superconductors are separated by a wave vector of order π/a, and therefore this parametrization means separation into small and large momentum scattering. The potential of a generic charged impurity is screened at the Thomas-Fermi length, which is on the order of the lattice spacing, a. Consequently, interband scattering can be expected to be suppressed, $U_1 \ll U_0$. This suggests that one limit of interest is a purely intraband scattering potential, $U_1=0$. On the other hand, band structure calculations show that the same iron d-orbitals contribute significantly to both the electron and the hole sheets of the Fermi surface [77]. Therefore it is logical to assume that an impurity, located at or near the Fe site, that directly affects these orbitals, will produce a significant interband scattering component. One obvious candidate is the Co-dopants in the 122 series where first principle calculation indicates, perhaps, a moderate

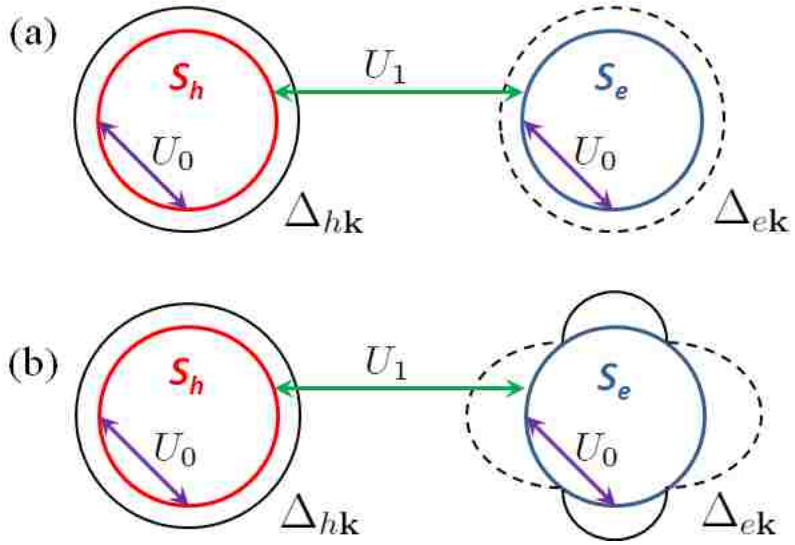

Figure 7.4: Two general scenarios for the scattering between FS sheets with different gap shapes. The solid (dashed) black lines represent a positive (negative) superconducting gap, and the impurity states are generated primarily by either U_0 or U_1 in each of the two cases shown. In panel (a), impurity states are generated when U_1 scatters quasiparticles across the sign change of the gap on different FS sheets. In panel (b), impurity states are generated when U_0 scatters quasiparticles across the gap nodes on the electron FS sheet.

ratio of $U_1/U_0 \sim 1/3$ [139]. Fits to the low-temperature specific heat in Co-doped 122 materials suggest $U_1/U_0 \sim 0.6$ [140, 141]. In this study, I consider both these ratios and also the "extreme" case $U_1 \simeq U_0$. In a realistic material the scattering may have additional anisotropy due to the orbital content that varies along each Fermi surface, but I am not aware of any detailed microscopic calculations of this effect. Furthermore, the inclusion of too many phenomenological parameters obscures the essential physics I aim to explain, hence I limit my analysis to the parameters U_0 and U_1.

Both scattering potential components help to generate the impurity states, but the formation of the states are controlled by either U_0 or U_1 depending on the shape of the gap on the electron FS sheets. In Fig. 7.4, I shown the two general scenarios for forming the resonant state. In the situation where the gaps are of the isotropic s_{+-} type, impurity states are generated primarily when U_1 scatters quasiparticles across the sign change of the gap on different FS sheets. In contrast, when there are gap nodes on the electron FS sheets, the

impurity states are controlled by U_0 which scatters quasiparticles across the nodes on the electron sheet.

To compute the physical properties, I determine the Green's function which is a matrix in both band and particle-hole space,

$$\check{G}_{jj'}(\mathbf{k},\mathbf{k}';\tau) = -\left\langle T_\tau \left(\Psi^\dagger_{j\mathbf{k}}(\tau)\Psi_{j'\mathbf{k}'} \right) \right\rangle , \tag{7.5}$$

where $\Psi^\dagger_{j\mathbf{k}}=(c^\dagger_{j\mathbf{k}\uparrow}, c_{j-\mathbf{k}\downarrow})$ is the Nambu spinor for band j, and T_τ is the ordering operator for the imaginary time τ. In this notation $\widehat{H}_{j\mathbf{k}}=\xi_{j\mathbf{k}}\widehat{\tau}_3 + \Delta_{j\mathbf{k}}\widehat{\tau}_1$, with $\widehat{\tau}_0$ the identity matrix and $\widehat{\tau}_i$ (i=1...3) the Pauli matrices in the Nambu space. In the absence of impurities, $\check{G}_{0,jj'}(\mathbf{k},\mathbf{k}')=\delta_{jj'}\delta_{\mathbf{k}\mathbf{k}'}\widehat{G}_{0,j}(\mathbf{k})$, and, after transforming to the fermionic Matsubara frequencies $\omega_n = 2\pi T(n+1/2)$ at temperature T, the Green's function $\widehat{G}_{0,j}(\mathbf{k};i\omega_n)=(i\omega_n\widehat{\tau}_0 - \widehat{H}_{j\mathbf{k}})^{-1}$ in each band takes the standard form

$$\widehat{G}_{0,j}(\mathbf{k};i\omega_n) = -\frac{i\omega_n\widehat{\tau}_0 + \xi_{j\mathbf{k}}\widehat{\tau}_3 + \Delta_{j\mathbf{k}}\widehat{\tau}_1}{\omega_n^2 + \xi^2_{j\mathbf{k}} + \Delta^2_{j\mathbf{k}}} . \tag{7.6}$$

In the particle-hole space, the non-magnetic charged impurity potential is proportional to the Pauli matrix τ_3. I solve the single impurity problem by computing the T-matrix, $\check{T}_{jj'}(\mathbf{k},\mathbf{k}';i\omega_n)$ that accounts for all the scattering events. The Green's function and the T-matrix satisfy the equations [125]

$$\check{G} = \check{G}_0 + \check{G}_0\check{T}\check{G}_0 , \tag{7.7}$$

$$\check{T} = \check{U} + \check{U}\sum_{\mathbf{k}} \check{G}_0\check{T} . \tag{7.8}$$

For my choice of the momentum-independent $\check{U}$, the T-matrix is solely a function of the band index and the frequency, hence

$$\check{T} = \left[1 - \check{U}\sum_{\mathbf{k}} \check{G}_0 \right]^{-1} \check{U} . \tag{7.9}$$

While this form is convenient for the analysis in momentum space and for analytical work, to compute the local density of states (LDOS) I need to Fourier transform the equations to

real space and carry out the analytic continuation $i\omega_n \to \omega + i0^+$ to obtain the retarded propagator. The corresponding equations for an impurity located at the origin read

$$\check{G}(\mathbf{r},\mathbf{r}';\omega) = \check{G}_0(\mathbf{r},\mathbf{r}';\omega) + \check{G}_0(\mathbf{r},0;\omega)\check{T}(\omega)\check{G}_0(0,\mathbf{r}';\omega)\,, \tag{7.10}$$

with

$$\check{T}(\omega) = \left[1 - \check{U}\check{G}_0(0,0;\omega)\right]^{-1}\check{U}\,. \tag{7.11}$$

The poles of the Green's function in the ω plane give the energies of the elementary excitations. It is clear from the structure of Eq. (7.7) and Eq. (7.10) that the set of the poles of $\check{G}$ consists of the poles of $\check{G}_0$, which yield the excitation energies in the clean system, and the poles of the T-matrix. Consequently, it is the poles of the T-matrix that give the energies of the impurity-induced states. The density of states per spin in each band is

$$N_j(\mathbf{r},\omega) = -\frac{1}{\pi}\mathrm{Im}\left(\check{G}_{jj,11}(\mathbf{r},\mathbf{r};\omega + i\,0^+)\right)\,, \tag{7.12}$$

where the indices 11 refer to the particle component in the Nambu space. I use this equation to determine the density of states near the impurity site. It is important that this expression is diagonal in the band indices since it means that only the diagonal components of the T-matrix, $\check{T}_{jj}$, are important for the determination of the impurity states, see Eq. (7.7).

Several important comments are in order here. First, I assume that the electron and hole Fermi surfaces are well separated, which is certainly true for the pnictides, so that the summation over the momenta $\mathbf{k}$ in Eq. (7.8) is dominated by the region near each respective sheet. Second, since each such summation generally yields a prefactor of the density of states at the Fermi surface, the ratio of the densities of states for the electron and the hole Fermi sheets controls not only the relative gap amplitudes (as discussed above), but also the number of states available for scattering, and directly affects the location of the resonance. I include it below in the analytical work and show that the effect is very significant. Therefore in choosing a parametrization of the Fermi surface for numerical approaches it is important

to fit not only the topology of the Fermi surface, but also the density of states, i.e. the slope of each band near the chemical potential. I give an example below where different parameterizations of the bands yield dramatically different results for the impurity-induced state because of this effect.

Third, if I denote (as I do hereafter) $\widehat{g}_j = \sum_{\mathbf{k}} \widehat{G}_{0,j}(\mathbf{k}) = \sum_i g_{ji}\widehat{\tau}_i$, with $i = 0, \ldots, 3$, it is clear from Eq. (7.9) that the impurity potential appears in combination with

$$g_{j3} = -\sum_{\mathbf{k}} \frac{\xi_{j\mathbf{k}}}{\omega_n^2 + \xi_{j\mathbf{k}}^2 + \Delta_{j\mathbf{k}}^2} \,. \tag{7.13}$$

This component of the local Green's function depends on the particle-hole band asymmetry, and therefore changes little between the normal and the superconducting states (I assume that the gap amplitude is small compared to the bandwidth), and therefore can be evaluated in the normal state. Analytical work often assumes $g_{j3} = 0$. For a flat band of width W with the density of states $N_0 = W^{-1}$ and the chemical potential μ measured from the center of the band, I find $g_3 = -W^{-1} \ln|(W - 2\mu)/(W + 2\mu)|$. Hence $g_3 W \sim \mu/W \ll 1$ for $\mu \ll W$ and becomes of order unity when the chemical potential approaches the band edges. Of course, in numerical work the value of $g_{j3} \neq 0$ depends on the chemical potential and the assumed band structure; this is especially true of the tight-binding models where a van Hove singularity typically is present. It is well known from the studies of single-band superconductors that, for such models and for a given scattering potential strength, the resonance state is sensitive to the exact form of the band structure [142, 143], and therefore below I explicitly address how the particle-hole anisotropy affects the results. Note that my simple analysis above suggests that $g_{e3}/N_e(0) \leq 0$ for the electron-like bands and $g_{h3}/N_h(0) \geq 0$ for the hole-like bands . This implies that the sign of the scattering potential (repulsive for holes and attractive for electrons, or vice versa), while irrelevant in the particle-hole symmetric case, does matter for a realistic band structure. I measure the Green's functions g_{j3} in terms of the πN_j for the rest of this study.

Finally, I comment on the analytic structure of the T-matrix. The density of states, $N_j(\mathbf{r}, \omega)$, is related to the retarded Green's function, which is analytic in the upper half of the complex energy plane; therefore, all the poles of the T-matrix are in the lower half-plane. Consequently, in solving Eq. (7.8) and Eq. (7.11), care needs to be taken to use the appropriate analytic continuation of the Green's function that coincides with the retarded $\check{G}_0$ in the upper half-plane, but does not have a branch cut on crossing into the lower half-plane. I present a detailed procedure for constructing such a function in Appendix E.

8. Two-band Model in a Continuum

8.1 Analytical Model and the T-matrix

A model with two circular Fermi surface sheets, which I refer to as the "electron" (band index $j = e$) and the "hole" ($j = h$), even though I control by hand the particle-hole anisotropy in each, allows analytical progress and clear elucidation of the effects I aim to investigate. The T-matrix, Eq. (7.8), is a 2x2 matrix in the band index, see also Refs. [144, 115]. Fig. 8.1 shows the diagrammatic representation for the intra- and interband components for the electron band, and gives

$$\widehat{T}_{ee} = U_0\widehat{\tau}_3 + U_0\widehat{\tau}_3\widehat{g}_e\widehat{T}_{ee} + U_1\widehat{\tau}_3\widehat{g}_h\widehat{T}_{he}\,, \tag{8.1a}$$

$$\widehat{T}_{he} = U_1\widehat{\tau}_3 + U_1\widehat{\tau}_3\widehat{g}_e\widehat{T}_{ee} + U_0\widehat{\tau}_3\widehat{g}_h\widehat{T}_{he}\,. \tag{8.1b}$$

Here I suppressed the frequency ω for brevity. The equations for $\widehat{T}_{hh}$ and $\widehat{T}_{he}$ are obtained by simply switching the band labels. I find

$$\widehat{T}_{ee} = \widehat{A}^{-1}\left[U_0\widehat{\tau}_3 - (U_0^2 - U_1^2)\widehat{\tau}_3\widehat{g}_h\widehat{\tau}_3\right]\,, \tag{8.2}$$

where

$$\widehat{A} = (1 - U_0\widehat{\tau}_3\widehat{g}_h)\,(1 - U_0\widehat{\tau}_3\widehat{g}_e) - U_1^2\widehat{\tau}_3\widehat{g}_h\widehat{\tau}_3\widehat{g}_e\,. \tag{8.3}$$

It follows from Eq. (8.3) that the poles of the T-matrix are given by the solutions of $\det(\widehat{A}) \equiv D(\omega) = 0$, where

$$\begin{aligned} D(\omega) = U_0^4 &\left(g_{e0}^2 - g_{e1}^2 - \pi^2 N_e^2 c_e^2 - \overline{g_e}^2\frac{U_1^2}{U_0^2}\right) \\ &\times \left(g_{h0}^2 - g_{h1}^2 - \pi^2 N_h^2 c_h^2 - \overline{g_h}^2\frac{U_1^2}{U_0^2}\right) \\ &- U_1^2\left(\overline{g_e}^2 + \overline{g_h}^2 + 2(g_{e0}g_{h0} - g_{e1}g_{h1} + g_{e3}g_{h3})\right)\,, \end{aligned} \tag{8.4}$$

where $\overline{g_j}^2 = \sum_i (-1)^i g_{ji}^2$ and $c_j^2 = (\pi N_j U_0)^{-2}\,(1 - U_0 g_{j3})^2$.

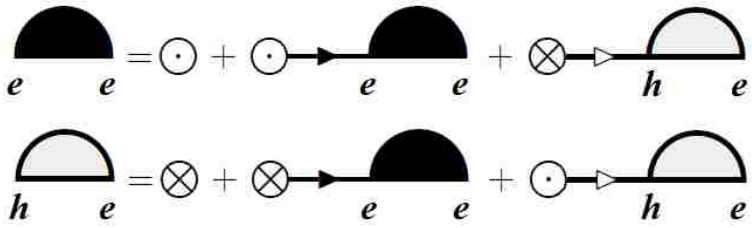

Figure 8.1: Diagrammatic equations for the electron-band T-matrix in the two-band model. Solid (shaded) semicircle is $\widehat{T}_{ee}$ ($\widehat{T}_{he}$); Line with filled (hollow) arrowhead is the propagator $\widehat{g}_e$ ($\widehat{g}_h$). Dotted (crossed) circle is the intraband, U_0, (interband, U_1) scattering potential which contains the Pauli matrix $\widehat{\tau}_3$.

I compute the τ_0 and τ_1 components of the local Green's functions $\widehat{g}_j$ by going to the continuum representation and using, for the circular Fermi surface,

$$\sum_k \widehat{G}(\mathbf{k};\omega) \approx N_j \int_{-\omega_c}^{\omega_c} d\xi_j \int_0^{2\pi} \frac{d\phi_j}{2\pi} \widehat{G}(\xi_j,\phi_j;\omega)\,, \tag{8.5}$$

where ϕ_j is the angle parameterizing the jth Fermi surface sheet and ω_c is the energy cutoff. I use the amplitude of the isotropic gap on the hole Fermi surface as the energy unit, $\varepsilon{=}\omega/\Delta_h$, so that (recall $\delta_0{=}\Delta_e/\Delta_h$)

$$\widehat{g}_h(\varepsilon) = -\pi N_h \frac{\varepsilon\widehat{\tau}_0 + \widehat{\tau}_1}{\sqrt{1-\varepsilon^2}} + g_{h3}\widehat{\tau}_3\,, \tag{8.6}$$

$$\widehat{g}_e(\varepsilon) = -\pi N_e \left\langle \frac{\varepsilon\widehat{\tau}_0 - \delta_0(1+r\cos(2\phi))\widehat{\tau}_1}{\sqrt{\delta_0^2(1+r\cos(2\phi))^2-\varepsilon^2}} \right\rangle_{FS} + g_{e3}\widehat{\tau}_3\,, \tag{8.7}$$

where $\langle ... \rangle_{FS}$ indicates the angular integration over the Fermi surface. Since g_{j3} depends on the details of the normal state band structure, see Eq. (7.13), I keep it as a free parameter with no energy dependence. The appropriate definition of the branches of the square root used in Eq (8.6) is given in Appendix E. I found closed form expressions for g_{ji} and arbitrary values of r: The derivation is given in Appendix E.2, and the resulting expressions are straightforward but too cumbersome to write here. For a pole at $\varepsilon = \varepsilon_1 - i\varepsilon_2$, both the DOS in the pure system at the same energy, ε_1, and the width of the resonance, $\varepsilon_2 = (2\tau)^{-1}$, where τ is the lifetime, determine how the impurity state mixes with the continuum and whether it is observable experimentally. I will see below that low-energy states near impurities in

multiband systems exist only under special conditions. I will determine the most favorable conditions for the existence of such resonances by solving $\partial D(\omega)/\partial U_1 = 0$ for the optimal scattering strength $U_{1,m}$, defined via

$$\frac{U_{1,m}^4}{U_0^4} = \frac{g_{e0}^2 - g_{e1}^2 - \pi^2 N_e^2 c_e^2}{g_{e0}^2 - g_{e1}^2 - g_{e3}^2} \frac{g_{h0}^2 - g_{h1}^2 - \pi^2 N_h^2 c_h^2}{g_{h0}^2 - g_{h1}^2 - g_{h3}^2} \,. \tag{8.8}$$

Solving this equation and $D(\omega) = 0$ gives the extremal impurity state energy, and I check that this energy is generally a minimum for the s_{+-} gap symmetry. I now proceed to consider several conceptually important cases.

8.2 Decoupled Bands

In the absence of interband scattering, $U_1 = 0$, the problem reduces to that for two decoupled single band superconductors. This limit allows me to make a connection with previous results, and show the technical details of the calculation. Eq. (8.4) factorizes in the equations for each band,

$$(U_0^{-1} - g_{j3})^2 - \left[g_{j0}^2 - g_{j1}^2\right] = 0 \,. \tag{8.9}$$

It is clear that the effect of the particle-hole anisotropy is equivalent to changing the *effective* strength of the impurity potential [142], $U_{eff}^{-1} = U_0^{-1} - g_{j3}$, so that the strong scattering (unitarity) limit, $U_{eff}^{-1} \to 0$ no longer corresponds to a large value of the bare scattering potential U_0 as it did for $g_3 = 0$. The solutions of Eq. (8.9) are well known for the s- and d-wave cases [125]. For an isotropic SC gap, $\Delta_{\mathbf{k}} = \Delta_0$, Eq. (8.6) gives $g_{j0}^2 - g_{j1}^2 = -\pi^2 N_j^2$. Hence Eq. (8.9) is never satisfied and there are no impurity bound states. For $r \gg 1$, when the gap approaches the d-wave shape with the magnitude $\Delta_{max} = r\Delta_0$, I expand the local Green's function $\bar{\varepsilon}{=}\varepsilon/r{=}\omega/\Delta_{max} \ll 1$. Using Eqs. (E.12) and (E.14) from Appendix E.2.1, I find

$$c_e^2 + \frac{4}{\pi^2 r^2} = \frac{4\bar{\varepsilon}^2}{\pi^2} \left[\ln^2\left(\frac{4}{\bar{\varepsilon}}\right) + i\pi \,\mathrm{sgn}(\bar{\varepsilon}) \ln\left(\frac{4}{\bar{\varepsilon}}\right)\right] , \tag{8.10}$$

where $c_e = (\pi N_F U_{eff})^{-1} \equiv \cot\delta$, and δ is the scattering phase shift. In the limit r^{-1}=0, the average of the order parameter over the Fermi surface vanishes, $\langle\Delta_{\mathbf{k}}\rangle_{FS} = 0$, so that $g_1 = 0$, and I recover the well-known resonance condition for d-wave SC [127, 130, 125],

$$\bar{\varepsilon}_d = \frac{\pi|c_e|}{2\ln(8/\pi|c_e|)}\left(\pm 1 - i\frac{\pi}{2\ln(8/\pi|c_e|)}\right). \tag{8.11}$$

This yields a mid-gap state, $\bar{\varepsilon}_d = 0$, in the unitarity limit, $\delta = \pi/2$, when $U_{eff}^{-1} = 0$. When $0 < r^{-1} \ll 1$, the low-energy solutions are given by Eq. (8.11) with $|c_e| = \sqrt{4/\pi^2 r^2 + c_e^2}$. It follows that the resonance for a given scattering strength moves away from $\omega = 0$ as the gap average over the Fermi surface increases.

For a given gap shape, r, the lowest-energy resonant state always forms in the unitarity limit $U_{eff}^{-1} = 0$, even when the expansion in r^{-1} is no longer valid. I find these resonances by using the Green's functions in Appendix E.2 to solve Eq. (8.9) numerically with $c_e = 0$. Fig. 8.2, shows the evolution of the deep-lying impurity state with the gap anisotropy r. For the nodal case, $r > 1$, the T-matrix generically has two poles on the positive frequency side, at $\varepsilon_1 > r - 1$ and at $\varepsilon_1 < r - 1$, but only the latter is a sharp resonance plotted in Fig. 8.2. Decreasing the anisotropy in a system with gap nodes causes the impurity state to broaden and move away from the chemical potential, see Fig. 8.2. As $r \to 1$, the unitarity impurity state approaches $\varepsilon_m = |1 - r|$, and moves above the gap edge when $r \lesssim 1$, fully merging with the continuum.

8.3 Fully-isotropic Gaps: The s_{+-} and s_{++} States

When the bands are coupled, it is clear from Eq. (8.4) that the sign of the interband scattering, U_1, is irrelevant, and only its magnitude affects the location of the poles of the T-matrix. In contrast, both the magnitude and the sign of the intraband scattering component, U_0, are relevant. In the following I consider the simplest of the cases proposed for the iron-based superconductors, that with the isotropic gaps on both Fermi surface sheets, $\Delta_{h\mathbf{k}} = \Delta_h$

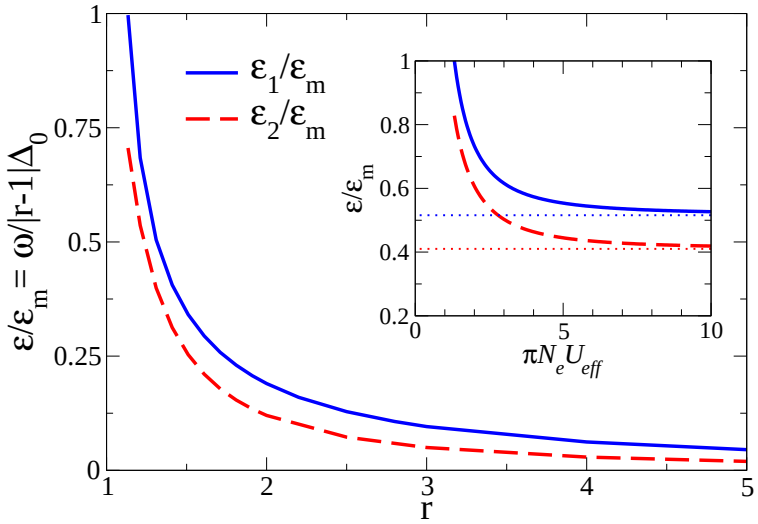

Figure 8.2: (Evolution of the impurity resonance for a single band. I plot the energy (ε_1) and the width (ε_2) of the resonance normalized to the smaller gap edge, $\Delta_m = |r-1|\Delta_e$. Main panel: unitarity limit, $U_{eff}^{-1} = 0$. The resonance state tends to mid-gap only in the d-wave limit, $r^{-1} = 0$. Inset: finite $r = 1.3$. Even for strong scattering the resonance remains at finite energy.

and $\Delta_{e\mathbf{k}} = -\Delta_e$ (where $\Delta_e > 0$ for s_{+-} pairing, and $\Delta_e < 0$ for the s_{++} state). It is easy to verify that $g_{j0}^2 - g_{j1}^2 = -\pi^2 N_j^2$, with no energy dependence, which simplifies the analysis greatly. My general approach here is to find the most favorable conditions for the existence of the low-energy impurity state, ask whether they can be satisfied for the Fe-containing materials, and determine how far from these optimal conditions I can be in the parameter space to still see the resonance peak.

8.3.1 Locating the Bound State Energy

For the isotropic gap, all of the energy dependence of Eq. (8.4) is contained in the term $\alpha = g_{e0}g_{h0} - g_{e1}g_{h1}$. Thus the poles of the T-matrix can be found explicitly. The bound state energy satisfies

$$\frac{\omega^2 + \Delta_e\Delta_h}{\sqrt{\Delta_e^2 - \omega^2}\sqrt{\Delta_h^2 - \omega^2}} = \alpha(U_i, N_j, g_{j3})\,, \tag{8.12}$$

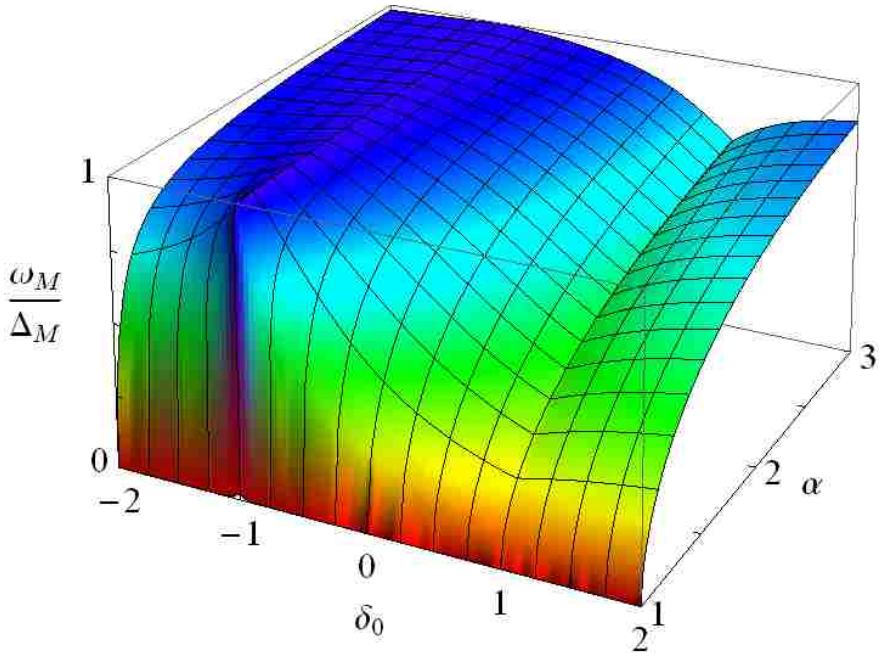

Figure 8.3: Energy of the impurity bound state for isotropically-gapped system given by $\omega_{\rm M} = \min(\omega_+, \omega_-)$, see Eq. (8.14), which is measured with respect to $\Delta_{\rm M} = \min(\Delta_e, \Delta_h)$. For a given value of the DOS ratio N_e/N_h, and the corresponding fixed δ_0, variation of the impurity potentials U_0 and U_1 traces a path along the surface. For a given value of α, the bound state energy is always lowest at δ_0=1.

where $\alpha \geq 1$ and is given by

$$\begin{aligned}\alpha =& \frac{\pi^2 N_e N_h U_0^4}{2U_1^2}\left[1 + c_e^2 - \left(1 + \frac{g_{e3}^2}{\pi^2 N_e^2}\right)\frac{U_1^2}{U_0^2}\right]\left[1 + c_h^2 - \left(1 + \frac{g_{h3}^2}{\pi^2 N_h^2}\right)\frac{U_1^2}{U_0^2}\right] \\ &+ \frac{\pi^2(N_e^2 + N_h^2) + (g_{e3} - g_{h3})^2}{2\pi^2 N_e N_h}\,.\end{aligned} \tag{8.13}$$

Note that the dependence of the energies on the scattering potential and the partial densities of states enters only via the parameter α. Thus, the poles of the T-matrix are

$$\omega_\pm^2 = \frac{\alpha^2(\Delta_e + \Delta_h)^2 - 2(\alpha^2 - 1)\Delta_e\Delta_h}{2(\alpha^2 - 1)} \pm \frac{\alpha(\Delta_e + \Delta_h)}{2(\alpha^2 - 1)}\sqrt{\alpha^2(\Delta_e - \Delta_h)^2 + 4\Delta_e\Delta_h}\,, \tag{8.14}$$

and the bound state is given by $\omega_{\rm M} = \min(\omega_+, \omega_-)$ and is measured with respect to the smaller of the two gaps $\Delta_{\rm M} = \min(\Delta_e, \Delta_h)$. Finally, it is easy to locate $U_{1,m}$ for the isotropically-gapped system since, in this case, the energy dependence disappears from

Eq. (8.8) which becomes

$$\frac{U_{1,m}^2}{U_0^2} = \sqrt{\frac{1+c_e^2}{1+\left(\frac{g_{e3}}{\pi N_e}\right)^2}}\sqrt{\frac{1+c_h^2}{1+\left(\frac{g_{h3}}{\pi N_h}\right)^2}}\,. \tag{8.15}$$

The resonance energy depends on the ratio of the gaps, δ_0, and parameter α as shown in Fig. 8.3. For a fixed band structure, variation of the impurity scattering strength traces a path of constant δ_0 along the surface, which I describe below for several situations. Although I consider arbitrary ratios of $U_1/|U_0|$ below, I emphasize that only those resonant states at $U_1 < |U_0|$ are physical solutions to Eq. (8.4).

8.3.2 Particle-hole Symmetric Case

For particle-hole symmetric bands I set $g_{h3} = g_{e3} = 0$ so that now

$$\alpha = \frac{[1+\pi^2 N_e^2(U_0^2-U_1^2)]\,[1+\pi^2 N_h^2(U_0^2-U_1^2)]}{2\pi^2 N_e N_h U_1^2} + \frac{N_e^2+N_h^2}{2N_e N_h}\,. \tag{8.16}$$

Focus first on the s_{+-} state corresponding to $\delta_0 > 0$ in Fig. 8.3. Examination of Eq. (8.12) shows that $\omega_{\rm M} = \omega_-$ and is monotonic in α. To find the optimal conditions for the impurity state, I minimize $\omega_-/\Delta_{\rm M}$ with respect to δ_0 for fixed α, and find that the bound state lies deepest in the gap when $\delta_0 = 1$. In this case, *i.e.*, for equal gap magnitudes $\Delta_j = \Delta_0$, the impurity states form at $\pm\varepsilon$ where

$$\varepsilon \equiv \frac{\omega_-}{\Delta_0} = \left[\frac{\alpha-1}{\alpha+1}\right]^{1/2}\,. \tag{8.17}$$

Mid-gap bound states form when α=1, and Eq. (8.16) shows that this requires two separate conditions, N_e=N_h=N_F *and* $U_{1,m}^2 = (\pi N_F)^{-2} + U_0^2$, a rare situation where the the bands are balanced and the interband scattering matrix element is stronger than its intraband counterpart. In Fig. 8.4(a), I show the dependence of the resonant energy on the scattering potentials for identical bands, $n = 1$, where it is clear that the lowest energy impurity states form near $U_{1,m}$.

For the s_{+-} gap and unequal densities of states, $N_e \neq N_h$, the mid-gap impurity state is altogether impossible, and the impurity bound state is always away from the chemical potential. The lowest energy of the bound state is found under the conditions of Eq. (8.15), $U_{1,m}^2 = U_0^2\sqrt{1+(\pi N_e U_0)^{-2}}\sqrt{1+(\pi N_h U_0)^{-2}}$, still at $U_1 > U_0$. I show this result in Fig. 8.4(b), where I used the interband pairing constraint $n\delta_0^2$=1 with $n = 0.5$. Imbalance in the DOSs restricts the impurity states to $\varepsilon \gtrsim 0.3$ for most values of the scattering potentials, and the low-energy bound states are relegated to scattering potentials near $U_0 \approx 0$ and substantial interband scattering $U_1 \approx (\pi N_F)^{-1}$. This is clearly an unphysical result and arises from the assumption of the particle-hole symmetric bands. As I show in the following section, relaxing this assumption changes the situation entirely.

Before that, let me consider the s_{++} gap, shown by $\delta_0 < 0$ in Fig. 8.3. The energies of the bound states are given by the same Eq. (8.14), but with $\Delta_e < 0$. Note that for the identical bands, $\Delta_e = -\Delta_h$ the bound state is always at the gap edge irrespective of the strength of the scattering potential, $\omega_\pm = \Delta_h$. For $|\Delta_e/\Delta_h| < 1$ the bound state is still given by ω_-, while in the opposite limit, $|\Delta_e/\Delta_h| > 1$, the in-gap state is obtained from ω_+. Existence of the in-gap bound state for the s_{++} two-band system is in agreement with the work of Golubov and Mazin, Ref. [145], who showed that only for identical bands is the transition temperature independent of the non-magnetic impurity scattering, while for non-identical bands interband non-magnetic scattering suppresses the transition temperature. Therefore, the bound state exists over a wide range of impurity potentials, albeit generally at higher energies compared with the optimal conditions for the s_{+-} order parameter. Figure 8.3 shows the overall features of the bound state in this case.

While for the s_{++} gap there is no reason to believe *a priori* that the interband pairing is dominant, the presence of a single thermodynamic transition where gaps on both the electron and the hole Fermi surfaces open simultaneously argues in favor of strong interband coupling. Therefore, I restrict myself to the situation where $\delta_0 = n^{1/2}$ as for the s_{+-} case discussed

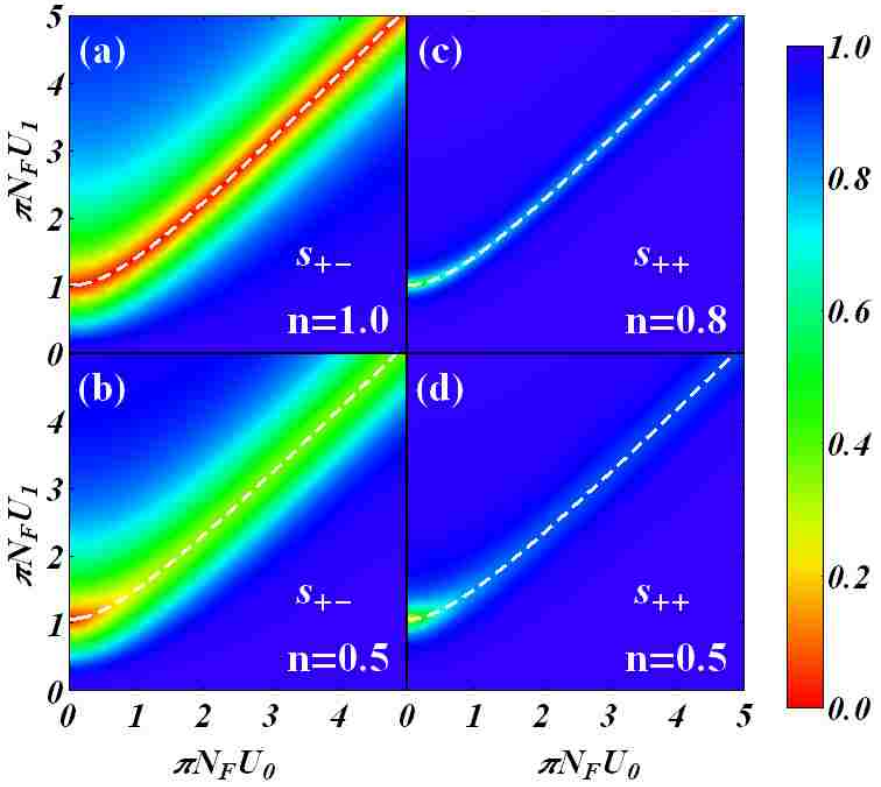

Figure 8.4: Energy of the impurity bound state in isotropically gapped systems with (a,b) s_{+-} and (c,d) s_{++} order parameter. In all cases $n\delta_0^2$=1, see Eq. (7.2), and dashed line is $\pi N_F U_{1,m}$ along which the energy is minimal, see Eq. (8.15) with the g_{j3}=0.

above. Under this restriction, the bound state generally remains close to the gap edge, a result I emphasize in Fig. 8.4(c,d). Since the bound state forms *at* the gap edge for n=1, I show instead in Fig. 8.4(c) the situation for n=0.8, *i.e.*, the case of nearly-balanced bands. As shown, the bound states form away from the gap edge only in the immediate vicinity of U_{1m} and even then remain at $\varepsilon \gtrsim 0.7$ over most of the scattering plane. Low-energy impurity states are completely absent except at the unphysical $U_0 \approx 0$ and $U_1 \approx (\pi N_F)^{-1}$. This situation does not change appreciably as the bands are further imbalanced, see Fig. 8.4(d) where $n = 1/2$, and I see that impurity states are unlikely to form in s_{++} systems. Hence, I focus my analysis below to the case of s_{+-} gap.

8.3.3 Finite Bandwidth and Particle-hole Asymmetry

When the bands are particle-hole asymmetric the impurity states are still given by Eqs. (8.14) and (8.13) with $g_{e3}, g_{h3} \neq 0$. To understand the importance of the finite g_{j3}, I focus my discussion below on energy of the bound states along this line. In fact, if I consider the states along $U_{1,m}$ and take U_0 to infinity, I find that the strong scattering state forms at $\omega = 0$ only when

$$\frac{\pi^2 N_e^2 + g_{e3}^2}{\pi N_e} = \frac{\pi^2 N_h^2 + g_{h3}^2}{\pi N_h} \,. \tag{8.18}$$

I find that a line of zero energy states always exists when the bands are completely identical, a situation I show in Fig. 8.5(a) so that $n = 1$ and $g_{e3} = -g_{h3} = 0.5$. The primary difference between this and the previous result is the shifted line $U_{1,m}$ for finite g_{j3}, since here the sign of U_0 matters. When the $g_{j3} > 0$, the minimal energy condition is now $U_{1,m} < |U_0|$ for positive U_0, and the situation is reversed if both $g_{j3} < 0$.

In Fig. 8.5(b), I show the energy for states when one band is much broader than the other. In this situation, I see that the location of the lowest-energy state depends strongly on the sign of U_0. Since the scattering in band e is effectively $\tilde{U}_0 = U_0(1 - g_{e3}U_0)^{-1}$, I see that scattering within the finite band is reduced when U_0 is moderate and of opposite sign as g_{e3}. In the strong scattering limit $|U_0| \to \infty$, the bound state energy approaches the finite value $\varepsilon = g_{e3}^2/|g_{e3}^2 + 2\pi^2 N_h^2|$.

In Fig. 8.5(c), I present the results for $g_{e3} = -g_{h3}$, *i.e.*, for bands that are identical up to the sign of their particle hole asymmetry. Since I expect electron and hole bands to have g_{j3} of opposite sign, this is the case that is most applicable to bound states in the pnictides. I find that in this case $U_{1,m} > |U_0|$, and that low-energy bound states are wholly absent at small U_0. In fact, it is straightforward to show that the energy is largest at $U_0 = 0$ for the bound states along $U_{1,m}$, and the bound state at $U_0 = 0$ approaches $\omega = 0$ only in the strong-scattering limit.

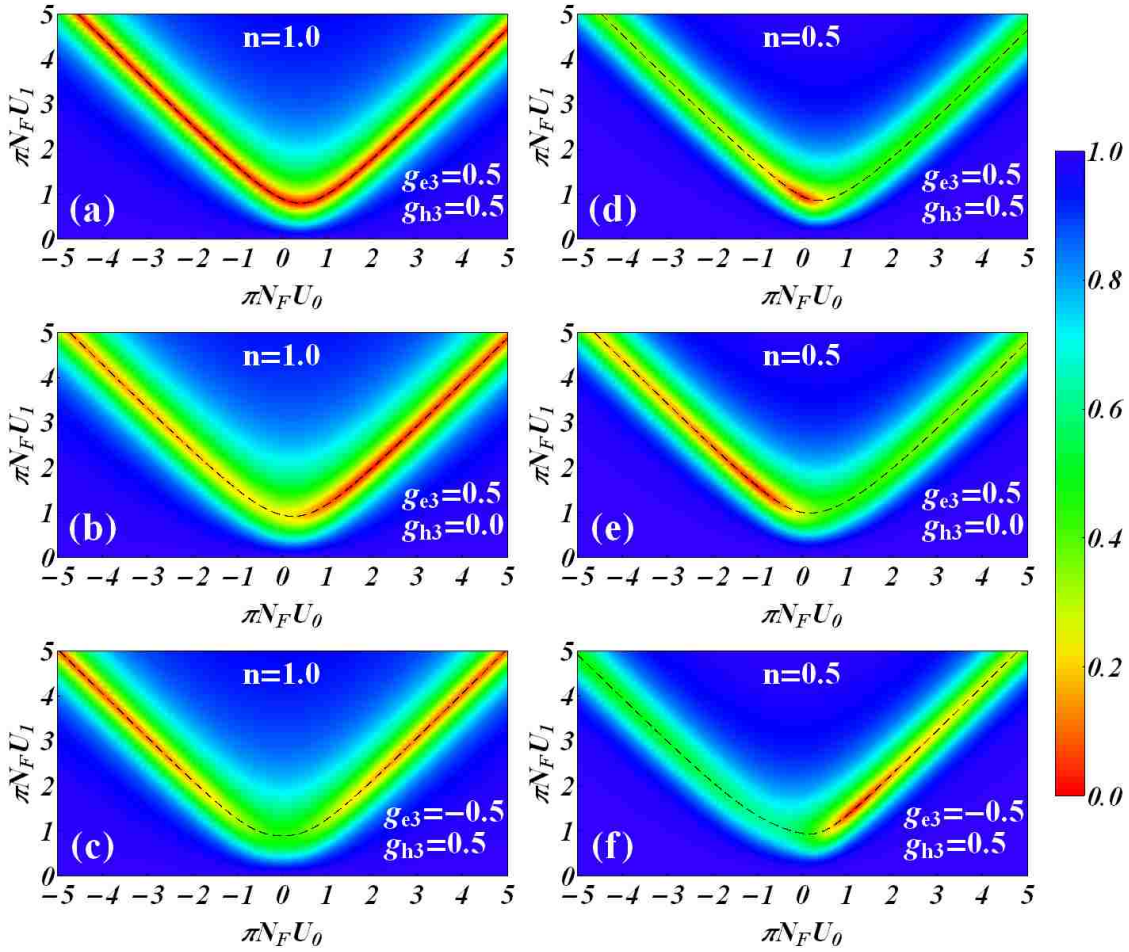

Figure 8.5: Energy of the impurity bound state in finite-bandwidth s_{+-} SC system for (a,b,c) $n = 1$ and (d,e,f) $n = 1/2$. Dashed line is $\bar{U}_{1,m}$ along which the resonance energy is minimal for a given $\bar{U}_0$, see Eq. 8.15. In all cases, $1 = n\delta_0^2$ as per Eq. (7.2).

Shifting the dominant DOS contribution to one band or the other has significant consequences for the formation of the bound state. In Fig. 8.5(d,e,f), I show the bound state energies for the same conditions as in Fig. 8.5(a,b,c), except that I now set $n = 1/2$. When the g_{j3}'s are the same, the effect of shifting the DOS balance is to simply raise the energy of all of the impurity states, as I show in Fig. 8.5(d,f). Since the system is particle hole asymmetric, the amount by which the energies are shifted depends on the sign of U_0, and for $g_{j3} > 0$ the energies are shifted much closer to the gap edge for $U_0 > 0$. When the bands have equal but opposite g_{j3}, I can capture the basic physics with an expansion of Eq. (8.13)

for $n \approx 1$. The expansion gives $\alpha(n) = \alpha(1) + 2U_0|g_{j3}|(n-1)f(n, U_0, g_{j3})$, where $f(n, U_0, g_{j3})$ is always positive. From this, I see that taking $n < 1$ shifts the energies to lower energies for $U_0 > 0$, a result that is apparent in Fig. 8.5(f).

8.4 Two Bands: Anisotropic Gap on One of the Sheets

For the anisotropically-gapped systems, I numerically solve the equation for the pole of the T-matrix given by Eq. (8.4) by evaluating the local Green's functions, see Eq. (8.7), on the electron FS with the help of Eqs. (E.6b) and (E.6c). As before, I treat the g_{j3} as free parameters. Since I expect the g_{j3} to have opposite signs for one electron and hole bands, the situation relevant for the pnictides, below I focus on the situation where $g_{h3} = -g_{e3} = 0.5$ for both balanced and unbalanced bands. I set $\delta_0^{-2}{=}n(1 + r^2/2)$ according to Eq. (7.2), whence the lower gap edge is $\varepsilon_m{=}|1 - r|\delta_0$. Below, I consider only the sub-ε_m states, impurity states that form below ε_m, since it is their spatial dependence that gives information about the nodal structure of the SC gaps. I will return to this point in Sections 9 and 10 where I calculate the spatial dependence of the local density of states near the single non-magnetic impurity.

8.4.1 Nodeless Anisotropic Gap

As I show in Fig. 8.6, the low-energy states in the $\delta_0 = 1$ system form only over a very narrow region of the U_0-U_1 plane in the vicinity of $U_{1,m}$. Since the electron band is fully-gapped at low energies so that $g_{e0}^2 - g_{e1}^2 \approx -\pi^2 N_e^2$, and, far below ε_m, here I can approximate $U_{1,m}$ by the isotropic s_{+-} result from Eq. (8.15). Compare the energies in Figs. 8.6(a) and (b) and those in the immediate vicinity of $U_{1,m}$ for isotropic s_{+-} that I show in Figs. 8.5(c) and 8.5(f), respectively. As shown, there are few qualitative differences in the bound state energies as long as the gap remains nodeless. This includes the fact that the low-energy states do not form below $U_1 \approx |U_0|$ and are thus unlikely to form in the nodeless anisotropic

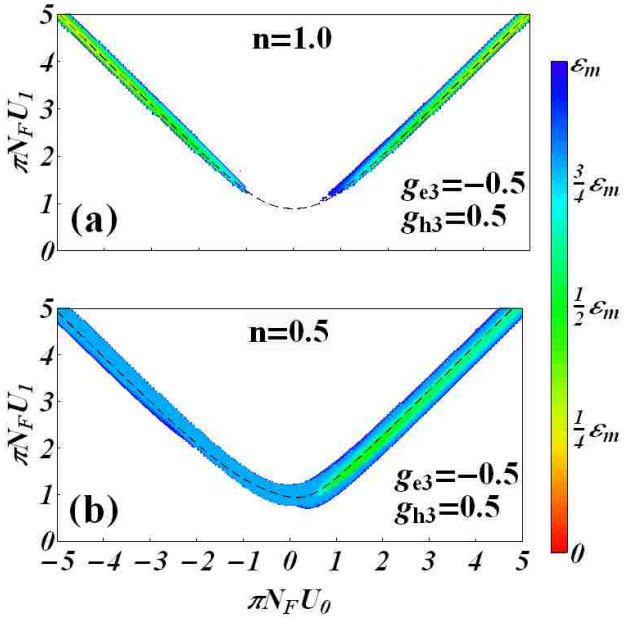

Figure 8.6: Energy of the low-lying impurity state in finite-bandwidth, nodeless anisotropic system, r=0.7, with (a) n=1 and (b) n=1/2. The T-matrix has no poles below ε_m in white regions, and only the poles at $U_1 < |U_0|$ are physical resonant states. Hence, low-energy states are not likely to form in the absence of gap nodes. Dashed line is $\bar{U}_{1,m}$ along which the resonance energy is minimal, see Eq. 8.15. In both cases, δ_0^{-2}=$n(1 + r^2/2)$ and $\varepsilon_m = 0.3\delta_0$. Energy is measured relative to ε_m.

system. I do not show the results for $\delta_0 < 0$. I did check, however, for low-energy resonant states for the nodeless anisotropic system with $\delta_0 < 0$. I found that the impurity state does not form below ε_m.

8.4.2 Anisotropic Gap with Nodes

The situation changes drastically when the FS supports gap nodes. Recall that the formation of the resonant state requires that quasiparticles be scattered between parts of the FS that have gaps of different sign. If nodes are present on one of the sheets, then the intraband component U_0 controls the formation of the impurity state, as I explained in Section 7.2. Consequently, once U_0 is sufficiently large, I find that the low-energy state forms at even the smallest values of U_1. This is in keeping with the single-band results that

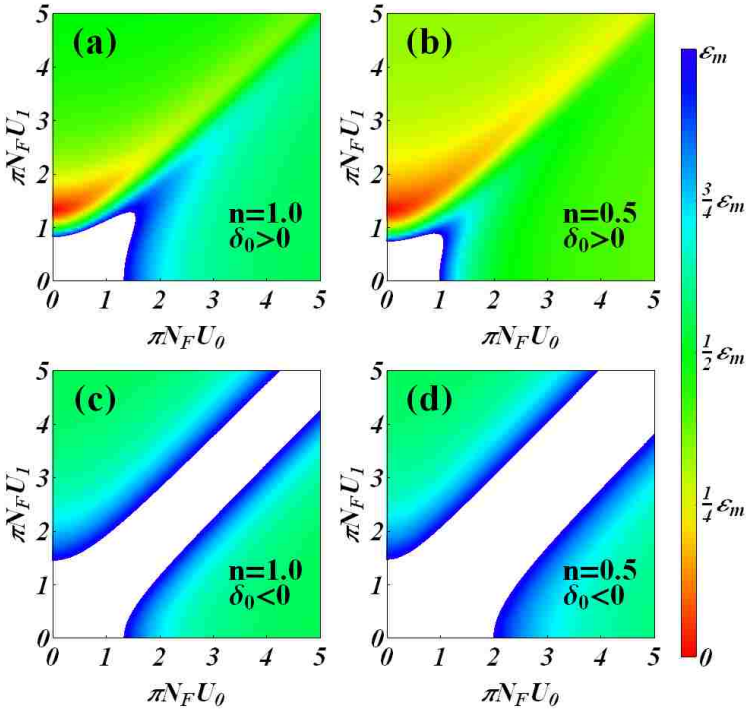

Figure 8.7: Energy of the impurity bound state in systems with nodal gap for (a,b) $\delta_0 > 0$ and (c,d) $\delta_0 < 0$. In all cases the g_{j3}=0, and δ_0 is set according to Eq. (7.2). Energy is measured relative to ε_m.

I discussed in Section 8.4.2. Since it is U_0 that is important when there are nodes on the electron FS, I find that the low-energy state forms readily for both signs of δ_0.

In Fig. 8.7, I show the low-energy state when the bands are particle-hole symmetric. For the sign-changing case $\delta_0 > 0$, the low-energy state forms at all but the smallest values of U_0 and U_1, see Figs. 8.7(a,b). The exact energy of the impurity state depends on the imbalance in the bands, and the resonance forms deeper in the gap when the bands are imbalanced. Generating a non-magnetic impurity state only requires that particles scatter across a sign change in the gap, which is why it easy to generate states in the nodal system when Δ_e and Δ_h have the same sign. This is in stark contrast to the fully-gapped systems where the low-energy states simply do not form for $U_1 < |U_0|$. Since U_0 can now scatter particles across the nodes on the electron sheet, one might naively expect to generate states for $\delta_0 < 0$ as easily as when $\delta_0 > 0$. However, in the sign-unchanging nodal case, there are fewer states

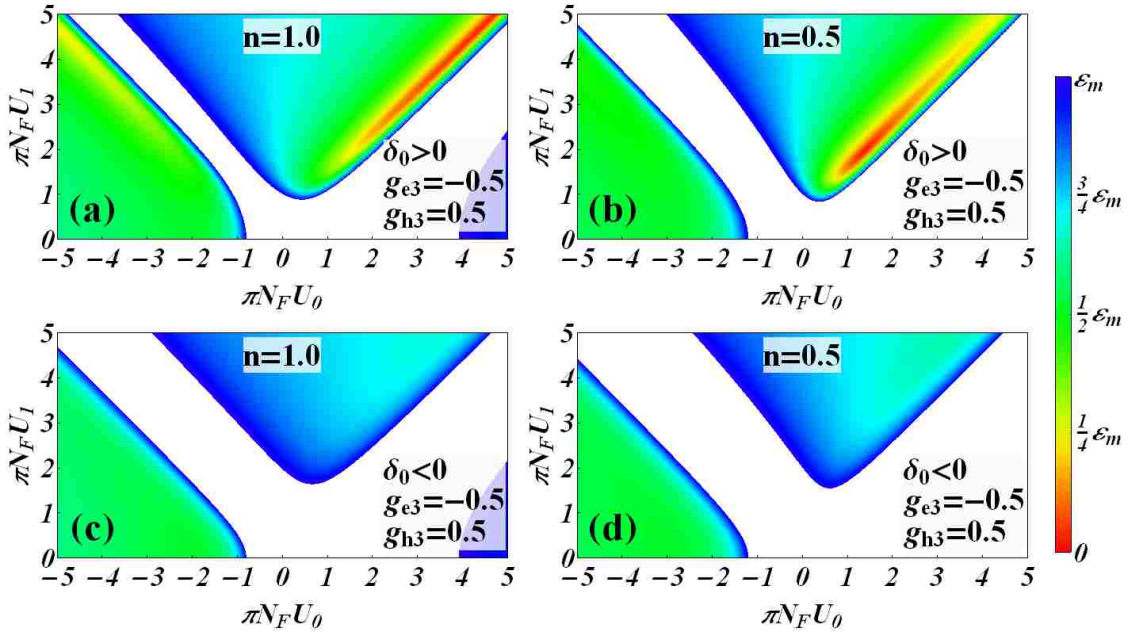

Figure 8.8: Energy of the low-lying impurity bound state in finite-bandwidth nodal system, r=1.3, with (a) n=1 and (b) n=1/2. The T-matrix has no poles below ε_m in white regions, and only the poles at negative U_0 and $U_1 < |U_0|$ are physical resonant states. In both cases, δ_0^{-2}=$n(1 + r^2/2)$ and $\varepsilon_m = 0.3\delta_0$. Energy is measured relative to ε_m.

on the electron sheet where the gap is opposite in sign to Δ_h, a fact that somewhat reduces the importance of U_1 in generating the resonant state. For the sign-unchanging case $\delta_0 < 0$, the resonances only form over a restricted region of the U_0-U_1 plane, and, as I shown in Figs. 8.7(c,d), there are two clear regimes where either U_0 or U_1 is more important. Of physical importance are the regions where $U_1 < |U_0|$. Thus, for both signs of δ_0, I find that it is relatively easy to generate low-energy resonant states in the nodal systems when U_0 is sufficiently strong, and the resonant state forms at even the smallest values of U_1 as per the results of Section .

I now consider the effects of finite bandwidth on the resonant states in the nodal systems. I take $g_{h3} = 0.5$ and $g_{e3} = -0.5$ so that the bands are hole-like and electron-like, respectively. As I show in Fig. 8.8, there are large regions of low-energy states for both signs of δ_0. When the g_{e3} is finite, it is c_e that controls the scattering between the nodes on the electron

sheet [142], and the formation of the low-energy state now depends strongly on the sign of U_0. Specifically, it is easier to generate states at negative U_0 since $g_{e3} < 0$. Compare the energy of the states at $U_1 < |U_0|$ for U_0 as shown in Fig. 8.8. The impurity state at large U_1 can be lower in energy for the sign-changing system; however, there is not much difference in the energy of the low-lying states at small U_1, regardless of the sign of δ_0.

The physically relevant impurity states, $U_1 < |U_0|$, are robust against an imbalance in the electron and hole contributions to the total DOS. Comparing Figs. 8.8(a,c) with Figs. 8.8(b,d), show that the band imbalance only slightly reduces the range of U_0 and U_1 over which the low-energy state can form. Thus, regardless of the sign of δ_0, I find that low-energy states will form over a substantial region of the $U_0 - U_1$ plane. As usual, the energy of the strong-scattering state is sensitive to the band structure, and I find that it always lies at finite bias in the presence of gap nodes.

I do not calculate or show $U_{1,m}$ since the g_{e0} and g_{e1} in Eq. (8.8) depend strongly on the energy of the resonant state, and solving finding Eq. (8.8) with $D(\omega) = 0$ is analytically impossible. However, it is clear from Figs. 8.7 and 8.8 that there is a shallow minimum in the energy of the accessible states for each fixed U_0. The shallowness of this minimum implies that most of the physical low-energy states remain close to ε_m so that they mix with the continuum states that form the DOS feature. While this results in a broadening of the resonant peaks relative to the bound states in the isotropic system, *any* peak below ε_m is relevant for probing the nodal structure of the gap.

In short, I find that the bound-state energy is sensitive to the details of the band structure, and that these details must be taken into account when interpreting the results of model-specific calculation. My analytical results provide insight into the varied tight-binding results for both the sign-changing s_{+-} state, where the bound state can form at low energies [133] but often remains close to the gap edge [131, 75, 132, 123, 121], and the s_{++} state, for which the bound state is wholly absent [121, 133]. I see that conditions for forming low-energy

states are generally the same for the isotropic and nodeless anisotropic gap. The situation is utterly different in the presence of gap nodes, where the importance of U_0 and U_1 is reversed for generating the impurity state. Consequently, I find that low-energy states form equally well for both the sign-changing and sign-unchanging nodal SC gaps. This remarkable result has direct consequences for probing the nodal structure of the gap by STS, a point I return to in Section 9.2. Now that I know the conditions under which to expect impurity states, I proceed in the next chapter to examine numerically the energy and spatial dependence of the local density of states near the single impurity

9. Two-band Tight-binding Model and the Local Density of States

Before I proceed to a more realistic model of iron-based superconductors, I consider a simple two-band tight-binding model, an instructive scenario wherein I can disentangle the effects due to the particle-hole asymmetry from those due to unequal densities of states on different Fermi surface sheets. I take the quasiparticle dispersion to be

$$\xi_{j\mathbf{q}} = -4t_j \cos q_x \cos q_y - \mu_j \,, \tag{9.1}$$

where the wave vectors q_x and q_y are measured in units of a^{-1}, the inverse of the distance between Fe ions, so that I work in the "unfolded" zone picture. For simplicity I set t_h as the unit of energy hereafter in this section. Setting $\mu_h/|t_h| = -\mu_e/|t_e| = 3$ ensures that the electron and hole Fermi surfaces have the same size and shape, with two hole sheets, one each centered at the Γ point and $(\pm\pi, \pm\pi)$, and two electron sheets, centered at the M points $(\pm\pi, 0)$ and $(0, \pm\pi)$, in the unfolded zone picture. The dispersion in Eq. (9.1) yields a van Hove singularity at the center of the band, where $\xi_{j\mathbf{q}} = -\mu_j$; therefore, for my choice of μ_e and μ_h, the density of states is featureless around the chemical potential which I take as zero energy.

I consider the superconducting order parameter that transforms according to an A_{1g} representation of the lattice point group. Therefore I take an isotropic gap, $\Delta_{h\mathbf{q}}$=Δ_h, on the hole pocket and an anisotropic gap of the form

$$\Delta_{e\mathbf{q}} = -\Delta_e \left[1 + \widetilde{r} \left(\cos q_x + \cos q_y\right)\right] \tag{9.2}$$

on the electron pocket. The choice of the anisotropy factor $\widetilde{r} = 4tr/(\mu_e - 4t)$ for small electron Fermi surface size maps the order parameter on that studied in the previous section. Indeed, expanding Eq. (9.1) near the point $(\pi, 0)$, I find that the electron Fermi surface is

approximately given by $(\pi - q_x)^2 + q_y^2 \equiv k_F^2 \approx 1 - \mu_e/(4t)$. A similar expansion of Eq. (9.2) yields the gap $\Delta_{e\mathbf{q}} \approx -\Delta_e[1 + r\cos 2\phi]$, where ϕ is the angle on the electron Fermi surface and is measured from [010], as I show in Fig. 7.1. An analogous expansion near the other M points yields the same $\Delta_{e\mathbf{q}}$, but with ϕ measured from [010] or [100] at $(-\pi, 0)$ and $(0, \pm\pi)$, respectively.

I work with the Hamiltonian $\check{H} = \sum_{j,\mathbf{q}} \widehat{H}_{j\mathbf{q}}$, where $\widehat{H}_{j\mathbf{q}} = \xi_{j\mathbf{q}}\widehat{\tau}_3 + \Delta_{j\mathbf{q}}\widehat{\tau}_1$ and $j = e, h$ is again the band index, and define the Green's function for the clean system via

$$\check{G}_0^{-1}(\mathbf{q};\omega) = \begin{bmatrix} \omega\widehat{\tau}_0 - \widehat{H}_{e\mathbf{q}} & 0 \\ 0 & \omega\widehat{\tau}_0 - \widehat{H}_{h\mathbf{q}} \end{bmatrix} . \tag{9.3}$$

I Fourier transform $\check{G}_0(\mathbf{q};\omega)$ to real space,

$$\check{G}_0(\mathbf{r}_i, \mathbf{r}_j;\omega) = \frac{1}{N_{q_x}N_{q_x}} \sum_{\mathbf{q}} \check{G}_0(\mathbf{q},\omega) e^{i\mathbf{q}(\mathbf{r}_i - \mathbf{r}_j)} , \tag{9.4}$$

with N_{q_i} the number of q-points in the q_i direction, and solve for the full Green's function using Eq. (7.10) and Eq. (7.11). The local density of states (LDOS) is $N(\mathbf{r},\omega)=2\sum_j N_j(\mathbf{r},\omega)$ from Eq. (7.12) with the factor of 2 for spin degeneracy. The calculations presented below have been done on a lattice with $N_{q_x}=N_{q_y}=1600$ with intrinsic broadening $\gamma=\Delta_h/40=0.005t$.

I set $\Delta_h=0.2t$ and take $\Delta_e=\delta_0\Delta_h$, where $|\delta_0|$ is determined from Eq. (7.2) with the DOS ratio $n = N_e(0)/N_h(0)$ that I defined earlier. Recall that $\delta_0 > 0$ corresponds to the sign-changing superconducting state state. I calculate the LDOS for both n=1 and n=1/2 by setting t_e=t_h and t_e=$2t_h$, respectively. With these parameters, the Green's function $g_{h3} = 1$ for the hole band while, for the electron band, $g_{e3} = -1$ and $g_{e3} = -0.9$ in the absence and presence of gap nodes, respectively. Recall that I measure the g_{j3} with respect to the $\pi N j(0)$.

As I did in Chapter 8, I measure the scattering potentials in units of $\pi N_F = \pi(N_e(0) + N_h(0))/2$, and I introduce $\bar{U}_i = \pi N_F U_i$ for notational simplicity. Here I focus on the moderate intraband potential $\bar{U}_0 = \pm 1.5$, and calculate the LDOS for $\bar{U}_1/|\bar{U}_0| = (1/3, 2/3, 1)$ in keeping

with the expectations [139, 140, 141] discussed in Chapter 6. For the fully-gapped systems, I estimate $U_{1,m}$ for each case by evaluating the Green's functions g_{ei} and g_{hi} at $\omega = 0$ for use in Eq. (8.8), while for the nodal case I find $U_{1,m}$ by inspection of the calculated LDOS. I present the LDOS for $U_{1,m}$ only when it differs appreciably from the LDOS for $\bar{U}_1/|\bar{U}_0| = (1/3, 2/3, 1)$.

9.1 Local Density of States in the Two-band System

In choosing the FS shape described above for the electron- and hole-like bands, I restrict myself to the situation where g_{e3} and g_{h3} are of opposite signs. I find that the energy of the impurity states agrees qualitatively with the predictions made in Sections 8.3 and 8.4. Specifically, I find that low-energy states generally do not form in the fully-gapped systems at physical values of finite scattering since. This is because a dominant interband scattering is required to scatter states between different signs of the gap on the electron and hole sheets. Furthermore, the intraband scattering controls the formation of the impurity state when there are nodes on the electron sheet. As such, it is easy to generate the low-energy resonance in the nodal systems.

I begin with the case $n = 1$, where the opposite particle-hole asymmetry of the two bands prevents the formation of the low-energy state for the nodeless systems when the scattering is moderate. I show this in Fig. 9.1(a,b) for the isotropic gap where the bound state never forms at $\omega = 0$. Furthermore, the lowest-energy resonance remains stuck to the LDOS feature at ε_m in the anisotropic system, see Figs. 9.1(c,d). These results are consistent with my analytic predictions.

As expected, when the gap has nodes, I find that sub-ε_m states form readily when there are nodes on the electron sheet. In Fig. 9.1(e,f), I show the impurity states for physical values of $\bar{U}_1 < |\bar{U}_0|$. As shown, the interband scattering has to be comparable to $|\bar{U}_0|$, an unlikely scenario, for a state to form for $\bar{U}_0 > 0$; however, the impurity state forms for all $\bar{U}_1$ when

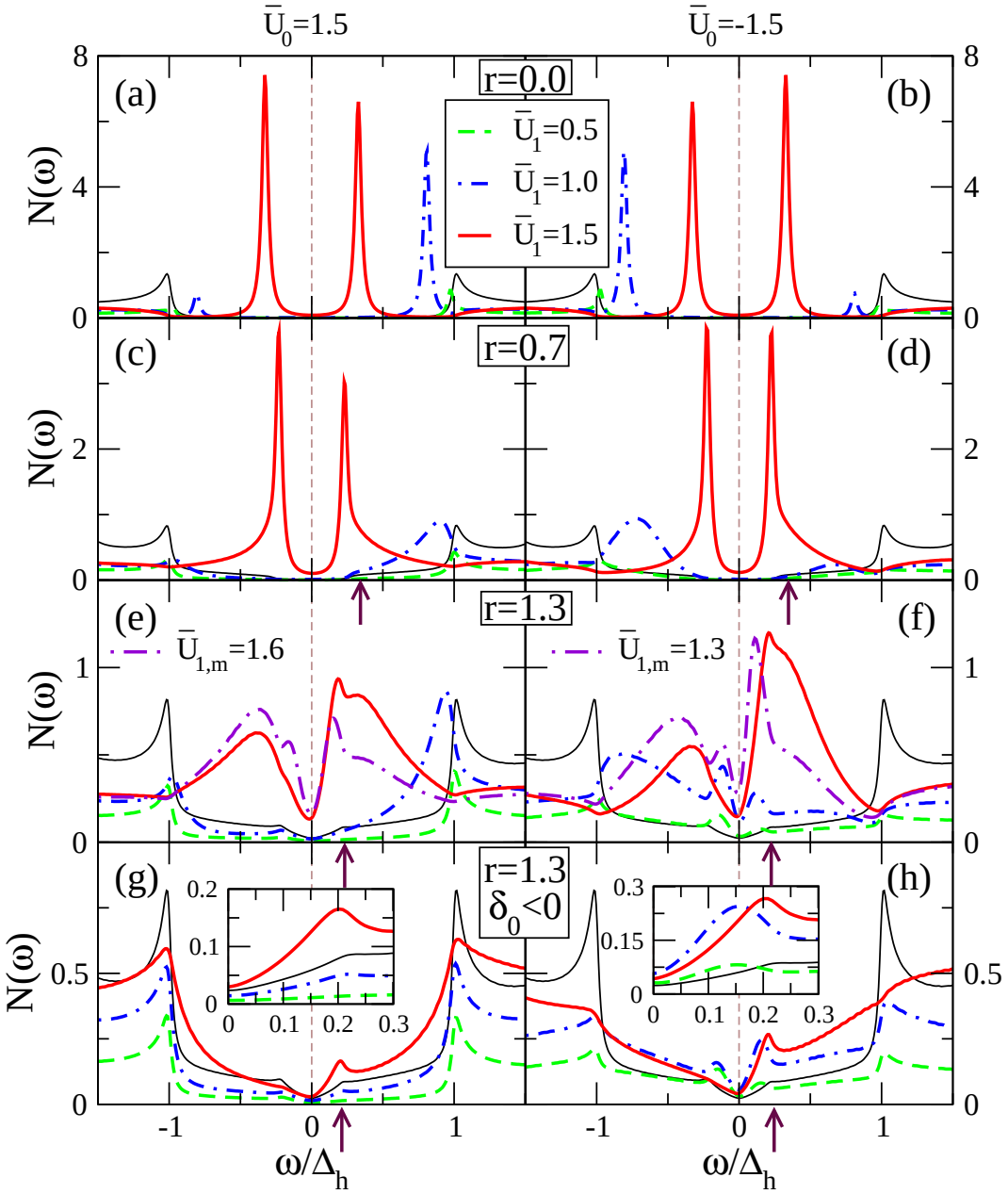

Figure 9.1: On-site LDOS for n=1 with moderate scattering, $\bar{U}_0$=±1.5 for (a,b) isotropic, (c,d) nodeless anisotropic, and (e,f) nodal gaps with $\delta_0 > 0$. Panels (g,h) are for nodal gap with $\delta_0 < 0$. The thin black line is the DOS of the clean system, and arrows mark the DOS feature at ε_m for the anisotropic cases. Low-energy impurity states form below ε_m in the nodal system even at small values of $\bar{U}_1$, but impurity states do not form near ω=0 in either of the fully-gapped systems. The LDOS for $\bar{U}_{1,m}$ is shown when $\bar{U}_{1,m} \not\approx |\bar{U}_0|$, but it is unlikely when $\bar{U}_{1,m} > |\bar{U}_0|$. The insets show close ups of the low-intensity positive-bias peaks. Note the different vertical scales.

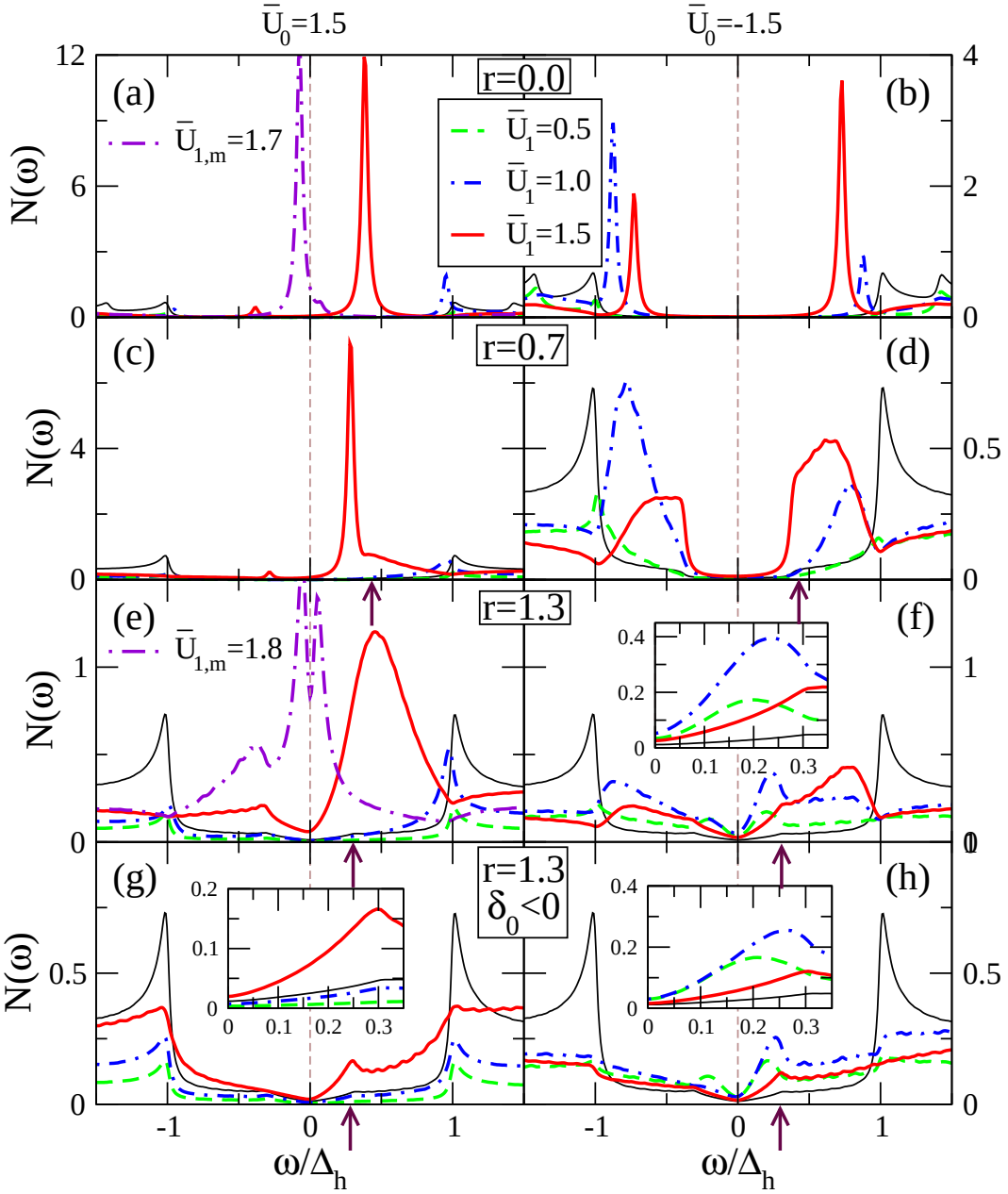

Figure 9.2: On-site LDOS for n=1/2 with moderate scattering, $\bar{U}_0$=±1.5, for (a,b) isotropic, (c,d) nodeless anisotropic, and (e,f) nodal gaps with $\delta_0 > 0$. Panels (g,h) are for nodal gap with $\delta_0 < 0$. The thin black line is the DOS of the clean system, and arrows mark the DOS feature at ε_m for the anisotropic cases. Low-energy impurity states form below ε_m in the nodal system even at small values of $\bar{U}_1$, but impurity states do not form near ω=0 in either of the fully-gapped systems. The LDOS for $\bar{U}_{1,m}$ is shown when $\bar{U}_{1,m} \not\approx |\bar{U}_0|$, but it is unlikely when $\bar{U}_{1,m} > |\bar{U}_0|$. The insets show close ups of the low-intensity positive-bias peaks. Note the different vertical scales.

$\bar{U}_0 < 0$. As I discussed in Section 8.4.2, scattering across a gap node is all that is required to generate an impurity state, hence the physical low-energy state forms equally well when $\delta_0 < 0$ as I show in Fig. 9.1(h). Also in keeping with my predictions from Section 8.4 is the fact that the impurity state stays close to ε_m. The height of the LDOS at the resonance energy depends upon $\bar{U}_1$, and the stronger peaks generally correspond to the larger values of $\bar{U}_1$ in the small-U_1 limit. The peaks for $\delta_0 < 0$ are also weaker than those for $\delta_0 > 0$, and it may be difficult to detect the impurity state generated by either a weak impurity or in the anisotropic s_{++} system. As I discuss in the next section, it is the shape, in real space, of the impurity state that can be used to discriminate the structure of the gap on the electron FS sheet. Hence, it is of paramount importance to carefully examine the LDOS to locate the impurity state.

The situation is different when the dominant contribution to the DOS comes from the hole bands. I show in Fig. 9.2 the LDOS for $n = 1/2$ and the same gap symmetry cases and scattering potentials as discussed above. The most obvious difference between these results and those in Fig. 9.1 is that here the impurity state energy for the fully-gapped cases depends strongly on the sign of U_0. As expected from the results presented in Fig. 8.5(f), the isotropic-gap bound state is lower in energy when $U_0 > 0$ but remains close to the gap edge at Δ_h for physical values of $\bar{U}_1$. My prediction for the nodeless anisotropic system is verified in Fig. 9.2(c,d) where I see that the impurity state is unlikely to form below ε_m. Although I find a sub-ε_m state for the anisotropic case at $\bar{U}_1{=}{-}\bar{U}_0{=}1.5$, it is unlikely that such a large interband scattering potential is physically relevant.

I also verify my prediction of the low-energy state in both the sign-changing and sign-unchanging nodal system. In fact, comparing Figs. 9.2(f) and (h), I see that the LDOS are remarkably similar for the two cases. As before, a larger interband scattering component generates a stronger resonance, and the resonances generally remain close to the gap feature

at ε_m. Thus, I see that the formation of the low-energy state in the nodal systems are robust against a moderate imbalance in the bands.

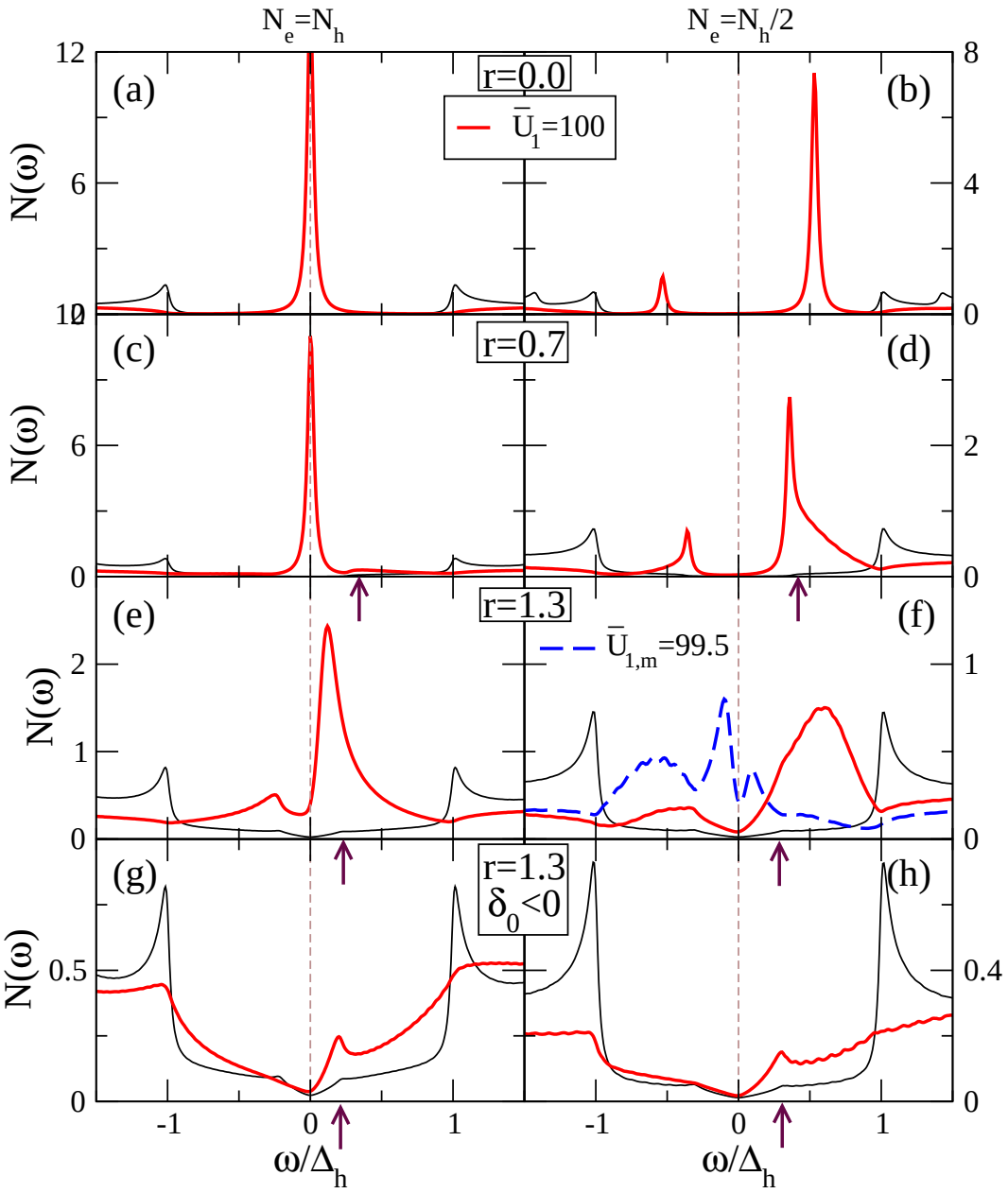

Figure 9.3: On-site LDOS for strong scattering, $|\bar{U}_0|=\bar{U}_1=100$, for (a,c,e,g) n=1 and (b,d,f,h) n=1/2. When the bands are balanced, n=1, the strong scattering state is at low energy. When the bands are imbalanced, the state forms away from $\omega = 0$ for of the gap shapes. As shown in panel (f), the nodal s_{+-} state has a low-energy peak in the LDOS at $U_{1,m} = 99.5$. Note the different vertical scales for the cases. The thin black line is the DOS of the clean system.

To examine the impurity state in the strong-scattering limit, I set $|\bar{U}_0| = \bar{U}_1 = 100$, where I find that the shape of the LDOS does not depend strongly on the sign of $\bar{U}_0$. As I show in Fig. 9.3, the location of the strong-scattering state depends on the symmetry of the gap. For fully-gapped systems at n=1, the bound state forms at $\omega = 0$ as shown in Figs. 9.3(a,c); however, the state moves to finite bias when the bands are imbalanced, see Figs. 9.3(b,d).

As in the case of finite scattering, the low-energy state is more likely to form when there are nodes on the electron FS sheet. This is true for both signs of δ_0, I show in Fig. 9.3(e)-(h). The only situation in which I do not find a sub-ε_m state at $|\bar{U}_0| = \bar{U}_1 = 100$ is for the nodal s_{++} state when the bands are imbalanced; however, there is a sub-ε_m state when $\bar{U}_1 = 99.5$. Since the low-energy state forms for $\bar{U}_1$ within one percent of $\bar{U}_0$, this indicates that the resonance very nearly forms even when the bands are imbalanced. The fine-tuning of $\bar{U}_1$ required implies that such a state is unlikely to form in a physical system if the bands' DOS are sufficiently different

9.2 Spatial Dependence of the Resonant State

So far I have shown that the presence of the low-energy impurity state is generally a hallmark of the gap nodes on the electron FS sheets, especially when the bands are particle-hole asymmetric. Even though the sub-ε_m state is not likely to form in the nodeless anisotropic system, it is clear from my results in Figs. 9.1(c,d) and 9.2(c) that such a state is possible when the interband and intraband scattering parameters are of comparable strength. I now explore the spatial dependence of the impurity state to obtain a fuller picture of the differences and similarities between the various gap structures on the electron sheet. Of course the resonance peak decays away from the impurity site, and the decay length depends on the electronic structure and the potential strength. The decay is isotropic for the s_{+-} system; however, the decay can be direction-dependent for the anisotropic gaps, depending on whether the impurity state forms above or below ε_m and whether the gap has nodes. This

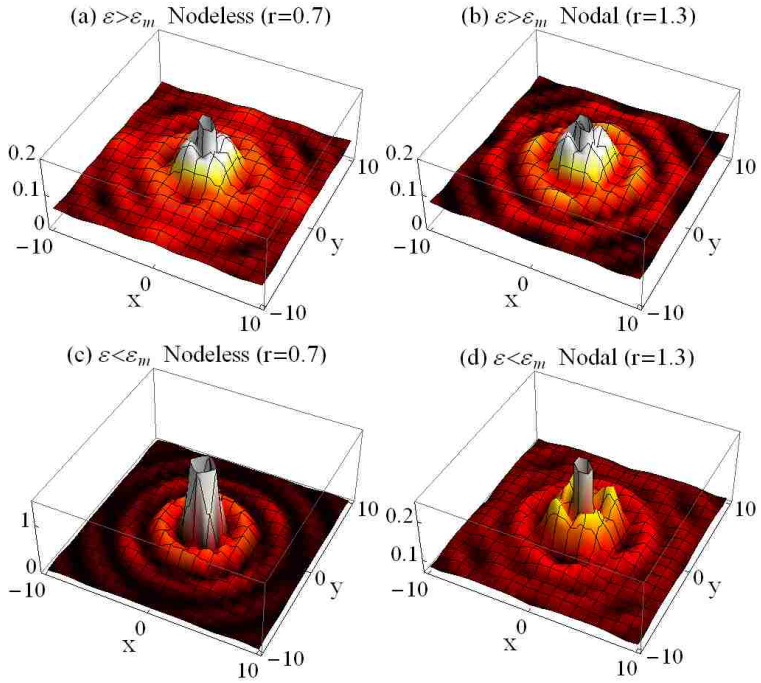

Figure 9.4: Impurity state for the two-band model with (a,c) nodeless, r=0.7, and (d,e) nodal, r=1.3, anisotropic gaps. Panels (a) and (b) show the positive-bias peaks that form at $\varepsilon \approx 0.7$, above ε_m, for $\bar{U}_1 = \bar{U}_0 = 1.5$. Panels (c) and (d) show the positive-bias peaks that form at $\varepsilon \approx 0.23$, below ε_m, for $\bar{U}_1 = -\bar{U}_0 = 1.5$. The impurity sits at $(0, 0)$, and x and y are the axes for the crystallographic unit cell.

is the effect I emphasize in this section and then pay further attention to in my subsequent analysis of the more realistic band structure relevant for the pnictides.

The impurity states above ε_m in both of anisotropic systems display a four-fold symmetric decay pattern, which I show in Fig. 9.4(a) and (b). The shape of the state is virtually identical in the immediate vicinity of the impurity. While there can be differences in the shape of the state far from the impurity, there the decay pattern is insufficient to determine the presence or lack of gap nodes. However, the similarity between the spatial profiles disappears once the resonant state forms below ε_m. When the impurity state is below ε_m, there is little difference between the bound state in the nodeless system and the bound states that form in the presence of isotropic s_{+-} gap. In Fig. 9.4(c), I show the spatial dependence of the sub-ε_m state that forms in the nodeless system. As shown, the impurity state exhibits almost

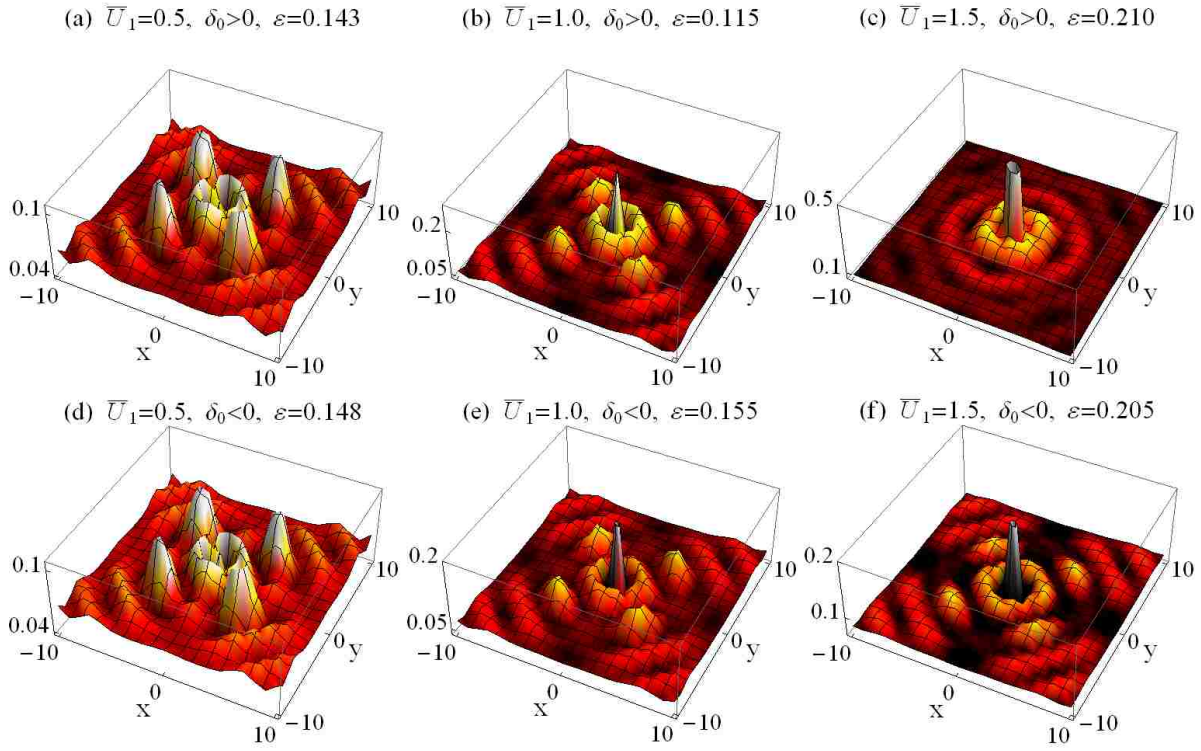

Figure 9.5: Sub-ε_m impurity state for the two-band model with n=1 and nodes, r=1.3, on the electron FS sheets. Shown are the positive-bias peaks for $\bar{U}_0 = -1.5$ with (a,d) $\bar{U}_1$=0.5, (b,e) $\bar{U}_1$=0.5, and (c,f) $\bar{U}_1$=0.5 that I present in Fig. 9.1(f) and (h). Panels (a), (b), and (c) are for the sign-changing case while panels (c), (d), and (e) are for the sign-unchanging case. The impurity sits at $(0, 0)$, and x and y are the axes for the crystallographic unit cell.

circular Friedel oscillations as it decays with distance from the impurity, which indicates that the resonance forms at an energy for which there are no states in the clean system. In contrast, the impurity state in the nodal system is still four-fold symmetric even below ε_m, as I show in Fig. 9.4(d).

This four-fold symmetry in the nodal system is much more prominent when the impurity state forms far below ε_m, and the resonance decays much more slowly along the Fe-lattice axes. This is clearly seen in the spatial mappings that I show in Fig. 9.5 for both the sign-changing and sign-unchanging systems with n=1. As shown, there is little about the resonance state generated by a particular value of $\bar{U}_0$ and $\bar{U}_1$ that can discriminate between the two possible signs of δ_0.

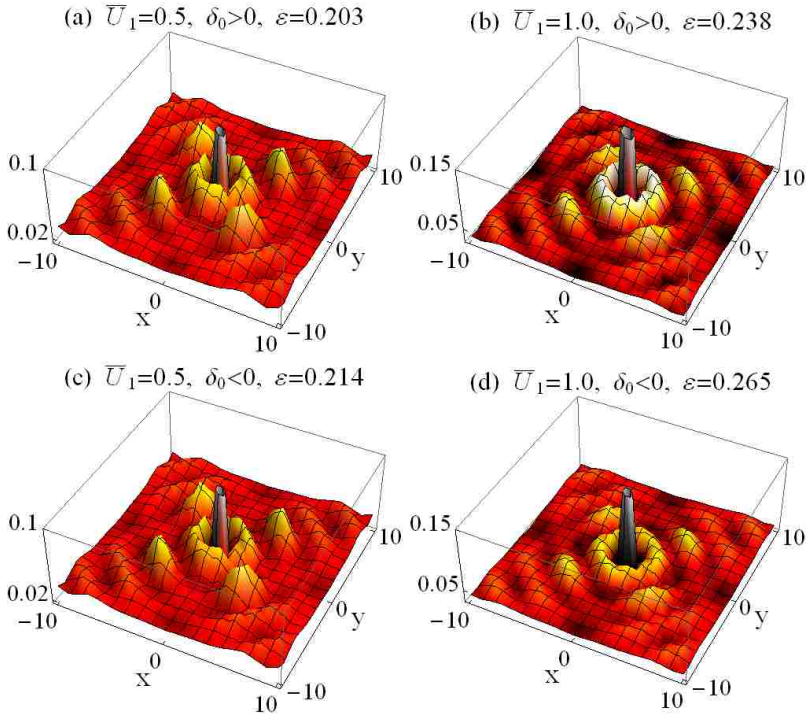

Figure 9.6: Sub-ε_m impurity state for the two-band model with n=1/2 and nodes, r=1.3, on the electron FS sheets. Shown are the positive-bias peaks for $\bar{U}_0 = -1.5$ with (a,c) $\bar{U}_1$=0.5 and (b,d) $\bar{U}_1$=1.0 that I present in Fig. 9.2(f) and (h). Panels (a) and (b) are for the sign-changing case while panels (c) and (d) are for the sign-unchanging case. The impurity sits at $(0, 0)$, and x and y are the axes for the crystallographic unit cell.

The spatial features of the impurity state are the same for resonances in the unbalanced-band system, which I show in Fig. 9.6 for n=1/2. As for the balanced-band scenario, the shape of the sate is four-fold symmetric with its longer decay length along the Fe-lattice axes. It is clear then, that the shape of the low-energy resonance is key to identifying the nodal structure of the gap. The four-fold symmetry of the low-energy state is much more pronounced when there are gap nodes on the electron FS sheet. Unfortunately, the imbalance in the bands does not introduce any features into the shape of the state that are capable of discriminating between the two signs of δ_0.

10. Realistic Four-band Tight-binding Model

I now verify my findings within the context of more realistic models of the pnictide band structure. Several studies of impurity-induced resonances have focused on extended s-wave superconductivity and find that resonances induced by non-magnetic impurities do not develop in the vicinity of the chemical potential [121, 131, 75]. References [121] and [131], use the minimal two-band model proposed by Raghu, *et al.* [73], that has also been used to study the consequences of s-wave $\cos(k_x)\cos(k_y)$ superconductivity in the pnictides [87], and find that non-magnetically-induced resonances develop only near the gap edge. This is in stark contrast to the low-energy impurity states discussed previously in this study and those from Refs. [75, 133] that develop well within the gap. The discrepancy between these two general cases arises because, as we discussed above, the details of the chosen tight-binding dispersion have important consequences for the formation of impurity states.

The minimal two-band model from Ref. [73], and used in Refs. [121] and [131], does reproduce the pnictide FS topology; however, it gives the relative Fermi-level densities of states as $N_e(0) \approx 4.9 N_h(0)$, as I show in Fig. 10.1(a), with particle-hole anisotropy given by the Green's functions $g_{e3} \approx -3.7\pi N_e(0)$ and $g_{h3} \approx 0.4\pi N_h(0)$. Using the formalism presented in Section 8.3.3, I estimate the bound-state energy for the isotropic s_{+-} state, which I show in Fig. 10.2. As shown, the impurity state remains close to the gap edge if it forms at all. I also checked for resonances numerically by calculating the LDOS with this model, and I found that the bound states that do form remain close to the gap edge. Furthermore, I do not find impurity states far from the gap edge in either of the anisotropically gapped systems. I conclude that the large degree of particle-hole anisotropy of this model prevents the formation of low-energy states. Thus, while it reproduces the FS topology, the model

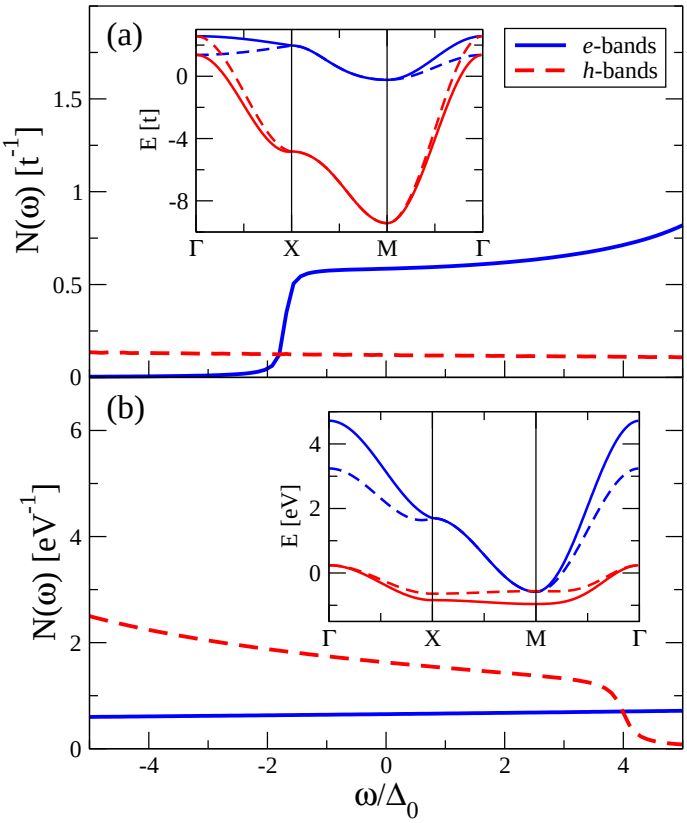

Figure 10.1: Normal state electron and hole DOSs for (a) two-band model with hopping integral t from Ref. [73] and (b) four-band model from Ref. [74]. Insets: Band structures for the respective models; symmetry-point notation is for the 1111-type materials [72, 137, 146, 65].

presented in Ref. [73] does not give resonant states due to the mismatch of the electron and hole bands.

I follow, instead, the four-band model presented in Ref. [74], which fits the Fermi-surface topology and Fermi velocity as determined by the local-density approximation, and whose band structure and normal-state DOS I show in Fig. 10.1(b). This four-band model estimates the relative contributions of electrons and holes to the Fermi-level DOS as $N_h(0) \approx 2.5N_e(0)$ or, in my notation, $n \approx 0.4$. It also estimates the Green's functions $g_{e3} \approx -\pi N_e(0)$ and $g_{h3} \approx 1.2\pi N_h(0)$, where g_{j3} and $N_j(0)$ represent the total contribution from the bands of the jth type. As I show below, the band structure from Ref. [74] allows for the formation of impurity states under the conditions I have discussed above.

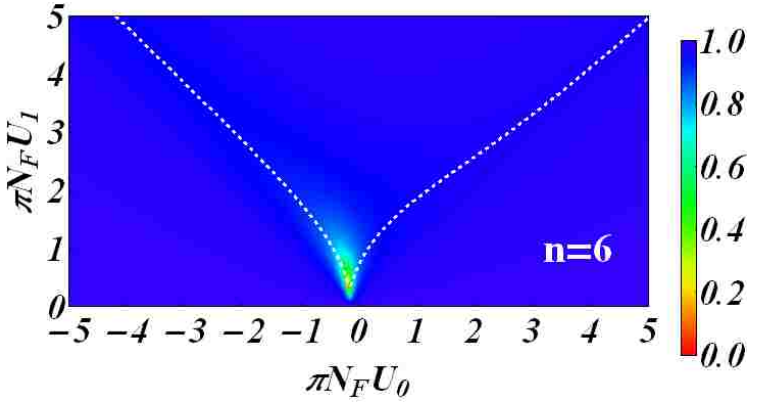

Figure 10.2: Energy of the impurity state in isotropic s_{+-} for the minimal two-band model of Ref. [73], as estimated using the formalism in Chapter 8. Impurity states are nearly absent for physical values of $\pi N_F U_1$. The dashed line is $\pi N_F U_{1,m}$ as taken from Eq. (8.15).

I extend the formalism in Chapter 9 to include four bands so that the eight-by-eight matrix Green's function $\check{G}_0(\mathbf{k};\omega)$ is defined by

$$\check{G}_0^{-1}(\mathbf{k};\omega) = \omega\mathbf{I} - \begin{bmatrix} \widehat{H}_{\alpha_1\mathbf{k}} & 0 & 0 & 0 \\ 0 & \widehat{H}_{\alpha_2\mathbf{k}} & 0 & 0 \\ 0 & 0 & \widehat{H}_{\beta_1\mathbf{k}} & 0 \\ 0 & 0 & 0 & \widehat{H}_{\beta_2\mathbf{k}} \end{bmatrix}. \tag{10.1}$$

Here $\mathbf{I}$ is the eight-by-eight identity matrix and the band index j now takes the values α_1, α_2, β_1, and β_2. From Reference [74], the tight-binding dispersions are

$$\varepsilon_{\alpha_i\mathbf{k}} = -t_{\alpha_i}\left(\cos\left(k_x\right) + \cos\left(k_y\right)\right) - t'_{\alpha_i}\cos\left(k_x\right)\cos\left(k_y\right) - \mu_{\alpha_i} \tag{10.2}$$

for the two hole bands and

$$\varepsilon_{\beta_i\mathbf{k}} = -t_{\beta i}\left(\cos\left(k_x\right) + \cos\left(k_y\right)\right) - t'_{\beta_i}\cos\left(\frac{k_x}{2}\right)\cos\left(\frac{k_y}{2}\right) - \mu_{\beta_i} \tag{10.3}$$

for the two electron bands with i=1,2. Here I work in the folded BZ picture, corresponding to two Fe atoms per unit cell with the lattice constant $\tilde{a}$=$\sqrt{2}a$. The momenta k_x and k_y are

therefore measured in units of $\tilde{a}^{-1}$. The tight-binding parameters from Ref. [74] are

$$(t_{\alpha_1}, t'_{\alpha_1}, \mu_{\alpha_1}) = (-0.3, -0.24, 0.6) \tag{10.4a}$$

$$(t_{\alpha_2}, t'_{\alpha_2}, \mu_{\alpha_2}) = (-0.2, -0.24, 0.4) \tag{10.4b}$$

$$(t_{\beta_1}, t'_{\beta_1}, \mu_{\beta_1}) = (-1.14, -0.74, -1.70) \tag{10.4c}$$

$$(t_{\beta_2}, t'_{\beta_2}, \mu_{\beta_2}) = (-1.14, 0.74, -1.70)\,. \tag{10.4d}$$

The tight-binding parameters in Eq. (10.4) yield the Fermi surface topology that I show in Fig. 10.3, which consists of two hole ($\varepsilon_{\alpha_i \mathbf{k}}$=0) and two electron ($\varepsilon_{\beta_i \mathbf{k}}$=0) FS sheets centered at the high-symmetry points Γ and M. The electron and hole contributions to the Fermi level DOS are $N_h(0) = N_{\alpha_1}(0) + N_{\alpha_2}(0)$ and $N_e(0) = N_{\beta_1}(0) + N_{\beta_2}(0)$, respectively. Here all energies are measured in electron volts (eV).

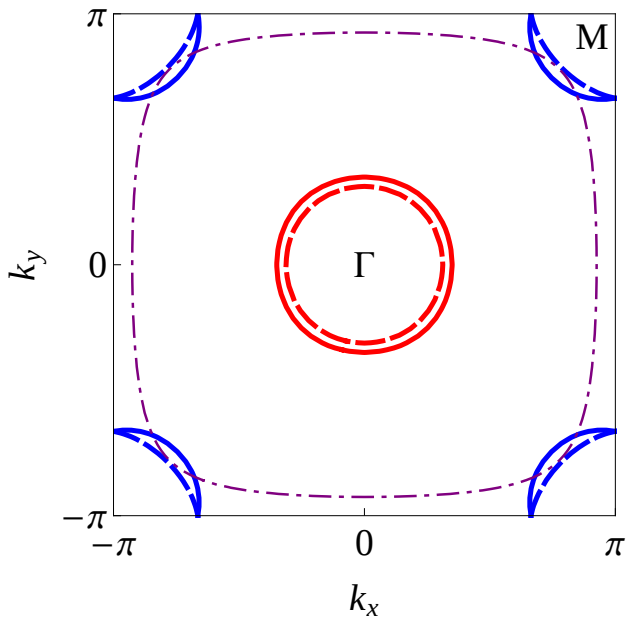

Figure 10.3: Fermi surfaces for bands $\varepsilon_{\alpha_i \mathbf{k}}$ and $\varepsilon_{\beta_i \mathbf{k}}$, i=1,2. Two hole pockets from $\varepsilon_{\alpha_1 \mathbf{k}}$ (dashed) and $\varepsilon_{\alpha_2 \mathbf{k}}$ (solid) are centered at the Γ point of the folded Brillouin Zone. Two electron pockets from $\varepsilon_{\beta_1 \mathbf{k}}$ (dashed) and $\varepsilon_{\beta_2 \mathbf{k}}$ (solid) are centered at the M point. The thin dash-dotted line gives the nodal line for the gap $\Delta_{\beta_2 \mathbf{k}}$ on $\varepsilon_{\beta_2 \mathbf{k}}$ for $\tilde{r}$=8.56. This corresponds to maximal and minimal gap on the electron FSs of $\Delta_{\beta+}$=1.94Δ_0 and $\Delta_{\beta-}$=−0.3Δ_0, respectively. The momentum is measured in units of $\tilde{a}^{-1}$.

I again consider the isotropic gap $\Delta_{\alpha_i \mathbf{k}}$=$\Delta_h$ on the hole FS sheets, and I define the gap on the electron sheets to be

$$\Delta_{\beta_1 \mathbf{k}} = -\Delta_e \left(1 + \tilde{r} \cos\left(\frac{k_x}{2}\right) \cos\left(\frac{k_y}{2}\right)\right) \tag{10.5a}$$

$$\Delta_{\beta_2 \mathbf{k}} = -\Delta_e \left(1 - \tilde{r} \cos\left(\frac{k_x}{2}\right) \cos\left(\frac{k_y}{2}\right)\right) , \tag{10.5b}$$

where the anisotropy of $\Delta_{\beta_i \mathbf{k}}$ is set by

$$\tilde{r} = r \frac{4t_{\beta_2} + t'_{\beta_2}}{2t_{\beta_2} - 2\mu_{\beta_2}} . \tag{10.6}$$

With this gap profile, the gap extrema on the electron FSs are $\Delta_{\beta,max} \approx -\Delta_e (1 + 0.110\tilde{r})$ and $\Delta_{\beta,min} \approx -\Delta_e (1 - 0.152\tilde{r})$, respectively. I choose $\tilde{r}$=4.91 for the nodeless and $\tilde{r}$=8.56 for the nodal anisotropic gaps so that $\Delta_{\beta,min}$=$-\Delta_e|r-1|$ are the same as the gap minima considered in Chapter 9 for $r = (0, 0.7, 1.3)$.

I set Δ_h=0.06 eV and Δ_e=$\delta_0 \Delta_h$, with $|\delta_0|$ as determined from Eq. (7.2) using the $N_e(0)$ and $N_h(0)$ defined above. Although this value for Δ_h is larger than what is found experimentally [79, 96, 97, 98], it is still much smaller than the bandwidth and captures the relevant physics. All of my calculations for this section are performed on a 2000 by 2000 k-space grid and take the intrinsic broadening γ=$\Delta_h/40$=0.0015 eV. With these parameters, the Green's functions $g_{h3} = 1.2\pi N_h(0)$ and $g_{e3} = -\pi N_e(0)$ at the chemical potential.

10.1 Local Density of States in the Four-Band System

I find that impurity states in the four-band model of Ref. [74] are generally consistent with the results discussed previously in this study. In particular, the details of the band structure from Ref. [74], and hence the resulting location and shape of the impurity state, are closest to those of the n=1/2 case that I considered in Section 9.1. Unless otherwise specified, all the comparisons I make with the results from Section 9.1 are for the n=1/2 results shown in Fig. 9.2.

In Fig. 10.4, I show the LDOS for the same scattering parameters as in Section 9.1. As before, the particle-hole asymmetry causes the impurity-state energy to depend strongly on the sign of U_0. As expected, the low-energy states do not form when the FS sheets are fully-gapped, but the states readily form when there are nodes on the electron sheets. A comparison of Figs. 10.4(f) and (h) shows that the impurity state forms in the nodal systems for physical $\bar{U}_1$ regardless of the sign of δ_0. This, and the proximity of impurity state to ε_m, agree with both my predictions from Section 8.4 and the results of Section 10.4.

Although I do not present the strong-scattering LDOS for the fully-gapped bands, I have verified that the low-energy state does not form away from $U_{1,m}$ for these gap symmetries within the current four-band model. I focus instead on the nodal system as I did in Section 9.1. As I show in Fig. 10.4, there is likely no low-energy state for $\bar{U}_1 = |\bar{U}_0| = 100$. As before for $n = 1/2$, the sub-ε_m peak forms instead at $\bar{U}_1 = 99.5$ which indicates that the strong-scattering state very nearly in the nodal system. Consequently, since the resonance does not form in the fully-gapped cases, any low-energy resonance heralds the presence of nodes in the gap on the electron sheet.

10.2 Spatial Dependence of the Resonant State

Compare the impurity states for the four-band system with their counterparts, *i.e.*, same $\bar{U}_0$ and $\bar{U}_1$, for the two-band system that I show in Figs. 10.6 and 9.5, respectively. Except for the overall spectral intensity, the resonant states are very nearly identical in the two different models. Presumably, the differences that appear result from the fine details of the two models but don't affect the salient features of the decay pattern. This result is not as surprising as one might think. Since I have approximated the interband scattering as being the same for the FS sheets of the same type, the two electron(hole) conduction bands effectively behave as a single band. The validity of this approximation comes from the fact the two bands of each type are nearly degenerate in energy and have similar dispersion near

the chemical potential. Hence the four-band aspect is not important for to the overall results of the model.

Given the nearly identical results for the two- and four-band models, I have verified the usefulness of the simple two-band approach. Specifically, if one has a good first principles calculation of the strength of the impurity potential, then an appropriate two-band model should effectively predict the energy and shape of the resonant state for any of the gap symmetries. Of course, the appropriate two-band model must mimic the pnictide dispersions near the Fermi level as closely as possible.

I emphasize that the physics in multiband systems, *e.g.*, the pnictides, can be extremely sensitive to the details of the band structure, and it is clear that experimental verification of the gap node structure in the pnictides will depend on the electron and hole contributions to the Fermi-level DOS. This observation is in keeping with a recent suggestion [147] that the apparent conflict between measurements indicating the presence [107] and absence [147] of gap nodes in the nominally identical $BaFe_2(As_{0.67}P_{0.33})_2$ and $BaFe_2(As_{0.7}P_{0.3})_2$, respectively, is due to a large difference in the band masses, and hence the partial densities of states near the Fermi level. Measurement of the effective mass in $BaFe_2(As_{0.37}P_{0.63})_2$ [81] suggests that the hole band can be a factor of two heavier than the electron band, a situation that I have discussed at length in this study. Measurements also show that the band masses are effectively identical to one another in the Fe-1111 compounds [72, 138, 137], which increases the likelihood that low-energy states will form in these materials in the presence of strong scattering even if the bands are fully-gapped. I therefore suggest a STS experiment to map the resonant state near a surface impurity on a nominally-clean pnictide. The accompanying spatial profile of any low-lying resonant states will be well-suited to verifying the nodal structure of the superconducting gap in both 122-type and 1111-type materials.

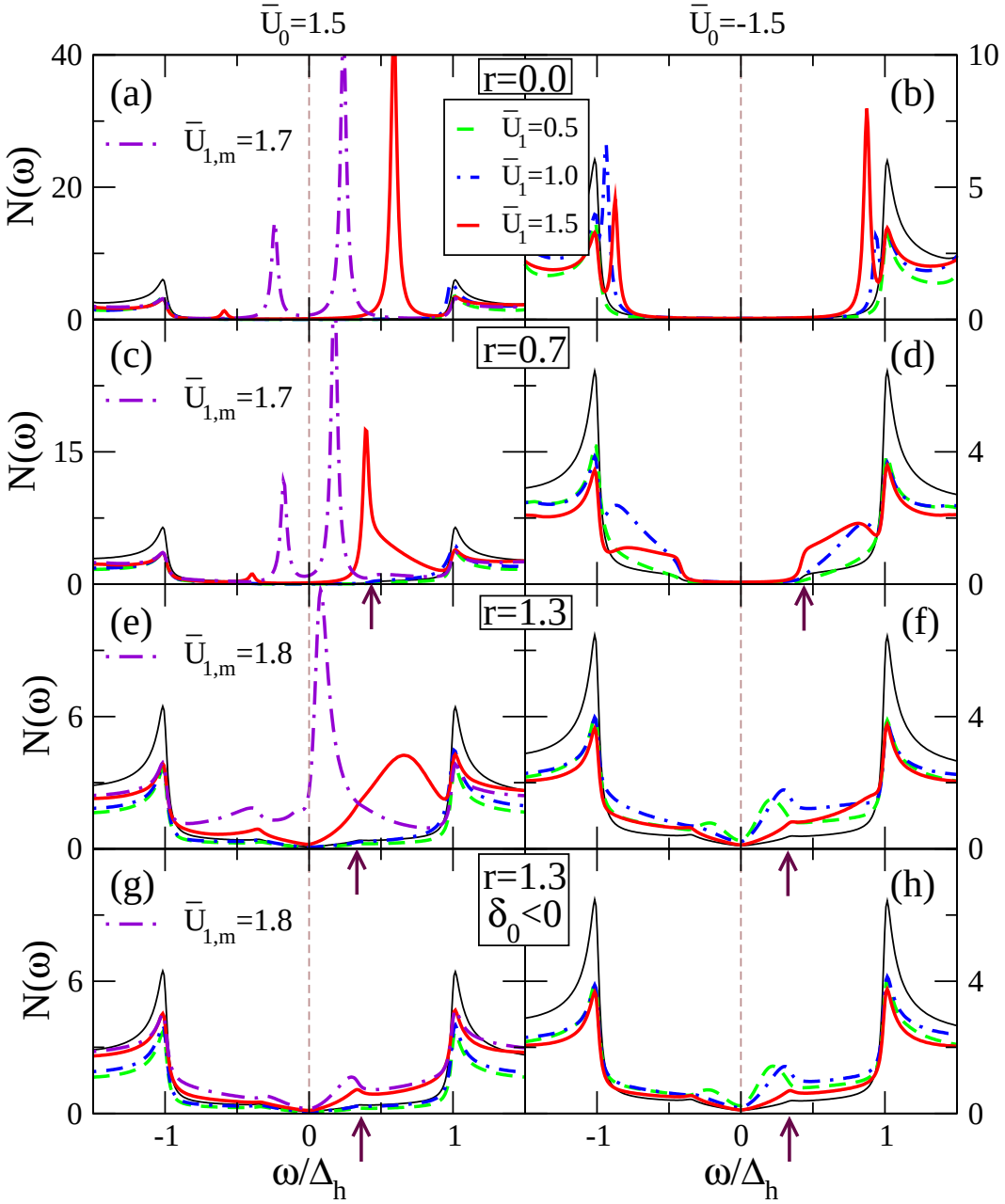

Figure 10.4: Evolution of on-site LDOS (eV^{-1}) for four-band model with moderate scattering, $\bar{U}_0$=$\pm$1.5, for (a,b) isotropic, (c,d) nodeless anisotropic, and (e,f) nodal gaps for $\delta_0 > 0$. Panels (g,h) are for nodal gap with $\delta_0 < 0$. The thin black line is the DOS of clean system, and arrows mark the DOS feature at ε_m for the anisotropic cases. Low-energy impurity states form below ε_m in the nodal system even at small values of $\bar{U}_1$, but impurity states do not form near ω=0 in either of the fully-gapped systems. The LDOS for $\bar{U}_{1,m}$ is shown when $\bar{U}_{1,m} \not\approx |\bar{U}_0|$, but it is unlikely when $\bar{U}_{1,m} > |\bar{U}_0|$. The insets show close ups of the low-intensity positive-bias peaks. Note the different vertical scales.

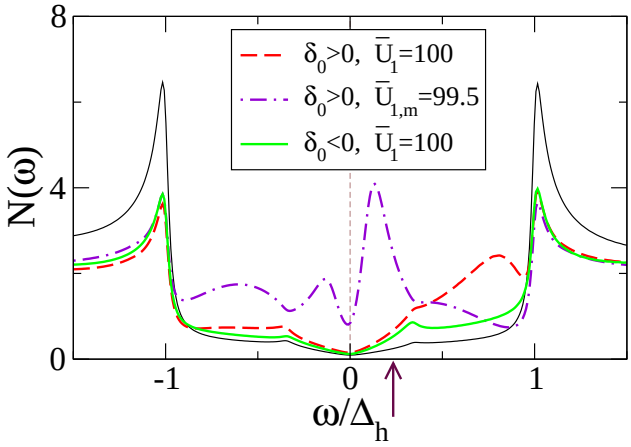

Figure 10.5: On-site LDOS for strong scattering, $|\bar{U}_0|=\bar{U}_1=100$, for (a) $n=1$ and (b) $n=1/2$. Note the different vertical scales for the two cases. The thin black line is the DOS of the clean system.

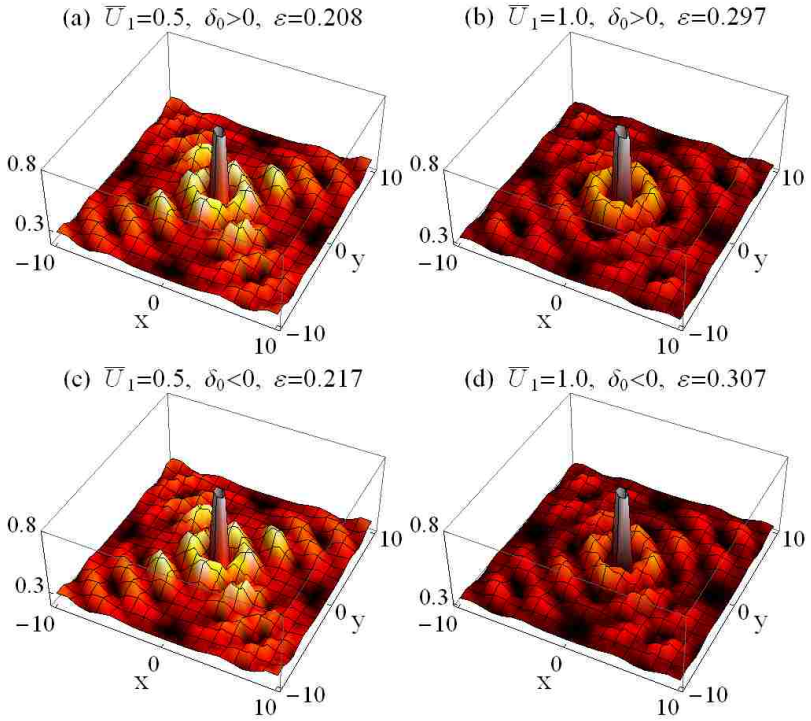

Figure 10.6: Sub-ε_m impurity state for the four-band model with nodes, r=1.3, on the electron FS sheets. Shown are the positive-bias peaks for $\bar{U}_0 = -1.5$ with (a,c) $\bar{U}_1$=0.5 and (b,d) $\bar{U}_1$=1.0 that I present in Fig. 10.4(e) and (f). Panels (a) and (b) are for the sign-changing case while panels (c) and (d) are for the sign-unchanging case. The impurity sits at $(0, 0)$, and x and y are the axes for the crystallographic unit cell.

11. Conclusions

There are two major results contained in this thesis. First, motivated by experiments on the heavy-fermion $CeCoIn_5$, I considered the effect of classical magnetic fluctuations on the normal-to-superconducting transition in two-dimensional s-wave and d-wave superconductors. I considered both the uniform and inhomogeneous (FFLO) superconducting states, and I investigated the order of the transition into each. My main finding is that there exists a range of temperatures, in the vicinity of the onset of the modulated state, where the coupling to magnetic fluctuations causes the transition to become first order into both the uniform and the modulated states. The width of the temperature range increases with the strength of coupling to the magnetic fluctuation and is generally greater for s-wave systems.

Since the regime of interest in experiment occurs for temperatures $T/T_c \sim 0.2 - 0.5$, I considered only classical thermal fluctuations. My approach outlined a new, generic, path towards a first order normal-to-superconducting transition, and demonstrated an important experimentally observed feature: the separation between the onset of the first order transition and the transition into a modulated state. It suggests that accounting for magnetic fluctuations, which are known to exist in heavy fermion and other related compounds, affects the shape of the transition lines, the order of the transition, and the behavior of the thermodynamic properties at the transition. In my analysis, the transition remains second order as $T \to 0$, but it remains for future studies to see whether accounting for the quantum dynamics of spins changes this conclusion. Among other potentially interesting avenues of research are whether impurity scattering, which is known to suppress the inhomogeneous LO state, enhances or shrinks the first order transition regime, and what the results of combining the Zeeman field with the orbital coupling and vortex physics are.

Second, I presented a detailed analysis of the non-magnetic, single-impurity problem in multiband superconducting systems, examining the conditions under which resonances exist and the potential they have to resolve the outstanding issue of the gap shape in the pnictides. I considered both analytical and numerical two-band models and then used them to explain the results of a more realistic four-band model. I found that low-energy resonances are generally absent from the fully-gapped states except, perhaps, in the strong-scattering limit for materials in which the particle and holes bands are very nearly balanced. I found that the low-energy state is more likely to form when the gap has nodes on one or more of the Fermi surface sheets, where the states form via the same mechanism as in the single-band system with nodes. I found also that the low-energy state in the nodal system has a four-fold symmetric shape, with the impurity state decaying more slowly along the principle axes of the crystallographic unit cell. The formation of a low energy state and its characteristic shape would provide the 'smoking gun' evidence for the nodal state. Even though the physics of the pnictides is sensitive to the details of the electronic band structure, I find that the formation of low-energy state in the nodal state is generally robust against moderate changes to the band structure. For the nodal case, which is dominated by the intraband scattering, I found that the low-energy resonance does not discriminate between the sign-changing (s_{+-}) and sign-unchanging (s_{++}) cases and can only be used to verify the presence of nodes on the Fermi surface sheet.

The two electron sheets and the two hole sheets in the pnictides are nearly degenerate, and this justifies my approach of using a two-band model to mimic materials with four Fermi surface sheets. While this approach that has been utilized many times for the pnictides with varying results, I found that the details of the band structure near the Fermi level are important and affect the energy of the impurity state. Thus, I chose the parameters in my two-band model to approximate the Fermi-level properties of the four-band model, and I found that my two-band approach was sufficient to capture the salient physics. In this study,

I have ignored the suppression of the superconducting gap in the vicinity of the impurity. Since I consider only a single impurity, I also ignore the lifting of the nodes dues to finite impurity concentration. Neither of these affect the qualitative description of the impurity effect in the pnictides, and I leave them to future studies.

Bibliography

[1] H. Onnes, Leiden Comm. **120b - 120c** (1911).

[2] V. Ginzburg and L. Landau, Zh. Eksperim. i Teor. Fiz. **20**, 1064 (1950).

[3] L. Gor'kov, Sov. Phys. JETP **9**, 1364 (1959).

[4] I. Giaever, Phys. Rev. Lett. **5**, 147 (1960).

[5] J. Bardeen, L. N. Cooper, and J. R. Schrieffer, Phys. Rev. **108**, 1175 (1957).

[6] W. Meissner and R. Ochsenfeld, Naturwissenschaften **21** (1933).

[7] A. Abrikosov, Sov. Phys. JETP **5**, 11174 (1957).

[8] I. I. Mazin, D. J. Singh, M. D. Johannes, and M. H. Du, Phys. Rev. Lett. **101**, 057003 (2008).

[9] C. Petrovic, P. G. Pagliuso, M. F. Hundley, R. Movshovich, J. L. Sarrao, J. D. Thompson, Z. Fisk, and P. Monthoux, J. Phys.: Condens. Matter **13**, L337 (2001).

[10] Y. Kamihara, H. Hiramatsu, M. Hirano, R. Kawamura, H. Yanagi, T. Kamiya, and H. Hosono, J. Am. Chem. Soc. **128**, 10012 (2006).

[11] H. Shishido, T. Ueda, S. Hashimoto, T. Kubo, R. Settai, H. Harima, and Y. Onuki, J. Phys.: Condens. Matter **15**, 499 (2003).

[12] T. Tayama, A. Harita, T. Sakakibara, Y. Haga, H. Shishido, R. Settai, and Y. Onuki, Phys. Rev. B **65**, 180504 (2002).

[13] V. A. Sidorov, M. Nicklas, P. G. Pagliuso, J. L. Sarrao, Y. Bang, A. V. Balatsky, and J. D. Thompson, Phys. Rev. Lett. **89**, 157004 (2002).

[14] A. Bianchi, R. Movshovich, I. Vekhter, P. G. Pagliuso, and J. L. Sarrao, Phys. Rev. Lett. **91**, 257001 (2003a).

[15] L. D. Pham, T. Park, S. Maquilon, J. D. Thompson, and Z. Fisk, Phys. Rev. Lett. **97**, 56404 (2006).

[16] Y. Kamihara, T. Watanabe, M. Hirano, and H. Hosono, J. Am. Chem. Soc. **130**, 3296 (2008).

[17] E. Moshopoulou, J. Sarrao, P. Pagliuso, N. Moreno, J. Thompson, Z. Fisk, and R. Ibberson, Applied Physics A: Materials Science & Processing **74**, 895 (2002), ISSN 0947-8396.

[18] N. Ashcroft and N. Mermin, *Solid State Physics* (Saunders, Philadelphia, 1976), ISBN 0-03-083993-9.

[19] M. Tinkham, *Introduction to superconductivity* (Dover, New York, 2004), 2nd ed., ISBN 0-486-43503-2.

[20] Š. Kos, I. Martin, and C. M. Varma, Phys. Rev. B **68**, 052507 (2003).

[21] A. Bianchi, R. Movshovich, C. Capan, P. G. Pagliuso, and J. L. Sarrao, Phys. Rev. Lett. **91**, 187004 (2003b).

[22] A. Bianchi, R. Movshovich, N. Oeschler, P. Gegenwart, F. Steglich, J. D. Thompson, P. G. Pagliuso, and J. L. Sarrao, Phys. Rev. Lett. **89**, 137002 (2002).

[23] M. Ichioka and K. Machida, Phys. Rev. B **76**, 064502 (2007).

[24] A. D. Bianchi, M. Kenzelmann, L. DeBeer-Schmitt, J. S. White, E. M. Forgan, J. Mesot, M. Zolliker, J. Kohlbrecher, R. Movshovich, E. Bauer, et al., Science **319**, 177 (2008).

[25] C. Capan, A. Bianchi, R. Movshovich, A. D. Christianson, A. Malinowski, M. F. Hundley, A. Lacerda, P. G. Pagliuso, and J. L. Sarrao, Phys. Rev. B **70**, 134513 (2004).

[26] C. F. Miclea, M. Nicklas, D. Parker, K. Maki, J. L. Sarrao, J. D. Thompson, G. Sparn, and F. Steglich, Phys. Rev. Lett. **96**, 117001 (2006).

[27] V. F. Mitrović, M. Horvatić, C. Berthier, G. Knebel, G. Lapertot, and J. Flouquet, Phys. Rev. Lett. **97**, 117002 (2006).

[28] K. Kumagai, M. Saitoh, T. Oyaizu, Y. Furukawa, S. Takashima, M. Nohara, H. Takagi, and Y. Matsuda, Phys. Rev. Lett. **97**, 227002 (2006).

[29] A. B. Vorontsov, J. A. Sauls, and M. J. Graf, Phys. Rev. B **72**, 184501 (2005).

[30] H. Burkhardt and D. Rainer, Ann. Phys. **506**, 181 (1994).

[31] A. B. Vorontsov, I. Vekhter, and M. J. Graf, Phys. Rev. B **78**, 180505 (2008).

[32] H. Adachi and R. Ikeda, Phys. Rev. B **68**, 184510 (2003).

[33] M. Houzet and V. P. Mineev, Phys. Rev. B **74**, 144522 (2006).

[34] K. Maki and T. Tsuneto, Prog. Theor. Phys. **31**, 945 (1964).

[35] A. M. Clogston, Phys. Rev. Lett. **9**, 266 (1962).

[36] B. S. Chandrasekhar, App. Phys. Lett. **1**, 7 (1962).

[37] P. Fulde and R. A. Ferrell, Phys. Rev. **135**, A550 (1964).

[38] A. I. Larkin and Y. N. Ovchinnikov, Sov. Phys. JETP **20**, 762 (1965).

[39] A. I. Buzdin and H. Kachkachi, Phys. Lett. A **225**, 341 (1997).

[40] C. Mora and R. Combescot, Phys. Rev. B **71**, 214504 (2005).

[41] S. Matsuo, S. Higashitani, Y. Nagato, and K. Nagai, J. Phys. Soc. Jpn. **67**, 280 (1998).

[42] H. Aoki, T. Sakakibara, H. Shishido, R. Settai, Y. Ōnuki, P. Miranović, and K. Machida, Physica B: Phys. Cond. Matt. **359**, 410 (2005).

[43] K. Izawa, H. Yamaguchi, Y. Matsuda, H. Shishido, R. Settai, and Y. Onuki, Phys. Rev. Lett. **87**, 057002 (2001).

[44] R. Movshovich, M. Jaime, J. D. Thompson, C. Petrovic, Z. Fisk, P. G. Pagliuso, and J. L. Sarrao, Phys. Rev. Lett. **86**, 5152 (2001).

[45] K. V. Samokhin, Physica C **274**, 156 (1997).

[46] L. W. Gruenberg and L. Gunther, Phys. Rev. Lett. **16**, 996 (1966).

[47] H. Shimahara, J. Phys. Soc. Jpn. **67**, 736 (1998).

[48] R. Combescot and C. Mora, Euro. Phys. J. B-Cond. Matt. **44**, 189 (2005).

[49] K. Maki and H. Won, Czech. J. of Phys. **46**, 1035 (1996).

[50] Y. Matsuda and H. Shimahara, J. Phys. Soc. Jpn. **76**, 051005 (2007).

[51] K. Yang and S. L. Sondhi, Phys. Rev. B **57**, 8566 (1998).

[52] P. M. Chaikin and T. C. Lubensky, *Principles of condensed matter physics* (Cambridge University Press, New York, 1995).

[53] P. Monthoux, A. V. Balatsky, and D. Pines, Phys. Rev. Lett. **67**, 3448 (1991).

[54] T. Moriya, Y. Takahashi, and K. Ueda, J. Phys. Soc. Jpn. **59**, 2905 (1990).

[55] S. Nakamura, T. Moriya, and K. Ueda, J. Phys. Soc. Jpn. **65**, 4026 (1996).

[56] P. A. Lee, T. M. Rice, and P. W. Anderson, Phys. Rev. Lett. **31**, 462 (1973).

[57] C. Stock, C. Broholm, J. Hudis, H. J. Kang, and C. Petrovic, Phys. Rev. Lett. **100**, 87001 (2008).

[58] M. Nicklas, O. Stockert, T. Park, K. Habicht, K. Kiefer, L. D. Pham, J. D. Thompson, Z. Fisk, and F. Steglich, Phys. Rev. B **76**, 052401 (2007).

[59] W. Bao, P. G. Pagliuso, J. L. Sarrao, J. D. Thompson, Z. Fisk, J. W. Lynn, and R. W. Erwin, Phys. Rev. B **62**, R14621 (2000).

[60] S. Majumdar, G. Balakrishnan, M. R. Lees, D. M. Paul, and G. J. McIntyre, Phys. Rev. B **66**, 212502 (2002).

[61] A. Llobet, J. S. Gardner, E. G. Moshopoulou, J. M. Mignot, M. Nicklas, W. Bao, N. O. Moreno, P. G. Pagliuso, I. N. Goncharenko, J. L. Sarrao, et al., Phys. Rev. B **69**, 024403 (2004).

[62] H. Hegger, C. Petrovic, E. G. Moshopoulou, M. F. Hundley, J. L. Sarrao, Z. Fisk, and J. D. Thompson, Phys. Rev. Lett. **84**, 4986 (2000).

[63] S. Nakatsuji, S. Yeo, L. Balicas, Z. Fisk, P. Schlottmann, P. G. Pagliuso, N. O. Moreno, J. L. Sarrao, and J. D. Thompson, Phys. Rev. Lett. **89**, 106402 (2002).

[64] R. Beaird, A. B. Vorontsov, and I. Vekhter, Physica B **403**, 1083 (2008).

[65] D. J. Singh and M.-H. Du, Phys. Rev. Lett. **100**, 237003 (2008).

[66] M. Rotter, M. Tegel, and D. Johrendt, Phys. Rev. Lett. **101**, 107006 (2008).

[67] X. H. Chen, T. Wu, G. Wu, R. H. Liu, H. Chen, and D. F. Fang, Nature **453**, 761 (2008).

[68] F.-C. Hsu, J.-Y. Luo, K.-W. Yeh, T.-K. Chen, T.-W. Huang, P. M. Wu, Y.-C. Lee, Y.-L. Huang, Y.-Y. Chu, D.-C. Yan, et al., Proc. Natl. Acad. Sci. USA **105**, 14262 (2008).

[69] A. Subedi, L. Zhang, D. J. Singh, and M. H. Du, Phys. Rev. B **78**, 134514 (2008).

[70] J. Paglione and R. Greene, Nature Phys. **6**, 645 (2010), ISSN 1745-2473.

[71] D. Singh, Phys. Rev. B **78**, 94511 (2008).

[72] D. Lu, M. Yi, S. Mo, A. Erickson, J. Analytis, J. Chu, D. Singh, Z. Hussain, T. Geballe, I. Fisher, et al., Nature **455**, 81 (2008).

[73] S. Raghu, X. Qi, C. Liu, D. Scalapino, and S. Zhang, Phys. Rev. B **77**, 220503(R) (2008).

[74] M. M. Korshunov and I. Eremin, Phys. Rev. B **78**, 140509 (2008).

[75] D. Zhang, Phys. Rev. Lett. **103**, 186402 (2009).

[76] K. Kuroki, S. Onari, R. Arita, H. Usui, Y. Tanaka, H. Kontani, and H. Aoki, Phys. Rev. Lett. **101**, 87004 (2008).

[77] S. Graser, T. Maier, P. Hirschfeld, and D. Scalapino, New J. Phys. **11**, 025016 (2009).

[78] T. Kondo, A. F. Santander-Syro, O. Copie, C. Liu, M. E. Tillman, E. D. Mun, J. Schmalian, S. L. Bud'ko, M. A. Tanatar, P. C. Canfield, et al., Phys. Rev. Lett. **101**, 147003 (2008).

[79] H. Ding, P. Richard, K. Nakayama, K. Sugawara, T. Arakane, Y. Sekiba, A. Takayama, S. Souma, T. Sato, T. Takahashi, et al., Europhys. Lett. **83**, 47001 (2008).

[80] S. Sebastian, J. Gillett, N. Harrison, P. Lau, D. Singh, C. Mielke, and G. Lonzarich, Journal of Physics: Condensed Matter **20**, 422203 (2008).

[81] J. G. Analytis, J.-H. Chu, R. D. McDonald, S. C. Riggs, and I. R. Fisher, Phys. Rev. Lett. **105**, 207004 (2010).

[82] H. Shishido, A. F. Bangura, A. I. Coldea, S. Tonegawa, K. Hashimoto, S. Kasahara, P. M. C. Rourke, H. Ikeda, T. Terashima, R. Settai, et al., Phys. Rev. Lett. **104**, 057008 (2010).

[83] P. Goswami, P. Nikolic, and Q. Si, Europhys. Lett. **91**, 37006 (2010).

[84] A. Chubukov, M. Vavilov, and A. Vorontsov, Phys. Rev. B. **80** (2009).

[85] K. Seo, B. A. Bernevig, and J. Hu, Phys. Rev. Lett. **101**, 206404 (2008).

[86] V. Cvetkovic and Z. Tesanovic, Euro. Phys. Lett. **85**, 37002 (2009).

[87] M. Parish, J. Hu, and B. Bernevig, Phys. Rev. B **78**, 144514 (2008).

[88] T. A. Maier, S. Graser, D. J. Scalapino, and P. J. Hirschfeld, Phys. Rev. B **79**, 224510 (2009).

[89] Y. Bang and H.-Y. Choi, Phys. Rev. B **78**, 134523 (2008).

[90] F. Wang, H. Zhai, Y. Ran, A. Vishwanath, and D. Lee, Phys. Rev. Lett. **102**, 47005 (2009).

[91] H. Kontani and S. Onari, Phys. Rev. Lett. **104**, 157001 (2010).

[92] K. Kuroki, H. Usui, S. Onari, R. Arita, and H. Aoki, Phys. Rev. B **79**, 224511 (2009).

[93] Physica C **469**, 614 (2009).

[94] K. Ishida, Y. Nakai, and H. Hosono, J. Phys. Soc. Jpn. **78**, 2001 (2009).

[95] D. C. Johnston, Adv. Phys. **59**, 803 (2010).

[96] L. Zhao, H.-Y. Liu, W.-T. Zhang, J.-Q. Meng, X.-W. Jia, G.-D. Liu, X.-L. Dong, G.-F. Chen, J.-L. Luo, N.-L. Wang, et al., Chin. Phys. Lett. **25**, 4402 (2008).

[97] C. Liu, G. Samolyuk, Y. Lee, N. Ni, T. Kondo, A. Santander-Syro, S. Bud'Ko, J. McChesney, E. Rotenberg, T. Valla, et al., Phys. Rev. Lett. **101**, 177005 (2008).

[98] K. Nakayama, T. Sato, P. Richard, Y. Xu, Y. Sekiba, S. Souma, G. Chen, J. Luo, N. Wang, H. Ding, et al., Europhys. Lett. **85**, 67002 (2009).

[99] R. Khasanov, K. Conder, E. Pomjakushina, A. Amato, C. Baines, Z. Bukowski, J. Karpinski, S. Katrych, H. Klauss, H. Luetkens, et al., Phys. Rev. B **78**, 220510 (2008).

[100] K. Hashimoto, T. Shibauchi, T. Kato, K. Ikada, R. Okazaki, H. Shishido, M. Ishikado, H. Kito, A. Iyo, H. Eisaki, et al., Phys. Rev. Lett. **102**, 017002 (2009a).

[101] K. Hashimoto, T. Shibauchi, S. Kasahara, K. Ikada, S. Tonegawa, T. Kato, R. Okazaki, C. van der Beek, M. Konczykowski, H. Takeya, et al., Phys. Rev. Lett. **102**, 207001 (2009b).

[102] C. Hicks, T. Lippman, M. Huber, J. Analytis, J. Chu, A. Erickson, I. Fisher, and K. Moler, Phys. Rev. Lett. **103** (2009).

[103] L. Malone, J. Fletcher, A. Serafin, A. Carrington, N. Zhigadlo, Z. Bukowski, S. Katrych, and J. Karpinski, Phys. Rev. B **79**, 140501 (2009).

[104] J. Fletcher, A. Serafin, L. Malone, J. Analytis, J. Chu, A. Erickson, I. Fisher, and A. Carrington, Phys. Rev. Lett. **102**, 147001 (2009).

[105] R. T. Gordon, C. Martin, H. Kim, N. Ni, M. A. Tanatar, J. Schmalian, I. I. Mazin, S. L. Bud'ko, P. C. Canfield, and R. Prozorov, Phys. Rev. B **79**, 100506 (2009a).

[106] R. T. Gordon, N. Ni, C. Martin, M. A. Tanatar, M. D. Vannette, H. Kim, G. D. Samolyuk, J. Schmalian, S. Nandi, A. Kreyssig, et al., Phys. Rev. Lett. **102**, 127004 (2009b).

[107] K. Hashimoto, M. Yamashita, S. Kasahara, Y. Senshu, N. Nakata, S. Tonegawa, K. Ikada, A. Serafin, A. Carrington, T. Terashima, et al., Phys. Rev. B **81**, 220501 (2010).

[108] M. Yamashita, N. Nakata, Y. Senshu, S. Tonegawa, K. Ikada, K. Hashimoto, H. Sugawara, T. Shibauchi, and Y. Matsuda, Phys. Rev. B **80**, 220509 (2009).

[109] X. Luo, M. Tanatar, J. Reid, H. Shakeripour, N. Doiron-Leyraud, N. Ni, S. Budko, P. Canfield, H. Luo, Z. Wang, et al., Phys. Rev. B **80**, 140503 (2009).

[110] M. A. Tanatar, J.-P. Reid, H. Shakeripour, X. G. Luo, N. Doiron-Leyraud, N. Ni, S. L. Bud'ko, P. C. Canfield, R. Prozorov, and L. Taillefer, Phys. Rev. Lett. **104**, 067002 (2010).

[111] H.-J. Grafe, D. Paar, G. Lang, N. J. Curro, G. Behr, J. Werner, J. Hamann-Borrero, C. Hess, N. Leps, R. Klingeler, et al., Phys. Rev. Lett. **101**, 047003 (2008).

[112] K. Ahilan, F. L. Ning, T. Imai, A. S. Sefat, R. Jin, M. A. McGuire, B. C. Sales, and D. Mandrus, Phys. Rev. B **78**, 100501 (2008).

[113] M. Yashima, H. Nishimura, H. Mukuda, Y. Kitaoka, K. Miyazawa, M. Parasharam, K. Kihou, K. Hijiri, H. Eisaki, and I. Akira, J. Phys. Soc. Jpn. **78**, 103702 (2009).

[114] V. Mishra, G. Boyd, S. Graser, T. Maier, P. Hirschfeld, and D. Scalapino, Phys. Rev. B **79**, 94512 (2009a).

[115] V. Mishra, A. Vorontsov, P. J. Hirschfeld, and I. Vekhter, Phys. Rev. B **80**, 224525 (2009b).

[116] S. Graser, G. R. Boyd, C. Cao, H.-P. Cheng, P. J. Hirschfeld, and D. J. Scalapino, Phys. Rev. B **77**, 180514 (2008).

[117] T. A. Maier and D. J. Scalapino, Phys. Rev. B **78**, 020514 (2008).

[118] V. Stanev, J. Kang, and Z. Tesanovic, Phys. Rev. B **78**, 184509 (2008).

[119] Y. Senga and H. Kontani, J. Phys. Soc. Jpn. **77**, 3710 (2008).

[120] A. B. Vorontsov, M. G. Vavilov, and A. V. Chubukov, Phys. Rev. B **79**, 140507 (2009).

[121] W. Tsai, Y. Zhang, C. Fang, and J. Hu, Phys. Rev. B **80**, 064513 (2009).

[122] Y. Senga and H. Kontani, New J. Phys. **11**, 035005 (2009).

[123] M. Matsumoto, M. Koga, and H. Kusunose, J. Phys. Soc. Jpn. **78**, 084718 (2009).

[124] A. Akbari, I. Eremin, and P. Thalmeier, Phys. Rev. B **81**, 014524 (2010).

[125] A. Balatsky, I. Vekhter, and J.-X. Zhu, Rev. Mod. Phys. **78**, 373 (2006).

[126] J. M. Byers, M. E. Flatté, and D. J. Scalapino, Phys. Rev. Lett. **71**, 3363 (1993).

[127] A. Balatsky, M. Salkola, and A. Rosengren, Phys. Rev. B **51**, 15547 (1995).

[128] S. Pan, E. Hudson, K. Lang, H. Eisaki, S. Uchida, and J. Davis, Nature **403**, 747 (2000).

[129] E. Hudson, K. Lang, V. Madhavan, S. Pan, H. Eisaki, S. Uchida, and J. Davis, Nature **411**, 921 (2001).

[130] M. Salkola, A. Balatsky, and D. Scalapino, Phys. Rev. Lett. **77**, 1841 (1996).

[131] T. Zhou, X. Hu, J.-X. Zhu, and C. S. Ting, arXiv:0904.4273 (unpublished).

[132] T. Ng and Y. Avishai, Phys. Rev. B **80**, 104504 (2009).

[133] T. Kariyado and M. Ogata, J. Phys. Soc. Jpn. **79**, 083704 (2010).

[134] J. Zhu, R. Yu, A. Balatsky, and Q. Si, arXiv:1103.3509 (unpublished).

[135] O. V. Dolgov, I. I. Mazin, D. Parker, and A. A. Golubov, Phys. Rev. B **79**, 060502 (2009).

[136] H. Ding, K. Nakayama, P. Richard, S. Souma, T. Sato, T. Takahashi, M. Neupane, Y. Xu, Z. Pan, A. Federov, et al., arXiv:0812.0534 (unpublished).

[137] A. Coldea, J. Fletcher, A. Carrington, J. Analytis, A. Bangura, J. Chu, A. Erickson, I. Fisher, N. Hussey, and R. McDonald, Phys. Rev. Lett. **101**, 216402 (2008).

[138] H. Muranaka, D. Yusuke, K. Katayama, H. Sugawara, R. Settai, F. Honda, T. Matsuda, H. Yoshinori, H. Yamagami, and Y. Onuki, J. Phys. Soc. Jpn. **78**, 053705 (2009).

[139] A. F. Kemper, C. Cao, P. J. Hirschfeld, and H. P. Cheng, Phys. Rev. B **80**, 104511 (2009).

[140] K. Gofryk, A. B. Vorontsov, I. Vekhter, A. S. Sefat, T. Imai, E. D. Bauer, J. D. Thompson, and F. Ronning, Phys. Rev. B **83**, 064513 (2011).

[141] D.-J. Jang, A. B. Vorontsov, I. Vekhter, K. Gofryk, Z. Yang, S. Ju, J. B. Hong, J. H. Han, Y. S. Kwon, F. Ronning, et al., New Journal of Physics **13**, 023036 (2011).

[142] R. Fehrenbacher, Phys. Rev. Lett. **77**, 1849 (1996).

[143] R. Fehrenbacher, Phys. Rev. B **54**, 6632 (1996).

[144] Y. Ohashi, Physica C: Superconductivity **412**, 41 (2004).

[145] A. A. Golubov and I. I. Mazin, Phys. Rev. B **55**, 15146 (1997).

[146] G. Xu, W. Ming, Y. Yao, X. Dai, S. Zhang, and Z. Fang, EPL (Europhysics Letters) **82**, 67002 (2008).

[147] J. Kim, P. Hirschfeld, G. Stewart, S. Kasahara, T. Shibauchi, T. Terashima, and Y. Matsuda, Phys. Rev. B **81**, 214507 (2010).

[148] I. Gradshteyn and I. Ryzhik, *Tables of integrals, series, and products* (Academic Press, 2000), 6th ed.

[149] M. Abramowitz and I. A. Stegun, *Handbook of Mathematical Functions with Formulas, Graphs, and Mathematical Tables* (Dover, New York, 1964), ninth dover printing, tenth gpo printing ed.

Appendix A: Derivation of Landau Expansion in Powers of the Order Parameter

To derive the coefficients for the Landau free energy functional, I begin with the partition function

$$\mathcal{Z} = \mathrm{Tr}(e^{-\beta\mathcal{H}}) \tag{A.1}$$

where $\mathcal{H}$ is the mean-field hamiltonian in Eq. (3.3), $\beta = T^{-1}$ and the trace is taken over all eigenstates of $\mathcal{H}$. I require that the free energy $\mathcal{F} = -T\ln(\mathcal{Z})$ is an extremum with respect to $\Delta_{\mathbf{q}}$ and $\Delta^*_{\mathbf{q}}$, so that

$$\delta\mathcal{F} = \sum_{\mathbf{q}} \left(\frac{\Delta^*_{\mathbf{q}}}{|\lambda|} + \sum_{\mathbf{k}} \mathcal{Y}(\hat{\mathbf{k}}) \left\langle c^\dagger_{-\mathbf{k}\downarrow} c^\dagger_{\mathbf{k}+\mathbf{q}\uparrow} \right\rangle \right) \delta\Delta_{\mathbf{q}} + h.c. = 0\,, \tag{A.2}$$

where $h.c.$ stands for the Hermitian conjugate. Since $\delta\mathcal{F} = 0$ and $\delta\Delta_{\mathbf{q}}$ can take any value, it follows that $\mathcal{F}$ is an extremum when $\Delta^*_{\mathbf{q}}$ satisfies the self consistency condition

$$\Delta^*_{\mathbf{q}} = -|\lambda| \sum_{\mathbf{k}} \mathcal{Y}(\hat{\mathbf{k}}) \left\langle c^\dagger_{-\mathbf{k}\downarrow} c^\dagger_{\mathbf{k}+\mathbf{q}\uparrow} \right\rangle \tag{A.3}$$

I construct the Landau free energy functional by expanding in powers of $\Delta_{\mathbf{q}}$, but not in the modulation wave vector $\mathbf{q}$, which allows me to treat the low temperature region. To carry out this expansion I use the Gor'kov formulation of the Green's function approach. The normal,

$$G_\sigma(\mathbf{k},\mathbf{k}';\tau) = -\left\langle T_\tau \left(c_{\mathbf{k}\sigma}(\tau) c^\dagger_{\mathbf{k}'\sigma}(0) \right) \right\rangle, \tag{A.4}$$

and anomalous,

$$F^\dagger(\mathbf{k},\mathbf{k}';\tau) = -\left\langle T_\tau \left(c^\dagger_{\mathbf{k}\downarrow}(\tau) c^\dagger_{\mathbf{k}'\uparrow}(0) \right) \right\rangle, \tag{A.5}$$

Green's function satisfy the equations of motion

$$\left(-\frac{\partial}{\partial\tau} - \epsilon_{\mathbf{k}\uparrow} \right) G_\uparrow(\mathbf{k},\mathbf{k}';\tau) + \sum_{\mathbf{q}} \mathcal{Y}(\hat{\mathbf{k}}) \Delta_{\mathbf{q}} F^\dagger(-\mathbf{k}+\mathbf{q},\mathbf{k}';\tau) = \delta_{\mathbf{k},\mathbf{k}'}\delta(\tau)\,, \tag{A.6}$$

$$\left(-\frac{\partial}{\partial\tau} + \epsilon_{-\mathbf{k}\downarrow} \right) F^\dagger(-\mathbf{k},\mathbf{k}';\tau) + \sum_{\mathbf{q}} \mathcal{Y}(\hat{\mathbf{k}}) \Delta^*_{\mathbf{q}} G_\uparrow(\mathbf{k}+\mathbf{q},\mathbf{k}';\tau) = 0\,, \tag{A.7}$$

respectively. Here T_τ denotes imaginary time ordering and $\sigma =\uparrow$ ($\sigma =\downarrow$) indicates the orientation of the electron spin is parallel (antiparallel) to the applied field $\mathbf{B}$. The equations of motion in Eqs. (A.6) and (A.7) are found by using

$$\frac{\partial A(\tau)}{\partial \tau} = [\mathcal{H}, A(\tau)] \,, \tag{A.8}$$

where the square brackets denote the commutator between the Hamiltonian $\mathcal{H}$ and the operator $A(\tau) = c_{\mathbf{k}\sigma}(\tau), c^\dagger_{\mathbf{k}\sigma}(\tau)$ [148].

A Fourier transformation of Eqs. (A.6)-(A.6) into the Matsubara frequency space yields

$$(i\omega_n - \epsilon_{\mathbf{k}\uparrow})G_\uparrow(\mathbf{k},\mathbf{k}';i\omega_n) + \sum_{\mathbf{q}} \mathcal{Y}(\hat{\mathbf{k}})\Delta_{\mathbf{q}} F^\dagger(-\mathbf{k}+\mathbf{q},\mathbf{k}';i\omega_n) = \delta_{\mathbf{k},\mathbf{k}'} \,, \tag{A.9}$$

$$(i\omega_n + \epsilon_{-\mathbf{k}\downarrow})F^\dagger(-\mathbf{k},\mathbf{k}';i\omega_n) + \sum_{\mathbf{q}} \mathcal{Y}(\hat{\mathbf{k}})\Delta^*_{\mathbf{q}} G_\uparrow(\mathbf{k}+\mathbf{q},\mathbf{k}';i\omega_n) = 0 \,, \tag{A.10}$$

where $\omega_n = 2\pi T\left(n+\frac{1}{2}\right)$ is the fermionic Matsubara frequency. The thermal average entering the free energy variation, Eq. (A.2), is given in terms of the Matsubara sum

$$\left\langle c^\dagger_{-\mathbf{k}\downarrow} c^\dagger_{\mathbf{k}+\mathbf{q}\uparrow} \right\rangle = -T\sum_n F^\dagger(-\mathbf{k},\mathbf{k}+\mathbf{q};i\omega_n) \,, \tag{A.11}$$

where $F^\dagger(-\mathbf{k},\mathbf{k}+\mathbf{q};i\omega_n)$ is found by solving Eqs. (A.9) and (A.10). Thus, in terms of $F^\dagger$, Eq. (A.2) is

$$\delta\mathcal{F} = \sum_{\mathbf{q}} \left(\frac{\Delta^*_{\mathbf{q}}}{|\lambda|} - T\sum_{\mathbf{k},n} \mathcal{Y}(\hat{\mathbf{k}}) F^\dagger(-\mathbf{k},\mathbf{k}+\mathbf{q};i\omega_n) \right) \delta\Delta_{\mathbf{q}} + h.c. = 0 \,. \tag{A.12}$$

I iteratively expand Eqs. (A.9) and (A.10) in powers of $\Delta_{\mathbf{q}}$ and $\Delta^*_{\mathbf{q}}$, and hence find the series expansion for $F^\dagger(-\mathbf{k},\mathbf{k}';i\omega_n)$. Using this expansion for the thermal average in Eq. (A.12), I integrate term by term with respect to $\Delta_{\mathbf{q}}$, and I obtain the Landau free energy density, $F_L = \mathcal{F}/L^2$ where L^2 is the 2D system size, up to $\mathcal{O}(|\Delta_0|^6)$ inclusive. I find

$$\begin{aligned} F_L = &\sum_{\{\mathbf{q}_i\}} \widetilde{\alpha}_{\mathbf{q}_i} |\Delta_{\mathbf{q}_i}|^2 + \sum_{\{\mathbf{q}_i\}} \widetilde{\gamma}_{\mathbf{q}_1,\ldots,\mathbf{q}_4} \Delta_{\mathbf{q}_1}\Delta^*_{\mathbf{q}_2}\Delta_{\mathbf{q}_3}\Delta^*_{\mathbf{q}_4} \delta_{\mathbf{q}_1+\mathbf{q}_3,\mathbf{q}_2+\mathbf{q}_4} \\ &+ \sum_{\{\mathbf{q}_i\}} \widetilde{\nu}_{\mathbf{q}_1,\ldots,\mathbf{q}_6} \Delta_{\mathbf{q}_1}\Delta^*_{\mathbf{q}_2}\Delta_{\mathbf{q}_3}\Delta^*_{\mathbf{q}_4}\Delta_{\mathbf{q}_5}\Delta^*_{\mathbf{q}_6} \delta_{\mathbf{q}_1+\mathbf{q}_3+\mathbf{q}_5,\mathbf{q}_2+\mathbf{q}_4+\mathbf{q}_6} \end{aligned} \tag{A.13}$$

where the summation over $\{\mathbf{q}_i\}$ includes all possible combinations of the allowed Fourier components of $\Delta(\mathbf{r})$.

The fully $\mathbf{q}$-dependent coefficients of the Ginzburg-Landau expansion are given by

$$\widetilde{\alpha}_{\mathbf{q}} = \frac{1}{|\lambda|} - T\sum_{n,\mathbf{k}} |\mathcal{Y}(\hat{\mathbf{k}})|^2 G^0_\uparrow(\mathbf{k}+\mathbf{q}; i\omega_n) G^0_\downarrow(-\mathbf{k}; -i\omega_n), \tag{A.14}$$

$$\begin{aligned}\widetilde{\gamma}_{\mathbf{q}_1,\ldots,\mathbf{q}_4} = \frac{T}{2}\sum_{n,\mathbf{k}} |\mathcal{Y}(\hat{\mathbf{k}})|^4 G^0_\uparrow(\mathbf{k}+\mathbf{q}_1; i\omega_n) G^0_\downarrow(-\mathbf{k}+\mathbf{q}_3-\mathbf{q}_2; -i\omega_n) \\ \times G^0_\uparrow(\mathbf{k}+\mathbf{q}_2; i\omega_n) G^0_\downarrow(-\mathbf{k}; -i\omega_n),\end{aligned} \tag{A.15}$$

$$\begin{aligned}\widetilde{\nu}_{\mathbf{q}_1,\ldots,\mathbf{q}_6} = -\frac{T}{3}\sum_{n,\mathbf{k}} |\mathcal{Y}(\hat{\mathbf{k}})|^6 G^0_\uparrow(\mathbf{k}+\mathbf{q}_1; i\omega_n) G^0_\downarrow(-\mathbf{k}+\mathbf{q}_3+\mathbf{q}_5-\mathbf{q}_2-\mathbf{q}_4; -i\omega_n) \\ \times G^0_\uparrow(\mathbf{k}+\mathbf{q}_2+\mathbf{q}_4-\mathbf{q}_3; i\omega_n) G^0_\downarrow(-\mathbf{k}+\mathbf{q}_3-\mathbf{q}_2; -i\omega_n) \\ \times G^0_\uparrow(\mathbf{k}+\mathbf{q}_2; i\omega_n) G^0_\downarrow(-\mathbf{k}; -i\omega_n),\end{aligned} \tag{A.16}$$

where

$$G^0_\sigma(\mathbf{k}; i\omega_n) = \frac{1}{i\omega_n - \epsilon_{\mathbf{k}\sigma}} \tag{A.17}$$

is the normal state propagator for an electron of spin σ in a Zeeman field.

All the momentum sums are evaluated using the fact the the Green's functions are peaked at the Fermi energy, so that, for my model of a 2D circular Fermi surface

$$\sum_{\mathbf{k}} g(\mathbf{k}) = N_F \int_0^{2\pi} \frac{d\theta}{2\pi} \int_{-\omega_c}^{\omega_c} d\epsilon\, g(\epsilon, \theta)\,. \tag{A.18}$$

where N_F is the density of states at the Fermi energy and $g(\mathbf{k})$ is whatever function is to be integrated over $\mathbf{k}$. Given that the pairing interaction $|\lambda|$ is assumed to be finite only over an energy band of width $2\omega_c$ that is centered at the Fermi surface, I formally take the integration limits on ϵ to be $\pm\omega_c$. Whenever the integrand dies out faster than $1/\varepsilon^2$, I can safely extend the ϵ integration limits out to infinity. Assuming a circular Fermi surface, I use 2D angular basis functions

$$\mathcal{Y}(\hat{\mathbf{k}}) = \begin{cases} 1 & s-\text{wave} \\ \sqrt{2}\left(\hat{k}_x^2 - \hat{k}_y^2\right) = \sqrt{2}\cos(2\theta) & d_{x^2-y^2}, \end{cases} \tag{A.19}$$

normalized so that $\langle|\mathcal{Y}(\theta)|^2\rangle_{FS} = 1$ where θ is the azimuthal angle in momentum space. Here $\langle\cdots\rangle_{FS}$ indicates the angular average over the 2D Fermi surface.

Since I cannot obtain a closed-form expression for **k**-integrated Landau coefficients, I compute the integral over ϵ analytically and leave the integral over θ to be evaluated numerically. Thus, I obtain the Landau coefficients $\widetilde{\gamma}_{\mathbf{q}}$ and $\widetilde{\nu}_{\mathbf{q}}$ that I show in Section 3.3. To obtain the expression for $\widetilde{\alpha}_{\mathbf{q}}$, I use the self consistency condition in Eq. (A.3) to eliminate the interaction strength $|\lambda|$ in favor of the zero-field transition temperature T_{c0} in the standard manner that I describe below.

A.1 The Critical Temperature in Zero Magnetic Field

Using Eqs. (A.9) and (A.10), and the fact that the superconducting order parameter is real and uniform ($\Delta_{\mathbf{q}} = \Delta^*_{\mathbf{q}} = \Delta_0\delta_{\mathbf{q},0}$) at **B**=0, I arrive at the zero-field self consistency equation

$$\begin{aligned}\frac{1}{|\lambda|} &= T\sum_{\mathbf{k},n}\mathcal{Y}(\hat{\mathbf{k}})^2\left[\frac{1}{\left[G^0_\downarrow(-\mathbf{k};-i\omega_n)\right]^{-1}\left[G^0_\uparrow(\mathbf{k};i\omega_n)\right]^{-1}+\Delta_0^2\mathcal{Y}(\hat{\mathbf{k}})^2}\right]_{\mathbf{B}=0}\\ &= T\sum_{\mathbf{k},n}\mathcal{Y}(\hat{\mathbf{k}})^2\frac{1}{\omega_n^2+\epsilon_{\mathbf{k}}^2+\Delta_0^2\mathcal{Y}(\hat{\mathbf{k}})^2}\,.\end{aligned} \tag{A.20}$$

where the last line follows from the fact that the two spin species are degenerate in the absence of the Zeeman field and the assumption of quadratic dispersion wherein $\epsilon_{\mathbf{k}\uparrow} = \epsilon_{-\mathbf{k}\downarrow} = \epsilon_{\mathbf{k}}$. The transition at T_{c0} is second order, hence I set $\Delta_0 = 0$ and $T = T_{c0}$ in Eq. (A.20) and then compute the Matsubara sum over n to obtain

$$\begin{aligned}\frac{1}{|\lambda|} &= \frac{N_F}{2}\int_0^{2\pi}\frac{d\theta}{2\pi}\mathcal{Y}(\theta)^2\int_{-x_c}^{x_c}\frac{dx}{x}\tanh\left(\frac{\pi x}{2}\right)\\ &= N_F\int_0^{x_c}\frac{dx}{x}\tanh\left(\frac{\pi x}{2}\right)\,,\end{aligned} \tag{A.21}$$

where $x = \epsilon/\pi T$ and $x_c = \epsilon/\pi T_{c0}$. Note that here the angular dependence of the gap is irrelevant due to the normalization of the $\mathcal{Y}(\theta)$. The last line of Eq. (A.21) is evaluated

using integration by parts, under the assumption that $\omega_c \gg T_{c0}$, whence

$$\frac{1}{|\lambda|} = N_F \ln\left(\frac{2e^{\gamma_E}}{\pi}\frac{\omega_c}{T_{c0}}\right), \tag{A.22}$$

where $\gamma_E \approx 0.577$ is the Euler-Mascheroni constant. It follows immediately that

$$T_{c0} = \frac{2e^{\gamma_E}}{\pi}\omega_c e^{-1/(|\lambda|N_F)}. \tag{A.23}$$

I can rewrite $\widetilde{\alpha}_{\mathbf{q}}$ by using Eq. (A.22) to eliminate $|\lambda|$ and then inserting the term

$$0 = T\sum_{\mathbf{k},n}\mathcal{Y}(\hat{\mathbf{k}})^2\frac{1}{\omega_n^2+\epsilon_{\mathbf{k}}^2} - N_F\ln\left(\frac{2e^{\gamma_E}}{\pi}\frac{\omega_c}{T}\right), \tag{A.24}$$

so that, by combining the logarithms and collecting the $\mathbf{k}$ sums, I obtain

$$\widetilde{\alpha}_{\mathbf{q}} = N_F\ln\left(\frac{T}{T_{c0}}\right) + T\sum_{n,\mathbf{k}}|\mathcal{Y}(\hat{\mathbf{k}})|^2\left[\frac{1}{\omega_n^2+\epsilon_{\mathbf{k}}^2} - G_\uparrow^0(\mathbf{k}+\mathbf{q};i\omega_n)G_\downarrow^0(-\mathbf{k};-i\omega_n)\right]. \tag{A.25}$$

This expression is then used to determine the quadratic Landau coefficients $\alpha_i = N_F^{-1}\sum_{\mathbf{q}}\widetilde{\alpha}_{\mathbf{q}}$, where $i = (u, FF, LO)$, that I present in Chapter 3.3.

A.2 Superconducting Gap at Zero Temperature and Field

I can similarly find $\Delta_0 = \Delta_{00}$, the superconducting gap at zero temperature and field by integrating the zero-field self consistency equation in Eq. (A.20) in the limit $T \to 0$. In this limit, the Matsubara sum in Eq. (A.26) becomes an integral so that

$$\begin{aligned}\frac{1}{|\lambda|} &= \lim_{T\to 0}\left(T\sum_{\mathbf{k},n}\mathcal{Y}(\hat{\mathbf{k}})^2\frac{1}{\omega_n^2+\epsilon_{\mathbf{k}}^2+\Delta_{00}^2\mathcal{Y}(\hat{\mathbf{k}})^2}\right)\\ &= \sum_{\mathbf{k}}\mathcal{Y}(\hat{\mathbf{k}})^2\int_{-\infty}^{\infty}d\omega\frac{1}{\omega^2+\epsilon_{\mathbf{k}}^2+\Delta_{00}^2\mathcal{Y}(\hat{\mathbf{k}})^2}\\ &= \frac{N_F}{2}\int_0^{2\pi}\frac{d\theta}{2\pi}\mathcal{Y}(\theta)^2\int_{-\omega_c}^{\omega_c}d\epsilon\frac{1}{\sqrt{\epsilon_{\mathbf{k}}^2+\Delta_{00}^2\mathcal{Y}(\theta)^2}}.\end{aligned} \tag{A.26}$$

For s-wave superconductivity I use $\mathcal{Y}(\theta) = 1$ and obtain $\Delta_{00} = \Delta_{s0}$ through the integral

$$\begin{aligned}\frac{1}{|\lambda|} &= \frac{N_F}{2}\int_{-\omega_c}^{\omega_c}d\epsilon\frac{1}{\sqrt{\epsilon_{\mathbf{k}}^2+\Delta_{s0}^2}}\\ &= N_F\ln\left(\frac{2\omega_c}{\Delta_{s0}}\right)\end{aligned} \tag{A.27}$$

where the last line follows from the fact that $\omega_c \gg \Delta_{s0}$. The d-wave gap at zero field is $\Delta_{d0}\mathcal{Y}(\theta) = \Delta_{d0}\sqrt{2}\cos(2\theta)$, so that

$$\begin{aligned}\frac{1}{|\lambda|} &= \frac{N_F}{2}\int_0^{2\pi}\frac{d\theta}{2\pi}\int_{-\omega_c}^{\omega_c} d\epsilon \frac{2\cos(2\theta)^2}{\sqrt{\epsilon_{\mathbf{k}}^2 + 2\Delta_{d0}^2\cos(2\theta)^2}} \\ &= \frac{N_F}{2}\int_0^{2\pi}\frac{d\theta}{2\pi} 4\cos(2\theta)^2 \sinh^{-1}\left(\frac{\omega_c/\Delta_{d0}}{\sqrt{1+\cos(4\theta)}}\right) \\ &= \frac{N_F}{2}\left(\ln\left(\frac{8\omega_c^2}{\Delta_{d0}^2}\right) - 1\right),\end{aligned} \tag{A.28}$$

assuming that $\omega_c \gg \Delta_{d0}$. Solving these two equations, I obtain $\Delta_{s0} = 2\omega_c e^{-1/(|\lambda|N_F)}$ and $\Delta_{d0} = \sqrt{8}\omega_c e^{-1/2} e^{-1/(|\lambda|N_F)}$ so that

$$\frac{\Delta_{s0}}{T_{c0}} = \pi e^{-\gamma_E} \approx 1.76 \tag{A.29a}$$

$$\frac{\Delta_{d0}}{T_{c0}} = \sqrt{2}\pi e^{-1/2} e^{-\gamma_E} \approx 1.51\,. \tag{A.29b}$$

Appendix B: Tridiagonal Integration of Gaussian Fluctuations

For the case of single-mode $\cos(\mathbf{Q}\cdot\mathbf{r})$ modulation of the order parameter, the magnetic contribution to the free energy functional (due to the off-diagonal $\mathbf{k}, \mathbf{k}\pm 2\mathbf{Q}$ coupling) takes the tridiagonal form

$$\mathcal{F}(\mathbf{M}(\mathbf{r})) = T\sum_{\mathbf{k}} \left(a_{\mathbf{k}}\mathbf{M}_{\mathbf{k}}\cdot\mathbf{M}^*_{\mathbf{k}} + b_{\mathbf{k}}\mathbf{M}_{\mathbf{k}}\cdot\left(\mathbf{M}^*_{\mathbf{k}+2\mathbf{Q}} + \mathbf{M}^*_{\mathbf{k}-2\mathbf{Q}}\right)\right) , \tag{B.1}$$

where

$$a_{\mathbf{k}} = a \equiv \frac{1}{2T}\left(\frac{1}{\chi} + \frac{1}{2}\eta|\Delta_0|^2\right), \quad \forall\mathbf{k} \tag{B.2}$$

and

$$b_{\mathbf{k}} = b \equiv -\frac{1}{8T}\eta|\Delta_0|^2, \quad \forall\mathbf{k}. \tag{B.3}$$

This yields the partition sum

$$\begin{aligned}\mathcal{Z} &= \prod_{\mathbf{k}}\int \mathcal{D}(\mathbf{M}_{\mathbf{k}})\exp\left[-\left(a|\mathbf{M}_{\mathbf{k}}|^2 + b\mathbf{M}_{\mathbf{k}}\cdot\left(\mathbf{M}^*_{\mathbf{k}+2\mathbf{Q}} + \mathbf{M}^*_{\mathbf{k}-2\mathbf{Q}}\right)\right)\right] \\ &= \prod_{i=1}^{d}\prod_{\mathbf{k}}\int \mathcal{D}(M_{\mathbf{k},i})\exp\left[-\left(a|M_{\mathbf{k},i}|^2 + bM_{\mathbf{k},i}\left(M^*_{\mathbf{k}+2\mathbf{Q},i} + M^*_{\mathbf{k}-2\mathbf{Q},i}\right)\right)\right] ,\end{aligned} \tag{B.4}$$

where the product over i accounts for the d spatial components of $\mathbf{M}(\mathbf{r})$. To compute this integral, I separate the product over all wave vectors into a product over components parallel and perpendicular to the direction of $\mathbf{Q}$. As the terms comprising $\mathcal{Z}$ have no functional dependence on i, I have $\mathcal{Z} = \mathcal{Z}_0^d$ where

$$\begin{aligned}\mathcal{Z}_0 = \prod_{k_\perp}\prod_{k_\parallel}\int \mathcal{D}(M_{k_\perp,k_\parallel})\exp\left[-a|M_{k_\perp,k_\parallel}|^2\right] \\ \times\exp\left[bM_{k_\perp,k_\parallel}\left(M^*_{k_\perp,k_\parallel+2Q} + M^*_{k_\perp,k_\parallel-2Q}\right)\right] .\end{aligned} \tag{B.5}$$

Due to the coupling between $M_{k_\perp,k_\parallel}$ and $M_{k_\perp,k_\parallel\pm 2Q}$, the product over $k_\parallel$ can be divided up into a product of integrals taken only over wave vectors $|k_\parallel| \le |Q|$, effectively employing

the Brillouin zone method of solid state physics with $|k_\parallel| \leq |Q|$ corresponding to the first Brillouin zone. Each term in the product over $|k_\parallel| \leq |Q|$ is then an integral connecting $k_\parallel$ to $k_n = k_\parallel + n(2Q)$, where n is an integer. The sum over k is cut off at a wave vector on the order of the inverse lattice spacing $k_c = \pi/l$. So, to cut off the sum over n, I define the cut off integer n_c such that $k_{\pm n_c} = k_\parallel \pm n_c(2Q) \approx k_c$.

Separating the product over $k_\parallel$ in this way, and introducing the notational shorthand

$$M_n(k_\perp, k_\parallel) = M_{k_\perp, k_\parallel + n(2Q)} \,,$$

my partition sum can be rewritten

$$\begin{aligned} \mathcal{Z}_0 = \prod_{k_\perp} \prod_{k_\parallel = -Q}^{Q} \int \left[\cdots \mathcal{D}(M_1)\mathcal{D}(M_{-1})\mathcal{D}(M_0) \right] \\ \times \exp\left[-a|M_0|^2 - bM_0\left(M_1^* + M_{-1}^*\right) - \cdots \right]. \end{aligned} \tag{B.6}$$

I integrate over the real and imaginary parts of $M_n = M_n' + iM_n''$ and restrict the product over $\mathbf{k}$ to be over one-half of k-space because $M_{\mathbf{k}} = M_{-\mathbf{k}}^*$ for real $\mathbf{M}(\mathbf{r})$. However, as the integrand factors into two identical integrals over M_n' and M_n'', I can integrate over M_n' alone and take the product over all values of $\mathbf{k}$. Thus

$$\begin{aligned} \mathcal{Z}_0 = \prod_{k_\perp} \prod_{k_\parallel = -Q}^{Q} \int \left[\cdots \mathcal{D}(M_1')\mathcal{D}(M_{-1}')\mathcal{D}(M_0') \right] \\ \times \exp\left[-a(M_0')^2 - 2bM_0'\left(M_1' + M_{-1}'\right) - \cdots \right]. \end{aligned} \tag{B.7}$$

Beginning with $n = 0$, I integrate recursively over all M_n' and denote by a_n and b_n the renormalized coefficients of $(M_{\pm n}')^2$ and $M_n' M_{-n}'$, respectively. Working with a and b given in Eqs. (B.2) and (B.3), the integration coefficients are

$$a_0 = a \;\text{ and }\; b_0 = b \;\text{ for }\; n = 0, \tag{B.8}$$

$$a_1 = a_0 - \frac{b_0^2}{a_0} \;\text{ and }\; b_1 = \frac{b_0^2}{a_0} \;\text{ for }\; n = 1, \tag{B.9}$$

and, for $n \geq 1$, the remaining terms

$$a_{n+1} = a_0 - \frac{a_n b_0^2}{a_n^2 - b_n^2} \;\text{ and }\; b_{n+1} = \frac{b_n b_0^2}{a_n^2 - b_n^2} \tag{B.10}$$

are determined recursively. The partition sum becomes

$$\begin{aligned}\mathcal{Z}_0 &= \prod_{k_\perp,k_\parallel} \sqrt{\frac{\pi}{a_0}}\sqrt{\frac{\pi^2}{a_1^2-b_1^2}}\sqrt{\frac{\pi^2}{a_2^2-b_2^2}}\times\cdots\times\sqrt{\frac{\pi^2}{a_{n_c}^2-b_{n_c}^2}} \\ &= \prod_{k_\perp,k_\parallel}\left(\sqrt{\frac{\pi}{a_0}}\right)^{2n_c+1}\sqrt{\frac{a_0^2}{a_1^2-b_1^2}}\sqrt{\frac{a_0^2}{a_2^2-b_2^2}}\times\cdots\quad,\end{aligned} \tag{B.11}$$

where $k_\parallel \in (-Q, Q)$ is understood. The free energy functional $\mathcal{F}(\mathbf{M}(\mathbf{r}))$ can now be replaced with its thermodynamic average $\mathcal{F} = -\beta^{-1}\ln(\mathcal{Z})$ which is

$$\mathcal{F} = \frac{d}{2\beta}\left[\sum_{|\mathbf{k}|=0}^{k_c}\ln\left(\frac{a_0}{\pi}\right) + \sum_{\substack{k_\perp,k_\parallel \\ n}}{}'\ln\left(\frac{a_n^2-b_n^2}{a_0^2}\right)\right], \tag{B.12}$$

where for the second sum $n \in (-n_c, n_c)$. The prime implies that $n = 0$ is excluded from the sum since the $n = 0$ term is $\ln(1) = 0$.

In order to obtain the necessary small Δ expansion of Eq. (B.12), I need to expand $(a_n^2 - b_n^2)/a_0^2$ to $\mathcal{O}(|\Delta_0|^6)$ inclusive. I do this by introducing recursion relations

$$\begin{aligned}s_n &= a_n + b_n = a_0 - \frac{b_0^2}{s_n}, \quad n > 1 \\ d_n &= a_n - b_n = a_0 - \frac{b_0^2}{d_n}, \quad n > 1\end{aligned} \tag{B.13}$$

with the initial values $s_1 = a_0$ and $d_1 = a_0 - 2b_0^2/a_0$, respectively. Taking $a_0 = a$ and $b_0 = b$ from Eqs. (B.2) and (B.3), I expand $s_n d_n/a_0^2 = (a_n^2 - b_n^2)/a_0^2$ to third order in b since $b \propto |\Delta_0|^2$. Expressing a and b in units of $1/2\chi T$, I have the initial values

$$\begin{aligned}s_1 &= a = 1 - 2b \\ d_1 &= a - \frac{2b^2}{1-2b} = 1 - 2b - 2b^2 - 4b^3 + \mathcal{O}(b^4),\end{aligned} \tag{B.14}$$

and the remaining terms for $n > 1$

$$s_n = d_n = 1 - 2b - b^2 - 2b^3 + \mathcal{O}(b^4). \tag{B.15}$$

With these expressions, I find that $s_n d_n = 1 - 4b + 2b^2$ is independent of n when expanded to third order in b. Thus,

$$\frac{s_n d_n}{a_0^2} = \frac{1-4b+2b^2}{(1-2b)^2} = 1 - 2b^2 - 8b^3 + \mathcal{O}(b^4), \tag{B.16}$$

and, substituting $b = -\eta\chi|\Delta_0|^2/4$, I finally obtain

$$\frac{a_n^2 - b_n^2}{a_0^2} = 1 - \frac{1}{8}\eta^2\chi^2|\Delta_0|^4 + \frac{1}{8}\eta^3\chi^3|\Delta_0|^6. \tag{B.17}$$

up to $\mathcal{O}(|\Delta_0|^6)$ inclusive. Since the summands no longer depends on n, I recollect the summation over $k_\perp$, $k_\parallel$, and n into a sum over $|\mathbf{k}| < k_c$. I take the sum to include all $n \in (-n_c, n_c)$ with the $n = 0$ term identical to the rest. I justify this by noting that, for a system of size L^D, the sum over $k_\parallel$ for $n = 0$ is of order $2QL$ and is much smaller than the sum over all $k_\parallel < k_c$ (of order $2k_cL$) since $Q \ll k_c$ (where $Q \lesssim \xi_0^{-1}$ and $k_c = \pi/l$).

After subtracting the average magnetic contribution to the normal state, the fluctuation contribution to the superconducting free energy is

$$\mathcal{F}_{LO,M} = \frac{d}{2\beta}\sum_{|\mathbf{k}|=0}^{k_c}\left[\ln\left(1 + \frac{1}{2}\eta\chi|\Delta_0|^2\right) + \ln\left(1 - \frac{1}{8}\eta^2\chi^2|\Delta_0|^4 + \frac{1}{8}\eta^3\chi^3|\Delta_0|^6\right)\right], \tag{B.18}$$

which, with $d = 3$, is the expression given in Eq. (4.10).

Appendix C: Landau Coefficients in the Zero Temperature Limit

I determine the Landau coefficients $\bar{\alpha}_{LO}$ and $\bar{\gamma}_{LO}$ and their temperature derivatives in the limit $t \to 0$. I first derive analytically α_{LO} and γ_{LO} from Eqs. (3.9) (with prefactor of 1/2 for LO) and (3.10) for both s- and d-wave at zero temperature; there the magnetic fluctuations die out so that $\bar{\alpha}_{LO} = \alpha_{LO}$ and $\bar{\gamma}_{LO} = \gamma_{LO}$. I then determine numerically the derivatives $\alpha'_{LO}(0)$, $\alpha''_{LO}(0)$, and $\gamma'_{LO}(0)$ for d-wave symmetry and add to them the magnetic fluctuation corrections at $t = 0$.

C.0.1 Analytic determination of b_c, q_0, and γ_{LO}

I first evaluate the quadratic Landau coefficient for the LO gap modulation. In the limit $t = 0$, the quadratic coefficient becomes

$$\alpha_{LO} = \frac{1}{4}\left\langle |\mathcal{Y}(\theta)|^2 \ln\left((b+\bar{q})^2\right)\right\rangle - \frac{1}{2}\Psi\left(\frac{1}{2}\right) , \tag{C.1}$$

where $\mathcal{Y}(\theta) = 1$ and $\mathcal{Y}(\theta) = \sqrt{2}\cos 2\theta$ for s- and d-wave gaps, respectively. Here I use $b = \mu B/(2\pi T_{c0})$ and $\bar{q} = q\cos(\theta - \theta_q)$ where $q = \xi_0 Q/2$. The angle θ_q is the modulation direction with respect to the crystalline a axis, and $\theta_q = \pi/4$ for nodally-oriented d-wave. Integration over θ yields

$$\alpha_{LO,s} = \frac{1}{2}\mathrm{Re}\left[\ln\left(\frac{b+\sqrt{b^2-q^2}}{2}\right)\right] - \frac{1}{2}\Psi\left(\frac{1}{2}\right) \tag{C.2}$$

and

$$\alpha_{LO,d} = \frac{1}{4}\ln\left(\frac{q^2}{4}\right) + \frac{b^4}{q^4} - \frac{b^2}{q^2} + \frac{1}{8} - \frac{1}{2}\Psi\left(\frac{1}{2}\right) \tag{C.3}$$

for s- and d-wave respectively. I locate the transition by finding the maximum b for which $\alpha_{LO,d} = 0$, and I find that for s-wave

$$q_{0,s} = b_{c,s} = 2e^{\Psi(1/2)} = \frac{e^{-\gamma_E}}{2} \simeq 0.281 , \tag{C.4}$$

where $\gamma_E \approx 0.577$ is Euler's constant, and for d-wave

$$\begin{aligned} q_{0,d} &= \frac{e^{-\gamma_E}}{2} \exp\left(-2a^4 + 2a^2 - \frac{1}{4}\right) \simeq 0.337\,, \\ b_{c,d} &= a q_{0,d} \simeq 0.278\,, \end{aligned} \tag{C.5}$$

where $a = ((1+\sqrt{3})/4)^{1/2} \simeq 0.826$.

To determine the quartic Landau coefficient, first note that, in the limit $T = 0$, the Matsubara sum $2\pi T \sum_n F(\omega_n)$ becomes the integral $\int d\omega F(\omega)$. Thus, I rewrite Eq. (3.10) as

$$\gamma_{LO} = \mathrm{Re} \int_0^\infty \frac{d\bar{\omega}}{128\pi^2} \int_0^{2\pi} \frac{d\theta}{2\pi} |\mathcal{Y}(\theta)|^4 I_\gamma(\bar{\omega}, b, q, \theta)\,, \tag{C.6}$$

where $\bar{\omega} = \omega/(2\pi T_{c0})$ and

$$I_\gamma(\bar{\omega}, b, q, \theta) = \frac{(\bar{\omega} + ib)\left(3\left(\bar{\omega} + ib\right)^2 - \bar{q}^2\right)}{\left(\left(\bar{\omega} + Ib\right)^2 + \bar{q}^2\right)^3}\,. \tag{C.7}$$

I perform the angular integration changing variables to $z = e^{i\theta}$, and then integrating around the unit circle in the complex z-plane. After thus averaging over the Fermi surface, I arrive at

$$I_{\gamma,s}(\bar{\omega}, b, q) = \frac{2q^4 + 5q^2\bar{\omega}_b^2 + 6\bar{\omega}_b^4}{2\bar{\omega}_b^2 (q^2 + \bar{\omega}_b^2)^{5/2}} \tag{C.8}$$

and

$$I_{\gamma,d}(\bar{\omega}, b, q) = \frac{24\bar{\omega}_b}{q^8} \frac{8q^4\bar{\omega}_b + 44q^2\bar{\omega}_b^3 + 40\bar{\omega}_b^5}{\sqrt{q^2 + \bar{\omega}_b^2}} - \frac{24\bar{\omega}_b}{q^8}\left(q^4 + 24q^2\bar{\omega}_b^2 + 40\bar{\omega}_b^4\right) \tag{C.9}$$

for s-wave and d-wave, respectively. Here $\bar{\omega}_b = \bar{\omega} + ib$. Evaluating the integral over $\bar{\omega}$ I arrive at

$$\gamma_{LO,s} = \frac{3}{32\pi^2} \frac{3b^2 - 2q^2}{b(b^2 - q^2)^{3/2}}\,, \tag{C.10}$$

and

$$\gamma_{LO,d} = \frac{1}{64\pi^2 q^2}\left(1 - 2\frac{b^2}{q^2}\left(3 - 36\frac{b^2}{q^2} + 40\frac{b^4}{q^4}\right)\right)\,, \tag{C.11}$$

the quartic Landau coefficients at $t = 0$. From Eq. (C.10), I find that $\gamma_{LO,s}$ diverges as $b_c \to q_0$ (see Eq. (C.4)) while, from Eq. (C.5) and (C.11) I see that $\gamma_{LO,d} \simeq 0.070$ remains finite when $T \to 0$.

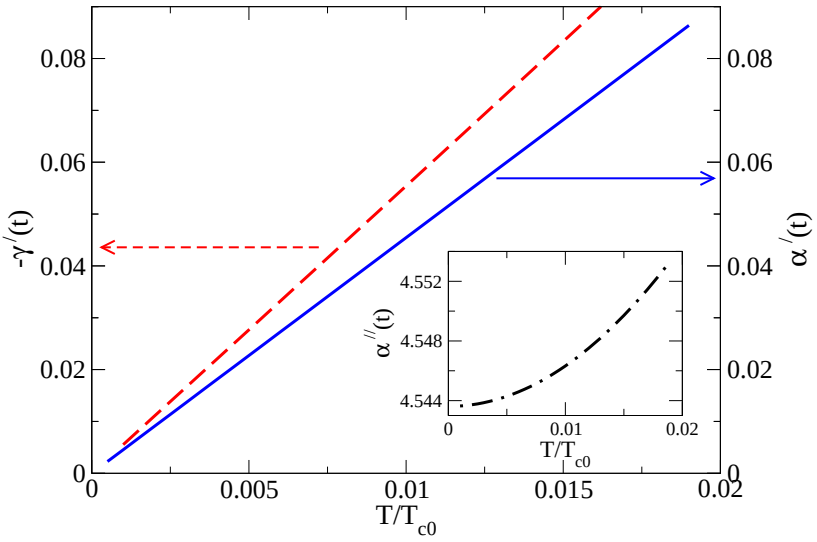

Figure C.1: Temperature derivatives of quadratic and quartic Landau coefficients for d-wave at fixed $b_{c,d}$ and $q_{0,d}$ in zero temperature limit. Main figure shows α'_{LO} and $-\gamma'_{LO}$, both of which limit to zero at $t = 0$. Inset: $\alpha''_{LO} \approx 4.54$ at $t = 0$.

C.0.2 Evaluation of derivatives for d-wave at $T = 0$

The temperature derivatives of the quadratic and quartic coefficients are

$$\bar{\alpha}'_{LO}(\tilde{\eta}, t) = \alpha'_{LO}(t) + \frac{1}{2}\tilde{\eta}\chi\,, \tag{C.12a}$$

$$\bar{\alpha}''_{LO}(\tilde{\eta}, t) = \alpha''_{LO}(t) + \tilde{\eta}\chi'\,, \tag{C.12b}$$

$$\bar{\gamma}'_{LO}(\tilde{\eta}, t) = \gamma'_{LO}(t) - \frac{1}{6t_F}\tilde{\eta}^2\chi^2\,. \tag{C.12c}$$

Expressions for $\alpha'_{LO}(t)$, $\alpha''_{LO}(t)$, and $\gamma'_{LO}(t)$ are obtained by taking the first and second derivatives of Eq. (3.9) (with prefactor of $1/2$ for LO modulation) and the first derivative of Eq. (3.10), respectively, with respect to t.

I determine $\alpha'_{LO}(0)$, $\alpha''_{LO}(0)$, and $\gamma'_{LO}(0)$ numerically by fixing $b = b_{c,d}$ and $q = q_{0,d}$ and evaluating the derivatives as t approaches zero. As shown in Fig. C.1, I find that $\alpha'_{LO} = \gamma'_{LO} = 0$ and $\alpha''_{LO} \approx 4.544$ at $t = 0$. Using these values and working with $\chi(T)$, I obtain $\bar{\alpha}'_{LO}(0) = 6.18\tilde{\eta}\tilde{\chi}$, $\bar{\alpha}''_{LO}(0) = 4.544 - 152.8\tilde{\eta}\tilde{\chi}$, and $\bar{\gamma}'_{LO}(0) = -1.48(\tilde{\eta}\tilde{\chi})^2$ in the zero temperature limit.

Appendix D: Constraint on Gap Amplitudes for Two-band Systems

A two band system, with band indices j, j', with a purely inter-band pairing potential $V_{jj'}(\mathbf{k}, \mathbf{k}')$ is described by the mean field Hamiltonian $H_0{=}\sum_j H_j$ where

$$H_j = \sum_{\mathbf{k}\sigma} \xi_{j\mathbf{k}} c^\dagger_{j\mathbf{k}\sigma} c_{j\mathbf{k}\sigma} - \sum_{\mathbf{k}} \left(\Delta_{j\mathbf{k}} c^\dagger_{j\mathbf{k}\uparrow} c^\dagger_{j-\mathbf{k}\downarrow} + \Delta^*_{j\mathbf{k}} c_{j-\mathbf{k}\downarrow} c_{j\mathbf{k}\uparrow} \right) \tag{D.1}$$

is the mean field Hamiltonian for band j, with the superconducting gap function on the j-th Fermi surface sheet self-consistently determined by

$$\Delta_{j\mathbf{k}} = \sum_{\mathbf{k}'} V_{jj'}(\mathbf{k}, \mathbf{k}') \langle c_{j'\mathbf{k}'\uparrow} c_{j'-\mathbf{k}'\downarrow} \rangle \,. \tag{D.2}$$

Here $\xi_{j\mathbf{k}}$ is the quasiparticle energy in band j, measured with respect to the chemical potential, and $c^\dagger_{j\mathbf{k}\sigma}$ and $c_{j\mathbf{k}\sigma}$ are the creation and annihilation operators for quasiparticles with momentum $\mathbf{k}$ and the spin projection σ.

I assume a separable form of the interaction $V_{jj'}(\mathbf{k}, \mathbf{k}') = \lambda_{jj'} f_j(\hat{k}) f_{j'}(\hat{k}')$ with the pairing-interaction strength $\lambda_{jj'}$. The function $f_j(\hat{k})$ defines the pairing symmetry and $\hat{k}$ denotes direction on the j-th Fermi surface sheet. Hence, the self consistency equations can be rewritten as

$$\begin{aligned} \Delta_j &= \lambda_{jj'} \sum_{\mathbf{k}'} f^2_{j'}(\hat{k}') \langle c_{j'\mathbf{k}'\uparrow} c_{j'-\mathbf{k}'\downarrow} \rangle \\ &= -T\lambda_{jj'} \sum_{n,\mathbf{k}'} \frac{\Delta_{j'} f^2_{j'}(\hat{k}')}{\omega_n^2 + \xi^2_{j'\mathbf{k}} + \Delta^2_{j'} f^2_{j'}(\hat{k}')} \,, \end{aligned} \tag{D.3}$$

where the gap amplitude $\Delta_j > 0$ is defined via $\Delta_{j\mathbf{k}}{=}\Delta_j f_j(\hat{k})$ and $\omega_n{=}2\pi T(n + 1/2)$ is the fermionic Matsubara frequency for temperature T.

Since the pairing interaction strength is symmetric in the band-indices, the gap ampli-

tudes are related as

$$\frac{\Delta_h}{\Delta_e} = \frac{\sum_{n,\mathbf{k}} \frac{\Delta_e f_e^2(\hat{k})}{\omega_n^2 + \xi_{e\mathbf{k}}^2 + \Delta_e^2 f_e^2(\hat{k})}}{\sum_{n,\mathbf{k}} \frac{\Delta_h f_h^2(\hat{k})}{\omega_n^2 + \xi_{h\mathbf{k}}^2 + \Delta_h^2 f_h^2(\hat{k})}} . \tag{D.4}$$

I write $\sum_k F(\mathbf{k}) \approx N_j \int_{-\omega_c}^{\omega_c} d\xi_j \int_0^{2\pi} d\phi_j/(2\pi) F(\xi_j, \phi_j)$, where ξ_j is perpendicular to the j-th FS sheet, ϕ_j is the direction on the j-th FS sheet, and ω_c is the cutoff frequency. Thus, rewriting Eq. (D.4), I have

$$1 = \frac{\sum_n \int_{-\omega_c}^{\omega_c} d\xi_e \int_0^{2\pi} \frac{d\phi_e}{2\pi} \frac{N_e \Delta_e^2 f_e^2(\phi_e)}{\omega_n^2 + \xi_e^2 + \Delta_e^2 f_e^2(\phi_e)}}{\sum_n \int_{-\omega_c}^{\omega_c} d\xi_h \int_0^{2\pi} \frac{d\phi_h}{2\pi} \frac{N_h \Delta_h^2 f_h^2(\phi_h)}{\omega_n^2 + \xi_h^2 + \Delta_h^2 f_h^2(\phi_h)}} . \tag{D.5}$$

I assume that $f_h(\phi_h) = 1$ so that the gap on the hole-like FS sheet is isotropic. I also assume that $f_e(\phi_e) = -(1 + r\cos\phi_e)$, where the parameter r controls the anisotropy of the gap on the electron-like FS.

In the weak-coupling limit $\omega_c \gg \Delta_j$, I find that

$$\begin{aligned} 1 &= \frac{N_e}{N_h} \int_0^{2\pi} \frac{d\phi_e}{2\pi} \frac{\Delta_e^2 (1 + r\cos\phi_e)^2}{\Delta_h^2} \\ &= \frac{N_e}{N_h} \frac{\Delta_e^2}{\Delta_h^2} \left(1 + \frac{r^2}{2}\right) \end{aligned} \tag{D.6}$$

at $T = 0$, so that the ratio N_h/N_e is equal to the ratio of the Fermi-surface average of the squared SC gap on each FS sheet. When $r = 0$, the condition in Eq. (D.6) reduces to the expression reported in Refs. [89, 135]. Using my notations $\delta_0 = \Delta_e/\Delta_h$ and $n = N_e/N_h$, the last line of Eq. (D.6) becomes the expression I use in Eq. (7.2).

Appendix E: Derivation of Local Green's Function for Anisotropically-Gapped Band

E.1 Choice of Branch Cuts for Integration of Green's Functions

As shown in Eq. (8.1), the T-matrix depends on only the local Green's functions $\widehat{g}_j = \sum_{\mathbf{k}} \widehat{G}_{j,0}(\mathbf{k}) = \sum_i g_{ji}\widehat{\tau}_i$ where $\widehat{\tau}_0$ is the identity matrix and $\widehat{\tau}_i$ $(i = 1, 2, 3)$ are the Pauli matrices. Working in two dimensions, I take $\sum_k = N_j \int d\xi \int d\phi/(2\pi)$, with ϕ the azimuthal angle and N_j the normal-state Fermi-level DOS. Assuming particle-hole symmetry ($g_{j3} = 0$) and integrating perpendicular to the FS, I obtain the Green's functions

$$\widehat{g}_h(\omega) = -\pi N_h \frac{\omega\widehat{\tau}_0 + \Delta_h\widehat{\tau}_1}{\sqrt{\Delta_h^2 - \omega^2}}\,. \tag{E.1}$$

for the isotropically-gapped hole band and

$$\frac{g_{e0}(\omega)}{\pi N_e} = -\int_0^{2\pi} \frac{d\phi}{2\pi} \frac{\omega}{\sqrt{\Delta_e(1 + r\cos(2\phi))^2 - \omega^2}}\,, \tag{E.2a}$$

$$\frac{g_{e1}(\omega)}{\pi N_e} = \int_0^{2\pi} \frac{d\phi}{2\pi} \frac{\Delta_e(1 + r\cos(2\phi)))}{\sqrt{\Delta_e^2(1 + r\cos(2\phi))^2 - \omega^2}} \tag{E.2b}$$

for the anisotropically-gapped electron band.

The physical properties of the system are determined from the retarded Green's function which has poles only in the lower half of the complex energy plane; therefore, the poles of the T-matrix *must* lie at $\omega = \omega_1 + i\omega_2$ with $\omega_2 \leq 0$. To ensure this analytic property, I define the complex-valued square root $\sqrt{\Delta^2(\phi) - \omega^2}$ such that the branch cut consists of two lines extending from $\omega = \pm\Delta(\phi)$ to $\omega = \pm\Delta(\phi) - i\infty$ and meeting at the point at infinity (see Fig. E.1). (I denote with $\sqrt{z}$ the square root with the standard branch cut along the negative real axis.) With this branch cut, the retarded Green's functions are analytic in the upper

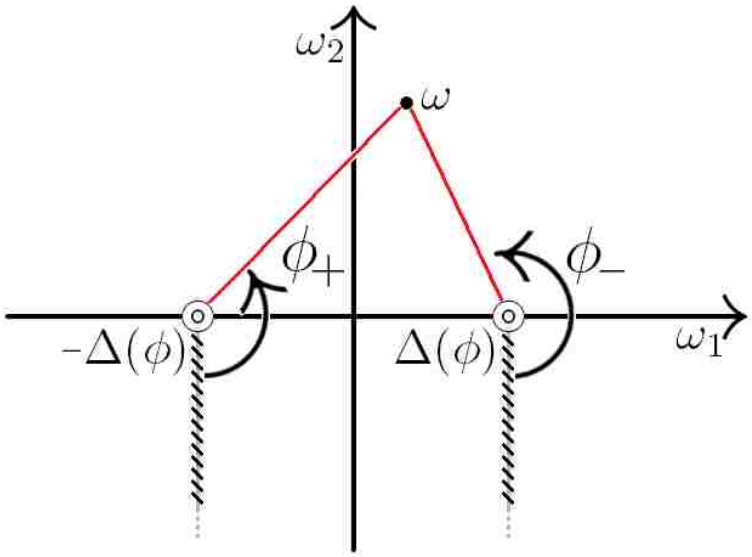

Figure E.1: Branch cut structure for complex-valued $\sqrt{\Delta^2(\phi)-\omega^2}\,' = -\sqrt{\rho_+\rho_-}e^{i(\phi_++\phi_-)/2}$. Branch cuts (hashed lines) extend from $\omega = \pm\Delta(\phi)$ to $\omega = \pm\Delta(\phi) - i\infty$. Phase angles are measured from branch cuts as shown.

half ω plane, yielding the DOS at $\omega = \omega_1 + i0^+$ and are continuous and well-defined across the real frequency axis.

With this choice of branch cut and the changes of variables $\varepsilon = \omega/\Delta_h$ and $\cos(2\phi) = \mathrm{Re}\,(z)$, the Green's functions in Eqs. (E.1) and (E.2) become

$$\frac{\widehat{g}_h(\varepsilon)}{\pi N_h} = -\frac{\varepsilon\widehat{\tau}_0 + \widehat{\tau}_1}{\sqrt{1-\varepsilon^2}\,'} \tag{E.3a}$$

$$\frac{g_{e0}(\tilde{\varepsilon})}{\pi N_e} = -\frac{\tilde{\varepsilon}}{\pi} I_0(\tilde{\varepsilon}) \tag{E.3b}$$

$$\frac{g_{e1}(\tilde{\varepsilon})}{\pi N_e} = \frac{1}{\pi}\left(I_0(\tilde{\varepsilon}) + I_1(\tilde{\varepsilon})\right)\,, \tag{E.3c}$$

with $\tilde{\varepsilon} = \omega/\Delta_e = \varepsilon/\delta_0$ and $\delta_0 = \Delta_e/\Delta_h$. The integrals in Eqs. (E.3b) and (E.3c) are

$$I_0(\tilde{\varepsilon}) = \int_{-1}^{1} \frac{dz}{\sqrt{1-z^2}\,'\sqrt{(1+rz)^2-\tilde{\varepsilon}^2}\,'} \tag{E.4a}$$

$$I_1(\tilde{\varepsilon}) = \int_{-1}^{1} \frac{r\,z\,dz}{\sqrt{1-z^2}\,'\sqrt{(1+rz)^2-\tilde{\varepsilon}^2}\,'}\,. \tag{E.4b}$$

I integrate along the straightest possible contour which is C_1 (straight-line $z \in [-1,1]$) for $\tilde{\varepsilon}_2 \geq 0$. Mapped into the complex z-plane, the branch cuts of $\sqrt{(1+rz)^2-\tilde{\varepsilon}^2}\,'$ terminate at

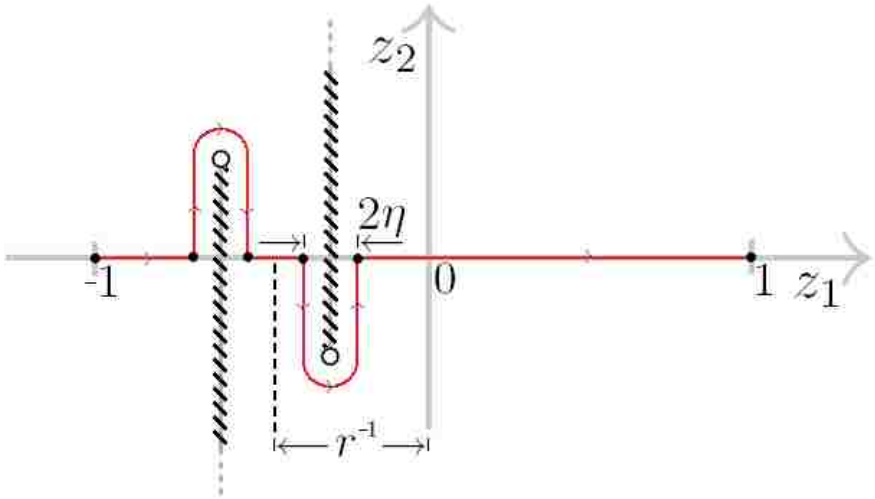

Figure E.2: Branch cuts (hashed lines) and integration contour (solid line) in complex z-plane ($z = z_1 + iz_2$) for fixed $\varepsilon = \varepsilon_1 + i\varepsilon_2$ with $r > 1$, $\varepsilon_2 < 0$, and $\varepsilon_1 \in (1-r, 1+r)$. Branch cuts terminate at $z_\pm = (-1 \pm \varepsilon)/r$ and, as shown, cross z_1 axis for $e_2 < 0$. The contour is deformed as shown ($\eta = 0^+$) when branch cuts cross the line $z \in (-1, 1)$.

$z_\pm = (-1 \pm \tilde{\varepsilon})/r$ and cross the $\mathrm{Re}\,(z)$ axis for $\tilde{\varepsilon}_2 < 0$ (see Fig. E.2). When $\tilde{\varepsilon}_1$ falls within the smallest gap ($|\tilde{\varepsilon}_1| < |1-r|$) of the nodal SC state ($r > 1$), both of the branch cuts cross C_1. In this case, the contour must be deformed around the branch cut as shown in Fig. E.2. When $|\tilde{\varepsilon}_1| \in (|1-r|, 1+r)$ only the branch cut passing through $z = (-1 + |\tilde{\varepsilon}_1|)/r$ crosses C_1.

E.2 Analytical Expressions for Green's Functions with an Anisotropic Gap

It is advantageous to express the integrals (E.4a) and (E.4b) in terms of the the complete

elliptic integrals

$$K(m) = \int_0^1 \frac{dx}{\sqrt{(1-x^2)(1-mx^2)}} \tag{E.5a}$$

$$\Pi(n,m) = \int_0^1 \frac{dx/\left(1-nx^2\right)}{\sqrt{(1-x^2)(1-mx^2)}}\,, \tag{E.5b}$$

where I use the notational conventions of Ref. [149]. Thus, the Green's functions take the closed form

$$\frac{\widehat{g}_h(\varepsilon)}{\pi N_h} = -\mathrm{sgn}\left(1+\mathrm{sgn}(\varepsilon_2)|\varepsilon_1|\right)\frac{\varepsilon\widehat{\tau}_0+\widehat{\tau}_1}{\sqrt{1-\varepsilon^2}} \tag{E.6a}$$

$$\frac{g_{e0}(\tilde{\varepsilon})}{\pi N_e} = -\frac{2i\,\mathrm{sgn}(\tilde{\varepsilon}_1)\tilde{\varepsilon}\widetilde{K}(b)}{\pi\sqrt{\left(\mathrm{sgn}(\tilde{\varepsilon}_1)\tilde{\varepsilon}+r\right)^2-1}} \tag{E.6b}$$

$$\frac{g_{e1}(\tilde{\varepsilon})}{\pi N_e} = \frac{2i\left(\tilde{\varepsilon}\widetilde{K}(b)-\left(\tilde{\varepsilon}+\mathrm{sgn}(\tilde{\varepsilon}_1)(1-r)\right)\widetilde{\Pi}(a,b)\right)}{\pi\sqrt{\left(\mathrm{sgn}(\tilde{\varepsilon}_1)\tilde{\varepsilon}+r\right)^2-1}}\,, \tag{E.6c}$$

with the arguments

$$a = \frac{2r}{\mathrm{sgn}(\tilde{\varepsilon}_1)\tilde{\varepsilon}+r+1} \tag{E.7a}$$

$$b = \frac{4r\mathrm{sgn}(\tilde{\varepsilon}_1)\tilde{\varepsilon}}{\left(\mathrm{sgn}(\tilde{\varepsilon}_1)\tilde{\varepsilon}+r\right)^2-1}\,. \tag{E.7b}$$

With $S=\mathrm{sgn}(1+|\tilde{\varepsilon}|^2-r^2)$, $s_1=\mathrm{sgn}(\tilde{\varepsilon}_2)$, $s_2=\mathrm{sgn}(\tilde{\varepsilon}_2)$ and $p(\tilde{\varepsilon}_2,r)=(1-2\Theta(-\tilde{\varepsilon}_2)\Theta(1-r))$, where $\Theta(x)$ the unit-step function, the piecewise-defined functions $\widetilde{K}(b)$ and $\widetilde{\Pi}(a,b)$ are

$$\widetilde{K}(b) = \begin{cases} p(\tilde{\varepsilon}_2,r)K(b)+is_1\Theta(r-1)\left(s_2(S+1)-2\right)K(1-b) & (I) \\ K(b)+is_1\left(s_2S-1\right)K(1-b) & (II) \\ K(b)+is_1\left(s_2(S+1)-2\right)K(1-b) & (III) \end{cases} \tag{E.8}$$

and

$$\widetilde{\Pi}(a,b) = \begin{cases} p(\tilde{\varepsilon}_2,r)\Pi(a,b)-\frac{\pi\Theta(-\tilde{\varepsilon}_2)\Theta(r-1)}{\sqrt{1-a}\sqrt{1-b/a}}+i\frac{s_1\Theta(r-1)(s_2(S+1)-2)}{1-a/b}\Pi\left(\frac{1-b}{1-b/a},1-b\right) & (I) \\ \Pi(a,b)+i\frac{s_1(s_2S-1)}{1-a/b}\Pi\left(\frac{1-b}{1-b/a},1-b\right) & (II) \\ \Pi(a,b)-\frac{\pi\Theta(-\tilde{\varepsilon}_2)}{\sqrt{1-a}\sqrt{1-b/a}}+i\frac{s_1(s_2(S+1)-2)}{1-a/b}\Pi\left(\frac{1-b}{1-b/a},1-b\right) & (III) \end{cases} \tag{E.9}$$

for energies (I) below the smaller gap edge ($|\tilde{\varepsilon}_1|<|1-r|$), (II) between the gap edges ($|1-r|<|\tilde{\varepsilon}_1|<1+r$), and (III) above the larger gap edge ($|\tilde{\varepsilon}_1|>1+r$). These complicated

expressions result from the analytic continuation of $K(b)$ and $\Pi(a,b)$ across their two branch cuts in the $\tilde{\varepsilon}$-plane: the real energy axis and, for $r>1$, the circle of radius $\sqrt{r^2-1}$ defined by $S=0$. For $|\tilde{\varepsilon}|^2 > r^2-1$ in the upper half plane, Eqs. (E.8) and (E.9) become simply $\widetilde{K}(b) = K(b)$ and $\widetilde{\Pi}(a,b) = \Pi(a,b)$.

E.2.1 Asymptotic expansion

To examine resonances deep within the gap for broad featureless bands ($g_{e3} = g_{he} = 0$), I need small-$\tilde{\varepsilon}$ asymptotic expressions for g_{e0} and g_{e1} . Using, from Ref. [149], the identities

$$K(z) =\simeq \frac{\pi}{2}\left(1+\mathcal{O}(z)\right)\ ,\ z\to 0 \tag{E.10}$$

and

$$K(z) \simeq -\frac{1}{2}\ln\left(\frac{1-z}{16}\right)\ ,\ z\to 1\,, \tag{E.11}$$

the lowest-order terms in the small-$\tilde{\varepsilon}$ expansion of g_{e0} in the region $|\tilde{\varepsilon}| < |1-r|$ are

$$\frac{g_{e0}}{\pi N_e} \simeq -\frac{i\,\mathrm{sgn}(\tilde{\varepsilon}_1)\tilde{\varepsilon}}{\sqrt{r^2-1}} - \frac{2}{\pi}\frac{\tilde{\varepsilon}}{\sqrt{r^2-1}}\ln\left(\frac{4(r^2-1)}{\mathrm{sgn}(\tilde{\varepsilon}_1)\tilde{\varepsilon}r}\right)\,. \tag{E.12}$$

Using, also from Ref. [149], the identity

$$\Pi(-n,m) = \frac{2\sqrt{n}\,\mathrm{atan}\left(\sqrt{n}\right) + \ln(16/(1-m))}{2(n+1)} \tag{E.13}$$

I obtain the small-$\tilde{\varepsilon}$ expansion

$$\frac{g_{e1}}{\pi N_e} \simeq \mathrm{P}_r - i\frac{1}{2}\frac{\mathrm{sgn}(\tilde{\varepsilon}_1)}{(r^2-1)^{3/2}}\tilde{\varepsilon}^2\,. \tag{E.14}$$

The expression

$$\begin{aligned}\mathrm{P}_r &= \frac{1}{\pi}\int_0^\pi \mathrm{sgn}\left[1+r\cos(\theta)\right]d\theta \\ &= \begin{cases} 1 & 0<r<1 \\ 1-\frac{2}{\pi}\mathrm{acos}\left(\frac{1}{r}\right) & r>1 \end{cases}\end{aligned} \tag{E.15}$$

follows directly from Eq. (E.2b) with $\omega = 0$ and $\theta = 2\phi$.

Appendix F: Statement of Permission

Chapters 3, 4, 5, and 11 were adapted in large part from

> R. Beaird, A. B. Vorontsov, and I. Vekhter, Physical Review B **81**, 224501 (2010). Copyright (2010) by the American Physical Society.

Permission for its use is granted to me by the American Physical Society per the statement

> [T]he author has the right to use the article or a portion of the article in a thesis or dissertation without requesting permission from APS, provided the bibliographic citation and the APS copyright credit line are given on the appropriate pages.

as taken from its copyright FAQ at http://publish.aps.org/copyrightFAQ.html#thesis.

Vita

Robert Pearson Beaird was born in Shreveport, Louisiana, on February 5, 1981. He earned his bachelor's degree in physics and his bachelor's degree in mathematics in 2003 from Centenary College of Shreveport. In August of 2003, he enrolled in graduate school at Louisiana State University in Baton Rouge. He received his master's degree in physics in 2008 from LSU, and expects to receive his doctoral degree in May 2011.